Missouri S&T Library and Learning Resources

Scholars' Mine

Doctoral Dissertations

Student Theses and Dissertations

Fall 2016

Properties of Amorphous Transparent Conducting and Semiconducting Oxides from First Principles

Rabi Khanal

Follow this and additional works at: https://scholarsmine.mst.edu/doctoral_dissertations

Part of the Physics Commons

Department: Physics

Recommended Citation

Khanal, Rabi, "Properties of Amorphous Transparent Conducting and Semiconducting Oxides from First Principles" (2016). *Doctoral Dissertations*. 2539.
https://scholarsmine.mst.edu/doctoral_dissertations/2539

This thesis is brought to you by Scholars' Mine, a service of the Missouri S&T Library and Learning Resources. This work is protected by U. S. Copyright Law. Unauthorized use including reproduction for redistribution requires the permission of the copyright holder. For more information, please contact scholarsmine@mst.edu.

PROPERTIES OF AMORPHOUS TRANSPARENT CONDUCTING AND SEMICONDUCTING OXIDES FROM FIRST PRINCIPLES

by

RABI KHANAL

A DISSERTATION

Presented to the Graduate Faculty of the

MISSOURI UNIVERSITY OF SCIENCE AND TECHNOLOGY

In Partial Fulfillment of the Requirements for the Degree

DOCTOR OF PHILOSOPHY

in

PHYSICS

2016

Approved by

Dr. Julia E. Medvedeva, Advisor
Dr. Gerald Wilemski
Dr. Paul E. Parris
Dr. Richard K. Brow
Dr. Matthew Grayson

Copyright 2016

RABI KHANAL

All Rights Reserved

PUBLICATION DISSERTATION OPTION

This dissertation has been prepared in the form of four papers that has been published as follows:

Paper I, Pages 37–66, has been published as *The structure and properties of amorphous indium oxide*, Chemistry of Materials **26**, 5401-5411 (2014) with D. Bruce Buchholz, Qing Ma, Diego Alducin, Arturo Ponce, Miguel Jose-Yacaman, Julia E. Medvedeva, and Robert P. H. Chang.

Paper II, Pages 67–85, has been published as *Long-range structural correlations in amorphous ternary In-based oxides*, Vacuum **114**, 142-149 (2015) with Julia E. Medvedeva.

Paper III, Pages 86–113, has been published as *Cation Size Effects on the Electronic and Structural Properties of Solution-Processed In-X-O Thin Films*, Advanced Electronic Materials **1**, 7 (2015) with Jeremy Smith, Li Zeng, Katie Stallings, Antonio Facchetti, Julia E. Medvedeva, Michael J. Bedzyk, and Tobin J. Marks.

Paper IV, Pages 114–144, has been published as *Composition-dependent structural and transport properties of amorphous transparent conducting oxides*, Physical Review B **91**, 205203 (2015) with D. Bruce Buchholz, Robert P. H. Chang, and Julia E. Medvedeva.

The Introduction (Section 1), Methods and approach (Section 2), and Conclusions (Section 3) have been added for purposes normal to dissertation writing.

ABSTRACT

Amorphous transparent conducting and semiconducting oxides possess properties superior or comparable to their crystalline counterparts. The structure-property relationship in amorphous oxides is not nearly as well understood as in the case of the crystalline transparent conducting oxides. We have employed *ab initio* molecular dynamics and a liquid quench approach to simulate amorphous oxide structures and performed density functional-based calculations to study the electronic properties of several amorphous conducting and semiconducting oxides with various cation compositions.

The effect of amorphization in oxides was investigated by taking indium oxide as a progenitor of the system. From the thorough study it was confirmed that the distribution and connectivity of naturally coordinated indium polyhedra (InO_6) depend on the cooling rates used in the quenching process. Also, it was shown experimentally that the transport properties depend strongly on the deposition temperature, in particular, the carrier Hall mobility is enhanced at the onset of the amorphous region to become similar to the mobility in crystalline In_2O_3. Our results have shown that the corresponding amorphous structure exhibits a long chain of the InO_6 connected primarily via corner sharing, thus, highlighting the importance of the medium/long-range structural characteristics.

To understand the effect of chemical composition on the structure and properties of amorphous oxides, In-X-O with X=Sn, Zn, Ga, Cd, Ge, Sc, Y, or La, were studied. The results reveal that the short-range structure of the metal-O polyhedra is preserved in the amorphous oxides; therefore, the extended nature of the conduction band, the key feature of transparent conducting oxide, is maintained. Unlike the case of crystalline transparent oxides, additional cation in amorphous oxides does not act as a dopant. Instead, the presence of X affects the number of naturally coordinated In atoms as well as the oxygen sharing between metal-oxygen polyhedra which ultimately affects the transport properties.

ACKNOWLEDGMENTS

I am sincerely and heartily grateful to my advisor Dr. Julia E. Medvedeva for her endless support. This work would not have been possible without her immense guidance, motivation, and supervision.

I would also like to express my gratitude and appreciation to my committee members Dr. Gerald Wilemski, Dr. Paul Parris, Dr. Richard K. Brow, and Dr. Matthew Grayson for their input, valuable discussions, and accessibility. To Dr. Gerald Wilemski, thank you for your encouragement, support, and help; I will be forever thankful to you.

I would like to thank the members of Northwestern University MRSEC, especially the members of Prof. Chang's, Prof. Marks's and Prof. Grayson's group for the collaboration on projects and the discussions.

Also, I would like to thank our head of the department Dr. George D. Waddill, and our graduate coordinator Dr. Jerry L. Peacher; department staff members Pamela J. Crabtree, Janice Gargus, Russell L. Summers and Andrew L. Stubbs, for their help. I wish to thank my friends and especially the students at Missouri S&T for enjoyable and great memories. To Dr. Hatem Barghathi, thank you for your help and support. I am also thankful to Dr. Bijay Shrestha, Nancy Uri, and Nepali friends of Rolla for making me feel at home.

I acknowledge the Dissertation Completion Fellowship provided through the office of the graduate studies.

Finally, my special thanks go to my parents Kashi Nath Khanal and Dev Kumari Khanal. Their love and support throughout my life were vital in many ways in completing this program. Also, I would like to thank my brothers Suresh Khanal, and Min Prasad Khanal and all my relatives, for their support, guidance and encouragement.

TABLE OF CONTENTS

Page

PUBLICATION DISSERTATION OPTION iii

ABSTRACT iv

ACKNOWLEDGMENTS v

LIST OF ILLUSTRATIONS xi

LIST OF TABLES xvii

SECTION

1. INTRODUCTION 1

1.1. CRYSTALLINE TRANSPARENT CONDUCTING OXIDES 1

1.1.1. Conductivity in Transparent Conducting Oxides 2

1.1.2. Optical Properties of Transparent Conducting Oxides 3

1.2. AMORPHOUS OXIDES 5

1.2.1. Brief History of Amorphous Oxides 5

1.2.2. Comparative Properties of Crystalline and Amorphous Oxides 6

1.2.2.1 Structural properties 6

1.2.2.2 Optical properties 7

1.2.2.3 Transport properties 8

1.2.2.4 Mechanical and surface properties 8

1.2.3. Covalent vs. Ionic Amorphous Oxides 9

1.2.4. Experimental Growth Techniques 10

1.2.4.1 Thermal deposition 10

1.2.4.2 Sputtering 11

1.2.4.3 Pulsed-laser deposition 11

1.2.4.4 Atomic layer deposition 11

1.2.4.5 Spin-coating 11

1.2.4.6 Spray coating (spray pyrolysis) 11

1.2.4.7 Printing 12

1.2.5. Theoretical Methods of Generating Amorphous Structures 12

1.2.5.1 Monte carlo technique 12

1.2.5.2 Classical molecular dynamics (MD) 12

1.2.5.3 *Ab initio* or Quantum mechanical molecular dynamics 13

1.3. PROPERTIES OF AMORPHOUS CONDUCTING AND SEMICONDUCTING OXIDES 13

1.3.1. Transport in Amorphous Oxides 13

1.3.2. Subgap States in Amorphous Oxides 15

1.3.3. Optical Properties of Amorphous Oxides 16

2. METHODS AND APPROACH 19

2.1. INTRODUCTION 19

2.2. DENSITY FUNCTIONAL THEORY 20

2.2.1. Exchange-Correlation Functional 22

2.2.1.1 The local density approximation 22

2.2.1.2 The generalized gradient approximation 23

2.2.1.3 The hybrid functional 24

2.3. METHOD FOR CALCULATING BAND STRUCTURE 25

2.3.1. Plane Wave Pseudopotential Method 26

2.3.2. All-electron Methods 27

2.3.2.1 Augmented plane wave method (APW) 27

2.3.3. Linearized Augmented Plane Wave (LAPW) Method 28

2.3.4. Projector Augmented Wave (PAW) Method 28

2.4. OPTICAL PROPERTIES 29

2.5. *AB INITIO* MOLECULAR DYNAMICS SIMULATIONS 30

2.6. MEASURE OF LOCALIZATION IN AMORPHOUS SOLIDS 32

2.7. DISSERTATION OUTLINE 34

PAPER

I. THE STRUCTURE AND PROPERTIES OF AMORPHOUS INDIUM OXIDE 37

ABSTRACT 37

1. INTRODUCTION 39

2. EXPERIMENTAL SECTION 44

3. THEORETICAL 46

4. RESULTS AND DISCUSSION 47

5. CONCLUSIONS 65

6. ACKNOWLEDGMENTS 66

II. LONG-RANGE STRUCTURAL CORRELATIONS IN AMORPHOUS TERNARY IN-BASED OXIDES 67

ABSTRACT 67

1. INTRODUCTION 68

2. COMPUTATIONAL METHOD 69

3. RESULTS AND DISCUSSION 70

3.1. In-O and X-O distances in amorphous IO and IXO 70

3.2. In-O and X-O coordination in amorphous IO and IXO 73

3.3. In-M coordination and distances 74

3.4. InO_6 connectivity and spatial distribution 78

3.5. XO connectivity and spatial distribution 82

4. CONCLUSIONS 84

5. ACKNOWLEGEMENTS 85

III. CATION SIZE EFFECTS ON THE ELECTRONIC AND STRUCTURAL PROPERTIES OF SOLUTION-PROCESSED IN-X-O THIN FILMS 86

ABSTRACT 86

1. INTRODUCTION 88

2. STRUCTURAL AND ELECTRONIC CHARACTERIZATION 91

2.1. X-Ray Absorption Spectroscopy 91

2.2. Ab Initio Molecular Dynamics Simulation 91

2.3. Thin Film Transistor Charge Transport Models 93

3. RESULTS AND DISCUSSION 95

4. CONCLUSION 107

5. EXPERIMENTAL SECTION 109

6. ACKNOWLEDGEMENTS 112

IV. COMPOSITION-DEPENDENT STRUCTURAL AND TRANSPORT PROPERTIES OF AMORPHOUS TRANSPARENT CONDUCTING OXIDES 114

ABSTRACT 114

1. INTRODUCTION 115

2. COMPUTATIONAL METHOD 117

3. GROWTH AND CHARACTERIZATION 118

4. RESULTS AND DISCUSSION 119

4.1. Local (short-range) structural characteristics 119

4.1.1 In-O distances in amorphous In-O and In-X-O 119

4.1.2 X-O distances in amorphous In-X-O 123

4.1.3 In-O coordination in amorphous In-O and In-X-O 125

4.1.4 X-O coordination in amorphous In-X-O 126

4.2. Long-range structural characteristics 129

4.2.1 In-M distance distribution and total In-M coordination ... 129

4.2.2 Edge- and corner-shared In-M in amorphous oxides 130

4.2.3 InO_6 and XO_x spatial distribution 136

4.3. Structural models of amorphous In-X-O 140

5. CONCLUSIONS 143

6. ACKOWLEDGMENTS 144

SECTION

3. CONCLUSIONS 145

BIBLIOGRAPHY 147

VITA 162

LIST OF ILLUSTRATIONS

Figure Page

1.1 (Left) Schematic electronic band structure of insulating transparent oxide, with band gap E_g and a dispersed parabolic conduction band which originates from interactions between metal *s* and oxygen *p* states. (Right) A schematic band structure of transparent and conducting oxide, where conductivity results from the shift of Fermi level E_F up into the conduction band via a Burstein-Moss shift, E_{BM}. 3

1.2 The atomic structure of (a) c-In_2O_3: represented by the periodic arrangement of highly symmetric InO polyhedra and (b) a-InO: represented by the random collection of distorted InO polyhedra. Red balls denote the In atoms, whereas small blue ball represents the O atoms. 7

1.3 Schematic drawing of atomic orbital overlap for conventional compound semiconductor (a-Si:H) and ionic oxide semiconductors (a-IGZO) as adopted from Ref.[43]. 10

1.4 The carrier concentration as a function of O_2 pressure during the deposition in a-IGZO and a-IZO [30]. 15

1.5 Schematic models of subgap DOS in typical amorphous oxides adopted from Ref. [82]. VB = valence band, CB = conduction band 16

2.1 Pair distribution function, g(r), of indium oxide showing the three phases, i.e., initial (crystalline), liquid (melt) and amorphous during the liquid quench simulation. 31

2.2 Percent contribution corner-shared InO_6-InO_6 polyhedra to the total (edge and corner) shared InO_6 pairs as a function of cooling rate (black): Low-temperature region of Hall mobility versus deposition temperature curve as given in Ref.[147]. 35

PAPER I

1 Corner, edge and face sharing polyhedra 41

2 Structure of crystalline In_2O_3 (bixbyite) 42

3 GIXRD patterns of indium oxide films, ~350 nm thick, as a function of deposition temperature. The *c*-IO/*a*-IO ratio, is determined by the area of the crystalline XRD peaks to the combined areas of the crystalline XRD peaks and the “amorphous hump". 48

4 HRTEM images of indium oxide films deposited at a) -50 °C, b) 0 °C, c) +100 °C and d) +600 °C. Insets are representative SAED patterns from the respective films. 49

5 Hall mobility of indium oxide films, ~350 nm thick, as a function of deposition temperature. 50

6 a) In-O coordination number, N_{In-O}, b) In-O bond-distance, R_{In-O} and c) σ^2_{In-O} for the In-O shell of indium oxide films, ~350 nm thick, as a function of deposition temperature: Red markers, powdered In_2O_3 standard. 51

7 a) unperturbed lattice; b) rotation of corner sharing polyhedra; c) rotation of edge sharing polyhedra 52

8 a) unperturbed lattice; b) breaking of corner sharing bond; c) breaking of edge sharing bond. 53

9 a) In-In coordination number, N_{In-In}, b) In-In bond-distance, R_{In-In} and c) σ^2 for the In-In shell, σ^2_{In-In}, of indium oxide films, ~350 nm thick, as a function of deposition temperature: Red markers-powdered In_2O_3 standard. 55

10 First-shell, In-O a) Effective coordination number, b) average bond distance, and c) bond-distance statistical-spread obtained from the MD simulations for 80-atom cell amorphous InO with different cooling rates on bottom axis (black circle markers). Blue diamond markers; low deposition temperature region (top axis) of EXAFS data. 57

11 a) Pair distribution functions for edge-shared In-In (solid lines: centered at ~3.4 Å) and corner-shared In-In (dashed lines: centered at ~3.7 Å) as obtained from the MD simulations for 80-atom cell *a*-IO with different cooling rates. b) Total In-In coordination as a function of distance. 59

12 Second-shell, In-In a) Coordination number, b) average bond distance, and c) bond-distance statistical-spread obtained from the MD simulations for 80-atom cell *a*-IO with different cooling rates on bottom axis (black circle markers). Blue diamond markers; low deposition temperature region (top axis) of EXAFS. 61

13 Third-shell, black diamonds: left axis, In-In* coordination number; blue squares: right axis, average bond distance. 62

14 Percent contribution edge-shared InO_6-InO_6 polyhedra with respect to total (edge and corner) shared InO_6 pairs as a function of cooling rate (black): Low temperature region of Hall mobility versus deposition temperature curve of Figure 5 (blue). 63

15 Spatial distribution and connectivity of the InO_6 polyhedra in amorphous InO obtained via 500 K/ps (top), 250 K/ps (middle), and 50 K/ps (bottom) cooling rates. Indium and oxygen atoms are shown with large (red) and small (blue) balls. Only InO_6 polyhedra are shown in these plots. 64

PAPER II

1 (Left) Calculated average In-O pair correlation function, l_{av}, in Å, for amorphous IO and IXO. (Right) Calculated standard deviation of the radial In-O distance distribution, σ^2, in Å^2, for amorphous IO and IXO. The horizontal dash lines represent the corresponding values in amorphous IO. 71

2 (Left) Average X-O correlation function, l_{av}, in Å, in amorphous IXO. Also, the X-O distance in the corresponding crystalline binary (cross) and In-containing ternary (plus) oxides are given for comparison. (Right) Calculated standard deviation of the radial X-O distance distribution, σ^2, in Å^2, for amorphous IXO. 72

3 Average effective coordination number of In with oxygen atoms in amorphous IO and IXO. 75

4 Relative number of differently coordinated indium atoms in amorphous IO and IXO calculated within 2.36 Å around a central In atom. 76

5 Radial distance, in Å, from a central In atom at which the average In-M coordination number becomes 6.0 (triangles) and 12.0 (diamonds) in a-IO and a-IXO. The horizontal dash line corresponds to the values for a-IO and is given to guide the eye. 77

6 Average In-In distance, in Å (left) and average In-O-In angle, in degrees, (right) for edge-shared (circle) and corner-shared (square) In-In pairs in amorphous IO and IXO. For comparison, the crystalline In_2O_3 edge-shared and corner-shared In-In distances are 3.4 Å and 3.8 Å, respectively, and average In-O-In angles are 99-101° and 126°, respectively. 78

7 (Left) Number of edge-shared and corner-shared In_6-In_6 pairs in amorphous IO and IXO. (Right) Average In_6-In_6 distance, in Å, and average In_6-O-In_6 angle, in degrees, for the InO_6 polyhedra connected via edge- and corner-sharing in amorphous IO and IXO. The horizontal dash line represents the corresponding values averaged for the second and third shells in crystalline In_2O_3. 79

8 The probability of the number of In_6 neighbors calculated within a radial cut-off distance of 3.8 Å from a central In_6 in a-IO and a-IXO. The oxides are grouped according to the fractional number of the six-coordinated In atoms, c.f., Fig. 4, that is ~20 % for a-IO, a-ITO, and a-ICdO; ~30 % for a-ILaO, a-IYO, a-IGO, and a-IZO; ~40 % for a-IScO, and a-IGeO. 81

9 (Left) Number of edge-shared and corner-shared X-X pairs in amorphous IXO. (Right) Average X-X distance, in Å, and average X-O-X angle, in degrees, for the XO polyhedra connected via edge- and corner-sharing in IXO. 82

10 (Color online) Atomic structures of a-IXO, X=Zn, Ga, Sn, or Cd, highlighting the X-O bonds and XO polyhedra only. Small spheres represent oxygen atoms, and large spheres that are not connected with oxygen atoms represent In atoms.. 83

PAPER III

1 Grazing incidence XRD scans for In-X-O thin films processed at a) T_a = 250 °C and b) T_a = 300 °C. Film compositions are given as at% of the secondary cation, X (X = Sc, Y, La). Peak positions for the crystalline samples are at 2θ = 21.7^o, 30.8^o, 35.7^o and are consistent with the In_2O_3 bixbyite structure. The broad amorphous peak is centered at 2θ = 29-33°. 96

2 Representative structures of a) In-Sc-O, b) In-Y-O, and c) In-La-O from ab initio MD simulation. In each case, 20% of the In atoms are replaced with the secondary cation, X. InO_6 polyhedra are indicated on the structures in purple with In represented as red spheres, X as yellow spheres, and O as blue spheres. The proportion of InO_x polyhedra with x = 4, 5, and 6 are shown in d). 97

3 Thin film transistor data for measurements at room temperature taken in saturation to extract values of μ_{sat} and V_T. Regions corresponding to crystalline, semicrystalline, and amorphous films are indicated for films processed at a) T_a = 250 °C and b) T_a = 300 °C. Optimal devices characteristics are around 5 and 10 at% doping for the low and high-temperature processed films, respectively. .. 98

4 Temperature-dependent field-effect electron mobility showing linear fits for the extraction of the activation energy, E_A. Effective linear mobility is plotted for values of V_G -V_T between 5 and 25 V for the In-La-O case with a) T_a = 250 °C and c) T_a = 300 °C. The extracted values of E_A are plotted as a function of ln(V_G -V_T) for each film and at processing temperatures of b) T_a = 250 °C and d) T_a = 300 °C. Linear fits are made to the T_a = 250 °C data while the lines through the T_a = 300 °C data are guides to the eye. 100

5 a) Values of the spatial coherence ratio calculated by fitting Equation (8) to the gate voltage dependence of the In-X-O electron mobility at temperatures between 150 and 275 K. b) Sharing statistics for XO_x polyhedra as calculated from MD simulations of the structures. Numbers of corner-, edge-, and face-sharing polyhedra are shown per computational cell. 102

6 Fitting parameters from the In-X-O EXAFS measurements and ab initio MD simulations plotted as a function of the ionic radius of the X cation normalized to the radius of In^{3+}. a) The change in coordination number, N, for both the In-O and In-M (M = In or X) shells. b) The same for the change in Debye-Waller factor coefficient, $\sigma^2_{R_i}$. 104

7 Ab initio MD simulation results for the In-X-O systems showing the calculated running coordination number, N_{RCN}. The radius r is the distance from the central In atom with a) showing the In-O coordination and b) showing the In-M coordination (where M = In or X). Crystalline In_2O_3 values are also shown for reference. 106

8 Fitting of the O1s XPS peaks for a 10 at% In-La-O film processed at a) T_a = 250 °C and b) T_a = 300 °C. Peak positions were fixed and correspond to fully bound oxygen (M-O-M), partially bound oxygen (M-O(H)) and weakly bound oxygen at the surface or organic impurities (M-O-R). c) The ratio of M-O-M peak area to total area, η_{M-O-M}, is plotted as a function of the X cation size for compositions of 2.5, 5, and 10 at%. 108

PAPER IV

1 (Color online) Radial In-O pair distribution functions in amorphous In-O and In-X-O. In the inset, the calculated average In-O pair correlation function, l_{av}, is plotted for amorphous In-X-O. The horizontal dash line represents the corresponding l_{av} value in amorphous In-O. 120

2 (Color online) Radial pair distribution function of X-O in amorphous In-X-O. The inset shows the average X-O correlation function, l_{av}, in amorphous In-X-O; black bar lines represent the average X-O distance in the corresponding crystalline binary oxides. 124

3 (Color online) Average effective coordination number for In-O and X-O in amorphous In-O and In-X-O calculated according to Eq. 2. 126

4 (Color online) The number of differently coordinated indium atoms, InO_x, in amorphous In-O and In-X-O calculated within 2.36 Å around a central In atom. 127

5 (Color online) Average X-O coordination in crystalline and amorphous oxides as a function of the radial distance r, in Å, from a central X atom. Also included is the average In-O coordination in c-In_2O_3 and a-In-O. Filled (open) symbols represent crystalline (amorphous) oxides. 128

6 (Color online) (Left) Radial In-M distribution function, g_{In-M}(r), where M=In or X=Zn, Ga, Sn, Ge) as a function of distance from an In atom in crystalline In_2O_3 and in amorphous In-O and In-X-O. (Right) Total In-M coordination, where M=In or X=Zn, Ga, Sn, Ge, as a function of distance from an In atom in crystalline In_2O_3 and in amorphous In-O and In-X-O. The inset shows the In-In coordination as a function of distance for the same. 130

7 (Color online) (a) Normalized In-M distance distribution functions, g(r), calculated as a function of radial distance r from a central In atom, in Å, for edge-shared (solid line) and corner-shared (dash line) In-M pairs in amorphous In-O and In-X-O. (b) Normalized In-O-M angle distribution functions, g(θ), calculated for edge-shared (solid line) and corner-shared (dash line) In-M pairs. 132

8 Number of edge-shared and corner-shared (a) In-In pairs and (b) In_6-In_6 pairs in amorphous In-O and In-X-O. Average In-In (triangle) or In_6-In_6 (circle) distance, in Å, and average In-O-In (triangle) or In_6-O-In_6 (circle) angle, in degrees, for the InO_x or InO_6 polyhedra connected via (c) edge-sharing or (d) corner-sharing in amorphous In-O and In-X-O. The horizontal dash line represents the corresponding values averaged for the second and third shells in crystalline In_2O_3 134

9 (Left) Number of edge-shared and corner-shared X-X pairs in a-In-X-O. (Right) Average X-X distance, in Å, and average X-O-X angle, in degrees, for the XO_x polyhedra connected via corner-sharing in amorphous In-X-O. The corresponding values for edge-shared X-X pairs for X=Sn and Ga are given in the text. 137

10 (Color online) The number of In_6 neighbors calculated within a radial cut-off distance of 3.8 Å from a central In_6 in a-In-O and a-In-X-O. The oxides are grouped according to the fractional number of the six-coordinated In atoms, c.f., Fig. 4, that is ∼20 % for a-In-O, and a-ITO; ∼30 % for a-IGO, and a-IZO; and ∼40 % for a-IGeO. 138

11 (Color online) Observed Hall mobility in PLD-grown amorphous In-X-O, X=Zn, Ga, or Sn, as a function of fractional substitution. 141

12 (Color online) Atomic structures of a-In-X-O, X=Zn, Ga, Sn, or Ge, highlighting the InO_6 and XO_x polyhedra only. Small spheres represent oxygen atoms, and large spheres represent In or X atoms. 142

LIST OF TABLES

Table Page

PAPER III

1 Model fit parameters for the TFT measurements calculated from Equation (9) .. 101

2 EXAFS fitting parameters for the first In-O and In-M (M = In or X) shells calculated using Equation (3) 103

3 Structural characteristics of the first In-O and X-O shell as obtained from the ab initio MD simulations. The average coordination N_{ECN} and average distance R_{av} parameters were calculated according to Equations (4) and (5). 105

PAPER IV

1 Average In-O pair correlation function, l_{av} in Å, and effective coordination number, ECN(In-O), cf. Eq. 12, as a function of the number of X atoms, NN_X, located within the radial distance of 3.4 Å from a central In atom. The fractional number of the In atoms, N_{In}, in percent, that have a certain number of X neighbors in the second coordination sphere, i.e., with NN_X=0, 1, 2, 3, or 4, is given in brackets. The total average pair correlation function, $< l_{av} >$, and total average effective coordination number, <ECN(In-O)>, are given in the last column. For comparison, the average In-O pair correlation function is 2.161 Å and the average In-O effective coordination number is 5.0 in a-In-O.... 121

SECTION

1. INTRODUCTION

1.1. CRYSTALLINE TRANSPARENT CONDUCTING OXIDES

In general, materials that conduct electricity are opaque (e.g., metal wire), and the materials that are transparent to light are insulators (e.g., glass). Transparent conducting oxides (TCOs) belong to a class of materials that possess high conductivity (> 100 S/cm) as well as high transparency (> 80 %) to visible light. Introduction of free carriers (electrons) in a material with wide band gap (E_{gap} > 3eV) gives rise to the unique property of being electrically conducting and, at the same time, transparent to visible light. For the first time, TCOs were used on a large scale during the Second World War as defrosting agents [1]. Since then, TCOs have been utilized in a variety of applications, including energy conversion devices (e.g., photovoltaics), flat and touch panel displays, and as heating, antistatic, and optical coatings [2, 3, 4, 5].

Cadmium oxide (CdO) was the first material identified with TCO characteristics; since then, several other transparent conducting oxides have been used as TCO materials, such as indium oxide (In_2O_3), tin oxide (SnO_2), zinc oxide (ZnO), and gallium oxide (Ga_2O_3). All of these materials are wide band gap semiconductors in their undoped stoichiometric form with the optical band gap of 3.5 eV for In_2O_3; 3.6 eV for SnO_2; 3.1 eV for ZnO; 2.3 eV for CdO; and 4.8 eV for Ga_2O_3 [6, 7, 8, 9, 10].

The materials that are alternatives to TCOs are mainly graphene and two-dimensional layered transition metal dichalcogenides, particularly MoS_2 [11]. Graphene, which is a single layer of carbon [12], has a high electron mobility (μ_e) and electrical conductivity. However, graphene lacks a semiconducting gap, whereas MoS_2 has a semiconducting gap and shows excellent electrical and mechanical properties similar to graphene together with

chemical stability. Currently, practical application of both graphene and MoS_2 is limited due to lack of their reliable cost-efficient production on a large scale [13]. In contrast, TCOs and amorphous TCOs (which are the primary focus of this work) have the advantage of easy fabrication on rough surfaces using existing technologies and still possess the combination of high carrier mobility, excellent optical transparency, and mechanical flexibility for a variety of practical applications.

1.1.1. Conductivity in Transparent Conducting Oxides. One of the main desired properties–high electrical conductivity ($\sim 10^3$-10^4 S/cm) –in TCOs is achieved via degenerate doping. The degenerate doping in a wide band gap semiconductor can occur either by (i) changing growth conditions to introduce native defects like anion/cation vacancies or interstitials, or by (ii) external doping with aliovalent substitutional impurities, e.g., In_2O_3:$Sn^{4+}_{In^{3+}}$[14]. Post-transition metal oxides have low formation energy [15]. Hence, oxygen vacancies often coexist with extrinsic dopants, leading to a complex defect chemistry and giving rise to a free carrier density of 10^{17}-10^{19} cm^{-3} even under equilibrium growth conditions [16, 17, 18]. The charge carriers produced in TCOs through degenerate doping can be treated as a free electron gas. Thus, conductivity (σ) can be derived from the Drude model:

$$\sigma = \frac{ne^2\tau}{m^*} = ne\mu \tag{1.1}$$

where n is the carrier concentration, m^* is their effective mass, τ is the relaxation time, and μ is the carrier mobility given by

$$\mu = \frac{e\tau}{m^*} \tag{1.2}$$

It seems that an easy way to enhance conductivity is to increase carrier concentration by introducing more dopant atoms. However, the mobility and therefore, the conductivity is fundamentally limited by the relationship between τ and n [19, 20]. At higher carrier concentrations ($> 10^{20}$ cm^{-3}), ionized impurity scattering, i.e., the Coulomb interactions between electron donors (native point defects or substitutional dopants), limit the carrier

transport. Also, doping can lead to non-homogenous clustering of the dopant atoms, which ultimately increases scattering and reduces carrier mobility.

1.1.2. Optical Properties of Transparent Conducting Oxides. In addition to high conductivity, a very low absorption coefficient in the visible range is the key feature of TCOs. All conventional *n*-type TCOs have highly dispersed conduction band [21, 22, 23, 24, 25], giving rise to the low density of states and therefore low optical absorption. When carriers are introduced by doping, the Fermi level, E_F, significantly moves up above the conduction band minimum, which is called the Burstein-Moss (BM) shift [26, 27] Figure 1.1. The increase in effective band gap provides the optical transition, E_v, from a valence band. In addition, there are transitions from the partially-filled conduction band up into the next empty band, E_c, and also transitions inside the conduction band, E_i. The transition E_v helps to broaden the transparency window, whereas the other two transitions E_c and E_i lead to absorption [25].

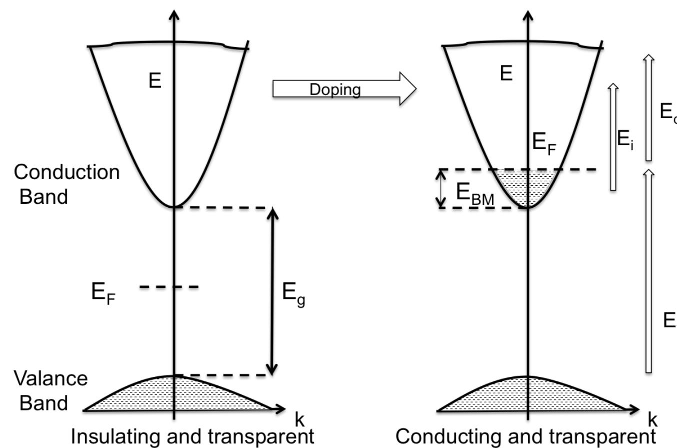

Figure 1.1. (Left) Schematic electronic band structure of insulating transparent oxide, with band gap E_g and a dispersed parabolic conduction band which originates from interactions between metal *s* and oxygen *p* states. (Right) A schematic band structure of transparent and conducting oxide, where conductivity results from the shift of Fermi level E_F up into the conduction band via a Burstein-Moss shift, E_{BM}.

Further, the relation between the conductivity and optical transparency can be explained by taking into account the harmonic motion of the electrons in response to the

time-varying electric field of the radiation:

$$\frac{m^* d^2 x}{dt^2} = \frac{-ne^2 x}{\epsilon} \tag{1.3}$$

where ϵ, n, and e are the dielectric constant of the material, the electron density, and the electric charge, respectively. From the above equation, the so-called plasma frequency ω_p can be expressed as:

$$\omega_p = \left(\frac{ne^2}{\epsilon m^*}\right)^{1/2} \tag{1.4}$$

By using Equation 1.1, plasma frequency can be written in terms of the conductivity:

$$\omega_p^2 = \frac{\sigma}{\epsilon \tau} = \frac{ne\mu_e}{\epsilon \tau} \tag{1.5}$$

Electromagnetic waves at plasma frequency striking the material undergo resonant absorption. However, below plasma frequency, electromagnetic waves will be reflected, and above the plasma frequency, the inertial mass of the electron can not be overcome, so the material becomes transparent. At still higher frequencies, photon energy will be adequate to excite electrons from the valence band to the conduction band and also from the conduction band to the next empty conduction band. Once electrons are excited, the absorption of the electromagnetic radiation occurs. Thus, by changing the plasma frequency, i.e., by adjusting the number of charge carriers, the light of selective frequency can be transmitted or blocked by the TCOs.

As discussed above, the unique electronic structure of TCOs is characterized by excellent mobility for the carriers generated due to their small effective mass; low optical absorption due to large band gap and low density of states in the conduction band. In these metal oxides, the conduction band arises mainly from metal *ns* orbitals whereas the valence band maximum (VBM) is formed primarily from O 2*p* orbitals. Localized O 2*p* orbitals at VBM cause poor conduction of holes, which are trapped by O ions [1, 28]. Both

properties, i.e., localized orbitals and the hole-trapping ions are the main obstacle in the development of *p*-type TCOs where holes are the carriers. There have been several efforts in the development of *p*-type TCOs by modifying band structure and band energy using metal orbitals with energy close to O 2*p* or extended anion orbitals using the materials mainly containing copper [13]. The *p*-type TCOs are beyond the scope of this work.

1.2. AMORPHOUS OXIDES

1.2.1. Brief History of Amorphous Oxides. The first reported work on amorphous oxide semiconductors was from Denton *et al.* in 1954, on electronic conductive glass having a significant amount of V_2O_5 [29]. Since then, the use of the term glass as an insulator was no longer appropriate. The electronic conductivity in these oxides is mainly by hops of the electron from donor to donor. At room temperature, the mobility of electrons observed in these oxides was in the order of 10^{-4}cm^2/Vs. Such low electron mobility and intense coloration due to absorption arising from $d-d$ transition make them unqualified as a transparent conducting oxide [30]. Pioneering studies of amorphous transparent conductors were the study by Ito *et al.* 1987 and by Bellingham *et al.* 1990 [31, 32]. The former was on the amorphous to the crystalline phase transition of In_2O_3 thin film, and the later was a detailed analysis of the electrical and optical properties of amorphous In_2O_3 (*a*-IO). In their study, the carrier concentration was observed at about 10^{20} cm^{-3} and resistivities near 10^{-4} Ω cm, which were comparable to those obtained with crystalline films. The study of amorphous In_2O_3 motivated general consideration of amorphous oxide semiconductors (AOSs) through studies of Cd_2GeO_4 [33, 34], $AgSbO_3$[35], $InGaZnO_4$[36]. $CdPbO_5$[37], and $MgIn_2O_7$[38]. Several properties of these materials were explained by considering the amorphous Cd_2GeO_4 system [33, 34]. It showed the eleven orders of magnitude increase in conductivity (up to 10^2 Scm^{-1}) by ion implantation of appropriate cations. The Hall mobility with electron carrier concentration of 10^{20} cm^{-3} was 10-12 cm^2 V^{-1} s^{-1} [39].

Hosono *et al.* proposed a working hypothesis for an amorphous oxide semiconductor [40, 41], where a delocalized *s* orbital of heavy post-transition metal oxide forms the dispersed conduction band with large overlap between the relevant orbitals with the overlap being insensitive to structural randomness in the structure. The research area of the amorphous oxide has grown significantly with the verification of their hypothesis and demonstration of an “invisible" transistor in 2004 [42]. To date, researchers have explored many *n*-type amorphous oxide semiconductor compositions, mainly including any combination of In, Zn, Ga, and Sn. Here we list those that have been studied for their good optical, electrical, and mechanical properties: i) ternary systems In-Sn-O (a-ITO), In-Zn-O (a-IZO), In-Ga-O (a-IGO), Zn-Sn-O (ZTO) and Ga-Sn-O (a-GTO) [43, 44, 45, 46, 47, 48] and ii) quaternary In-Ga-Zn-O (a-IGZO) [49, 50, 51, 52, 53], Zn-Sn-In-O (a-ZITO) [54, 55, 56] and Ga-Sn-Zn-O (a-GTZO) [57].

1.2.2. Comparative Properties of Crystalline and Amorphous Oxides. Amorphous oxide semiconductors are getting more attention in technological applications in recent days [58] due to their ability of large-area deposition of a uniform film at low temperatures [42, 59] combined with excellent electrical properties. Low processing temperature makes these materials good candidates for deposition on plastic or even paper [42, 60]. Other important properties of amorphous oxides, such as being free from grain boundaries, having good etchability [42, 61, 62], having low surface roughness [63, 64], and being less prone to fracture, are the key reasons why amorphous oxide semiconductors became more appealing technologically than their crystalline counterparts. Comparative properties of crystalline and amorphous oxide semiconductors in different aspects are described below.

1.2.2.1. Structural properties. Both amorphous and crystalline oxides have metal-oxygen (M-O) polyhedra as basic building blocks. A notable difference of amorphous oxides with crystalline counterparts is the arrangement of M-O polyhedra, Fig. 1.2. In crystalline TCOs, the M-O polyhedra are arranged by maintaining perfect periodicity of

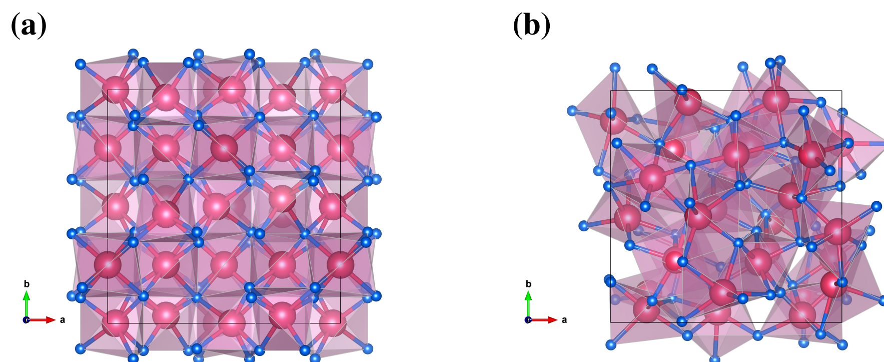

Figure 1.2. The atomic structure of (a) c-In_2O_3: represented by the periodic arrangement of highly symmetric InO polyhedra and (b) a-InO: represented by the random collection of distorted InO polyhedra. Red balls denote the In atoms, whereas small blue ball represents the O atoms.

the crystal, while in the amorphous oxide, there is a random network of distorted polyhedra with no long range ordering. Even though the first coordination sphere of the cation remains preserved in amorphous form, there is the significant change in the second and the third coordination spheres, i.e., the M-M arrangement. Moreover, amorphization may introduce other structurally relevant defects such as porosity that will decrease density of the material (ρ for c-IGZO is 6.33 gcm^{-3} and for a-IGZO 5.8 gcm^{-3} [65]). Annealing an amorphous structure below the crystalline transition temperature (T_g) leads to internal atomic rearrangement without long-range migration, which helps in reducing local defects and porosity of the material [65, 66].

1.2.2.2. Optical properties. The optical band gaps in both crystalline and amorphous conducting oxides are > 3eV due to the Burstein-Moss shift, which allows technological application of them as a transparent electrode. In comparison to crystalline transparent conducting oxides, the optical band gap is slightly decreased in amorphous form due to the formation of tail states in the gap, yet amorphous oxides remain transparent in the visible range of the electromagnetic spectrum. Optical properties of amorphous oxides and the formation of tail states will be discussed in detail in Section 1.3.3.

1.2.2.3. Transport properties. In oxide semiconductors, the essential feature of the electronic band structure originates from the M-O interactions [24, 67]. The electron effective mass remains nearly unchanged upon amorphization [68]; and the electron mobility remains the same order of magnitude as in crystalline oxides [69]. Also, the thermal conductivity in amorphous oxides is almost the same as in crystalline oxides [70]. Long-range structural disorder in amorphous oxides reduces scattering mean free path; on the other hand, lack of grain boundaries makes the electronic properties uniform over large area.

The oxygen nonstoichiometry in both crystalline and amorphous transparent conducting oxides introduces n-type carriers [30]. In contrast to crystalline conducting oxides where doping by aliovalent cations such as Sn^{4+} on In^{3+} in In_2O_3 increases the carrier concentration by an order of magnitude, the carrier concentration in amorphous oxides does not vary with cation composition as in the crystalline oxides. In c-In_2O_3, oxygen vacancy and substitutional doping give carrier density in the order of 10^{19} cm^{-3} and 10^{20} cm^{-3}, respectively, while in both a-IO and a-ITO, the number of carriers is in the order of 10^{20} cm^{-3}. The mechanism of controlling carrier density in amorphous oxides will be discussed in Section 1.3.1

1.2.2.4. Mechanical and surface properties. Transparent conducting oxide has polar crystallographic axes, which can give rise to the surface with preferred cation or anion. These surfaces act as a carrier depletion layer [71]. Moreover, at the surface, the Fermi level lies below the valance band despite degenerate doping [71]. The surface properties affect the interface properties of material significantly.

The surface and the mechanical properties of transparent conducting oxides are important, especially for its large area applications and application in flexible electronics. In contrast to crystalline oxides, which are anisotropic, possess grain boundaries, and have rough surfaces, amorphous oxides are often isotropic, so they are free from dislocations, grain boundaries and have smooth surfaces. Furthermore, crystalline TCOs are brittle, i.e.,

they lack mechanical flexibility, whereas amorphous oxides are less prone to fracture and are bendable with curvature radius as large as 3 cm [42]. A variation of the gap and the optical properties at strain arises due to the change in cationic coordination and bond length [72]. These structural variations are less pronounced for amorphous material compared to the crystalline one, which makes amorphous materials more appealing in flexible electronic applications [60].

1.2.3. Covalent vs. Ionic Amorphous Oxides. Amorphous materials and glasses have a long history of research interest from both fundamental and technological points of view. Some of the most commonly used glasses are $((SiO_2)_{0.8}(Na_2O)_{0.2})$ in windows and $(Fe_{0.8}B_{0.2})$ in transformer cores.

It is important to stress the difference between amorphous covalent semiconductors (e.g., Si: H), whose device performance and applications are limited by the properties inherent to this material, with ionic amorphous oxide semiconductors. In covalent semiconductors, the conduction band arises mainly from directional *p*-orbitals (in Si sp^3 orbitals), the magnitude of the overlap between the vacant orbitals of neighboring atoms is very sensitive to variations in the bond angle upon amorphization. The illustrative comparison of orbitals and their overlapping in Si and transition metal oxide semiconductor is presented schematically in Fig. 1.3. As a result, the effective mass is significantly affected by the crystalline to amorphous transition. Moreover, the high concentration of deep and localized states (e.g., dangling bonds) below the bottom of the conduction band and on top of the valence band are created upon amorphization that causes further decrease in mobility due to scattering [73]. Specifically, the mobility in crystalline Si is 1500 cm^2/Vs, whereas, in a-Si it is reduced to 0.1 cm^2/Vs. In contrast, transparent oxides consist of post-transition metal cations with the electronic configuration $(n-1)d^{10}ns^0$ ($n \geqslant 4$). The magnitude of the overlap between the vacant orbitals of neighboring atoms is insensitive to the bond angle

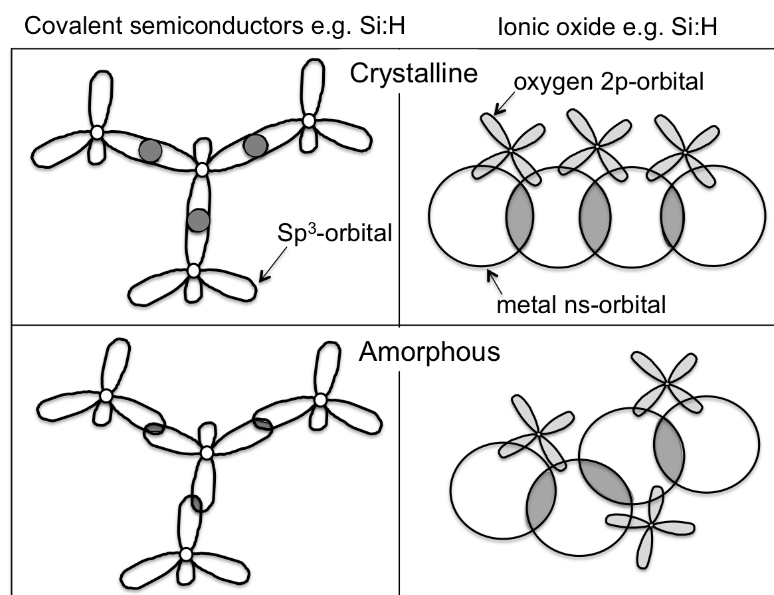

Figure 1.3. Schematic drawing of atomic orbital overlap for conventional compound semiconductor (a-Si:H) and ionic oxide semiconductors (a-IGZO) as adopted from Ref.[43].

distribution due to isotropic nature of the spherically symmetric *s*-orbitals. As a consequence, ionic amorphous materials have mobility comparable to crystalline counterparts and orders of magnitude greater than that of amorphous Si [58, 74].

1.2.4. Experimental Growth Techniques. In experiment, deposition geometry like source-to-substrate distance, the rate of vacuum deposition pressure will have an effect on MO film properties. The most commonly used experimental techniques to grow metal oxides [1, 13, 58] are presented below.

1.2.4.1. Thermal deposition. In this method, the metal itself or its oxides in desired proportion are evaporated in a vacuum. The proper substrate is used to deposit the material evaporated, and the substrate is kept at a higher temperature to allow fast reaction between the constituent ions. Also, the appropriate amount of oxygen must be supplied on the background to have the desired composition. Sometimes post annealing of the deposited material is performed in an oxygen-rich environment to get the desired oxide composition.

1.2.4.2. Sputtering. In sputtering, particles are ejected from the solid target due to the bombardment of gas ions from the plasma. The magnetic field is applied to the target to intensify bombardment of the ions and uniform film deposition. In this process, materials are deposited at room temperature so plastic can be used as the substrate. To achieve the desired features on oxide, controlling parameters such as variation of oxygen partial pressure and sputtering power are used.

1.2.4.3. Pulsed-laser deposition. Pulsed laser deposition (PLD) is a vapor deposition technique. In this process, a high pulse laser beam is used to melt the target material that is to be deposited. The melted material is vaporized from the target in a plasma plume, which is deposited as a thin film on a substrate at required temperature (deposition temperature). Depending upon the material requirement, the process can occur in an ultra high vacuum or background gas such as oxygen for metal oxide deposition.

1.2.4.4. Atomic layer deposition. In the atomic layer deposition process (ALD), thin films are deposited on a substrate by exposing its surface to alternate gaseous species. In this method, different species are never present simultaneously in the reactor, unlike the chemical vapor deposition process. Instead, they are inserted as a series of non-overlapping pulses in a self-limiting way to allow consumption of all the species and termination of the reaction before another pulse arrives.

1.2.4.5. Spin-coating. Spin coating is used to deposit a thin film on a flat substrate. Coating material in the form of a solution is placed on the substrate that is at rest or rotating at slow speed. Then, the substrate is rotated at high speed so that centrifugal force spreads the coating material. Rotation is maintained until the film reaches the desired thickness. The nature of the solvent and the speed of rotation determines the quality and thickness of the film deposited.

1.2.4.6. Spray coating (spray pyrolysis). In this method, the liquid droplet containing precursors are sprayed onto preheated substrate. The reaction takes place at the surface, giving rise to the volatile product leaving a film of desired material on the substrate.

1.2.4.7. Printing. When the printing method is used to create electronic devices on various substrates, it uses the simultaneous method of film deposition and the design at low temperature. The most commonly used printing techniques are gravure, flexography and ink-jet. In this method, electrically functional devices are deposited on the substrate. Printed electronics are expected to be low-cost, low-performance electronics for applications.

1.2.5. Theoretical Methods of Generating Amorphous Structures. To model an amorphous structure theoretically, one requires to adopt a scientific method which can give physically meaningful structure by creating a computer model that mimics the realistic compound and the environment close to the experimental conditions.

1.2.5.1. Monte carlo technique. Monte Carlo simulation is an early computation technique used in simulation of materials. In this approach, atoms are enclosed inside a simulation box and are moved randomly. After each complete move, radial distribution function is computed, and a move is accepted if the radial distribution becomes close to the experimental distribution, otherwise the move will be considered with Metropolis probability. Later, the so-called Reverse Monte Carlo (RMC) method, which is the variation of Metropolis Monte Carlo (MMC), is used instead of Metropolis probability; the probability is replaced with a normal distribution with width σ[75]. This method gives excellent agreement with diffraction data but chemical properties might be far from the reality. Mostly the amorphous glasses, e.g., a-Si and a-Ge, were studied with the help of the Monte-Carlo method for their structural characterization, namely coordination statistics and ring-like structure formations in the amorphous phase.

1.2.5.2. Classical molecular dynamics (MD). Nowadays, a large number of atomistic structure simulations are done using molecular dynamics. Starting with the interatomic potential, one has to integrate the Newtonian equations of motion for all atomic species that are enclosed inside a box with suitable periodic boundary conditions. In modeling of amorphous oxides, typically a liquid is formed at a temperature fairly high above the

melting point and gradually cooled to get an amorphous solid. Molecular dynamics is deterministic and provides full static and dynamic information of all particles from complete microscopic trajectories. Because it is computationally less expensive, this method is still used in modeling of amorphous glasses [73, 76, 77] and amorphous oxides [68, 78, 79] at large scale to study some of the properties, e.g., structural, thermal, mechanical. The simulated quench for semiconducting elements performed using effective pair and volume force derived from pseudo potential- and linear-response theories is found to give discrepancies with experimental data in the metal-semiconductor transition [80].

1.2.5.3. *Ab initio* or Quantum mechanical molecular dynamics. In contrast to classical molecular dynamics, potential and force are calculated before moving the ions in this method, i.e., the quantum mechanical equation for many electron systems is solved before solving Newtonian equations of motion. In this approach, the quantum nature of the chemical bond is taken into account for each and every ionic step so that it captures underlying electronic details of the material microscopic properties. The *ab initio* molecular dynamics is becoming a reliable method in the study of amorphous oxide semiconductors [47, 50, 81]. Major advantages of *ab initio* molecular dynamics are summarized as follows: (i) forces acting on the nuclei are calculated on the fly from first principles; (ii) the density of electronic states and related properties can be calculated; (iii) the reactions that involve the breaking or formation of the chemical bonds are taken into account; and (iv) energy is minimized with respect to certain density functional so problem of nonadiabaticity does not arise. The *ab initio* molecular dynamics will be discussed in detail in Section 2.5 as the method used in the present work.

1.3. PROPERTIES OF AMORPHOUS CONDUCTING AND SEMICONDUCTING OXIDES

1.3.1. Transport in Amorphous Oxides. For an excellent transport behavior in an amorphous semiconductor, the necessary conditions are controllable carrier concentration

and high mobility. Experimentally, it was shown that one way of generating carriers in amorphous oxide is to alter the oxygen stoichiometry, which can be done by either controlling the oxygen gas pressure during growth or by annealing the film in excess oxygen environment as a post processing step. Most of the amorphous oxide semiconductors exist in the multicomponent form, as a mixture of several post-transition metals, e.g., In, Sn, Zn, and Ga. A clear understanding of the effect of different constituent ions is essential to overcome the difficulty of having controllable carrier concentration and the desired mobility. The presence of various ions having different charges introduces the perturbation in regular metal-oxide networks, making it easier to achieve an amorphous phase [82].

The small effective mass of electrons for high mobility of carriers is mainly due to unoccupied *s* orbitals in the conduction band. Hence, one of the primary requirements for a good transparent conductor is to have the majority of In, Ga, Zn, or Sn in the system. These ions have different effects on the properties of amorphous oxide, e.g., a-IZO shows higher mobility with higher carrier concentration compared to the material where some of the Zn atoms are replaced by Ga atoms, a-IGZO [83]. In Fig. 1.4, we can see that carrier concentration in the a-IGZO is reduced below 10^{15} cm^{-3} (from 10^{20} cm^{-3}) by changing oxygen pressure from 0.1 Pa to 7 Pa. At the same time, it is hard to reduce carriers in a-IZO below 10^{17} cm^{-3} in contrast to a-IGZO. This indicates that, in addition to the external change in the oxygen pressure, the presence of Ga in the material helps to reduce the oxygen deficiency due to a stronger Ga-O bond in comparison to the In-O and Zn-O bonds, which may limit spontaneous generation of the carriers [49]. Thus, addition of an appropriate fraction of different cations and growth environment is essential to obtain stable amorphous oxide with the desired properties [82]. Also, it is possible to generate carriers by using the external electric field when they are used as thin film transistors. The formation of defect states and their role in electronic transport and material properties will be discussed in detail in Section 1.3.2.

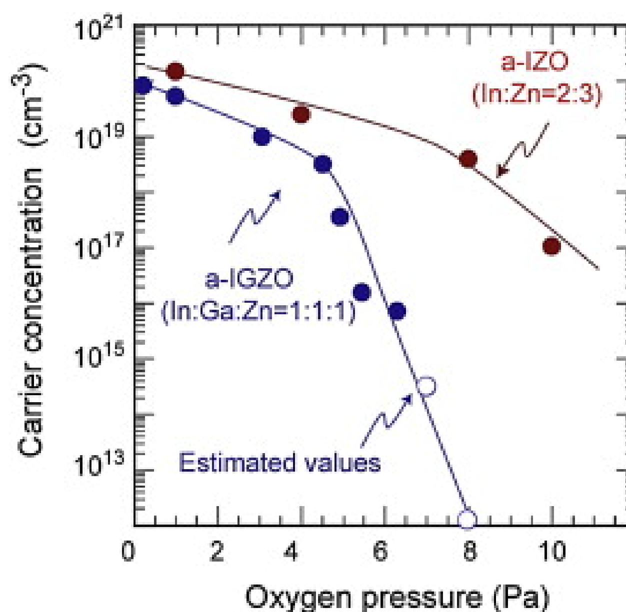

Figure 1.4. The carrier concentration as a function of O_2 pressure during the deposition in a-IGZO and a-IZO [30].

1.3.2. Subgap States in Amorphous Oxides. The structure of amorphous oxide promotes the formation of subgap states (the tail states). The disorder-induced effects at the bottom of the conduction band are negligible, as the conduction band is formed primarily from spherical 4*s* or 5*s* orbitals of the metal atom, which are insensitive to the structural disorder. In contrast, the top of the valence band is formed mainly from oxygen *p*-orbitals which are directional and thus more strongly affected by the disorder [50, 84]. Development of subgap states within the electronic band affects transport properties and optical transparency [85, 86]. The subgap states close to the valence band maximum can form flat bands above the top of the valence band VB, Fig. 1.5, which may reduce the hole mobility if hole carriers exist [87].

Due to the significant dependence of the carrier concentration on the oxygen pressure during growth, it is commonly assumed that oxygen vacancy is responsible for the conductivity in amorphous oxides; it was shown that oxygen vacancy creates a shallow donor defect near the conduction band minimum, which may provide the carriers [88], Fig.

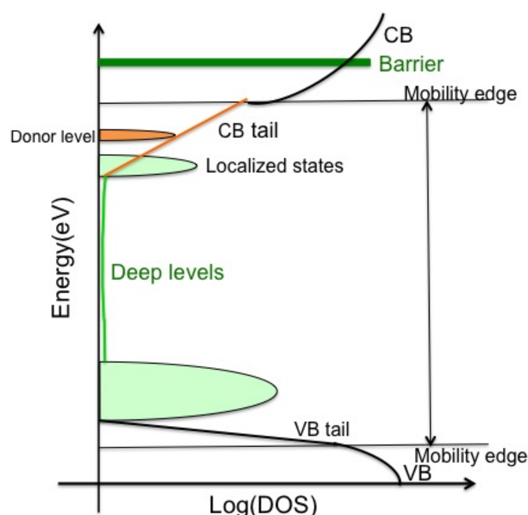

Figure 1.5. Schematic models of subgap DOS in typical amorphous oxides adopted from Ref. [82]. VB = valence band, CB = conduction band

1.5. Also, it was believed that oxygen vacancies are responsible for deep subgap states [65, 89, 90, 91]. However, an oxygen vacancy V_O in an amorphous structure is not well defined and is indistinguishable from metal interstitial (M_i) that may appear in one of the following equivalent forms O-(M-M)-O=O-(M-V_O-M)=O-(M-M_i)-O [92].

Some of the recent experimental and theoretical studies on amorphous a-IGZO, a-IZO, and a-ZTO have found the increase in deep subgap states with a rise in oxygen content [85, 86, 93]. They have pointed that the subgap states below the lower half of the band gap, and the deep localized defect levels are due to the undercoordinated oxygen atom, and the subgap states in the upper part of the band gap are caused by defects related to the local oxygen deficiency. Subgap states in the upper part of the band gap are further attributed to nanocrystalline indium in indium-based oxides or the formation of M-M complexes [48, 86]. However, the origin of both shallow and deep defects in amorphous oxide is still a topic of debate [85, 87, 94]. It requires more thorough understanding and treatment of the defects to achieve material stability during application [88].

1.3.3. Optical Properties of Amorphous Oxides. As mentioned earlier, structural disorder reduces the band gap in the amorphous oxide; however, short-range interaction,

i.e., the nearest neighbor M-O interaction (which is preserved during amorphization) and the Burstein-Moss shift, keeps them optically transparent due to the low absorption in the visible range. A high energy transition occurs due to the transition of electrons from valence band to the conduction band, as shown in Fig.1.1. In the experimental study, the band gap is estimated from change in the absorption coefficient α at the absorption edge [53, 95]. The absorption coefficient can be calculated by using transmitted intensity, I, the incident intensity, I_0, and the thickness d of the thin film as:

$$I = I_0 e^{-\alpha d} \tag{1.6}$$

The optical band gap values of amorphous oxides are usually determined from a Tauc relation [96], which has the form

$$(\alpha h\nu)^{1/2} = c(h\nu - E_g) \tag{1.7}$$

where $h\nu$ is the incident photon energy, c is a constant, and E_g is the optical band gap of the material. Also, optical spectra follow Urbach's law, which can be used to check disorder in the film [97]. In the theoretical calculation, the absorption coefficient is calculated from extinction coefficient, κ, as:

$$\alpha = \frac{4\pi\kappa}{\lambda}, \tag{1.8}$$

where extinction coefficient is determined from the relation of complex dielectric function ϵ as:

$$\epsilon = (n + i\kappa)^2 \tag{1.9}$$

Here n is the refractive index of the material. The imaginary and real parts of the complex dielectric function are related by the Kramers-Kronig relations. The expression for refractive index and extinction coefficient are given in Section 2.4.

Studies of the optical spectra provide the information about subgap states and also the disorderness in the film. The decrease in the band gap value and film transparency during transition from crystalline to amorphous form can be regained by annealing the film in the appropriate environment [82, 85] or by incorporating the appropriate cations in the material.

2. METHODS AND APPROACH

2.1. INTRODUCTION

Computer simulations of solids, also called computational experiments, bridge the gap between phenomenological description and experimental observation. They are becoming an important tool to characterize properties of materials, from the nanoscale up to bulk materials and devices [98]. The combination of state-of-the-art methodology, efficient algorithm innovations, and ever-increasing computer power is leading towards a modern revolution in materials modeling [99]. Various solid-state properties are explained at different levels of sophistication by treating electron-electron interaction differently [100, 101]. The selection of methodology for the calculation depends on a choice of the problem of interest. One approach to deal with many electron systems is the band theory of solids, which has emerged from the self-consistent field approximation. In this method, each electron is assumed to move independently in the average effective field produced by nuclei and remaining electrons. A one-particle Schrödinger equation governs the motion of each electron. This approach has been proven to be immensely successful, particularly in the physics of semiconductors and metals. It provides us with convenient first-principles, or *ab-initio* methods, such as the density functional theory (DFT) [102, 103]. One can use DFT as a tool not only to verify but also to predict the characteristics of materials with significant quantitative accuracy before it is made or tested in a lab.

As discussed in Section , amorphous materials are of keen interest in material science on both the fundamental and technological levels. In amorphous material, the primary challenge is a precise characterization of the structural features, or in other words, the clear understanding of the atomic structure of the network. For a crystalline structure, the diffraction experiment can give the complete set of atomic coordinates whereas for liquid

and amorphous materials, commonly used experimental techniques to identify the structure are X-ray spectroscopy and extended X-ray absorption fine structure (EXAFS)[104]. The latter provides reliable pair distribution functions, yet it can not give the information beyond the second or third shell. Therefore, to gain sufficient understanding of the structure of amorphous materials, the laboratory experiment should be supplemented with a computer simulation [105].

In addition to the methods mentioned under the Section 1.2.5, methods used to generate amorphous materials in computation are *accretion*, i.e., the sequential addition of atoms to a growing cluster [76], and *randomization and relaxation* [77]. Both methods are strongly biased by the detail of growth, the randomization algorithm, and the interatomic force field used during the relaxation. Molecular dynamics (MD) is preferred over these methods, in which results depend only on the quality of interatomic potential. However, due to inability of the empirical potentials to describe in detail the chemical bonding process in many important systems, and also due to complexity in constructing empirical two- and three-body potentials with transferability from a liquid phase to amorphous phase, first-principles based approach, i.e., *ab initio* molecular dynamics technique was developed.

To generate amorphous oxides in our study, we have used *ab initio* MD, which is based on the density functional approach [106]. *Ab initio* MD will be discussed in more detail in Section 2.5. Below, we introduce the DFT approach and the approximations currently employed within this formalism.

2.2. DENSITY FUNCTIONAL THEORY

Density functional theory (DFT) is one of the most widely used electronic structure calculation techniques to study the ground state properties of a solid. In the DFT, the electronic orbitals are the solutions of a many-electron Schrödinger equation, which depend on the electron density rather than on electron spin orbital as in the Hartree-Fock approach

[107]. The basic approach of the DFT is to approximate the electron correlation using a general functional of the electron density. For an n electron system, the density of the electrons can be defined by the wave functions:

$$n(\mathbf{r}) = \langle \psi(\mathbf{r}) | \psi(\mathbf{r}) \rangle \tag{2.1}$$

One can express the property of a system such as total energy as a functional of its electron density instead of its wave function.

The notion of expressing the characteristic of the system by the density of homogeneous electron gas started with the Thomas-Fermi approximation [108, 109]. The era of modern DFT started from Hohenberg and Kohn Theorems in 1964 which are stated as [102]:

Theorem i): *For any system of interacting particles in an external potential $V_{ext}(\mathbf{r})$, the density is uniquely determined.*

Theorem ii): *A universal functional for the energy $E[n]$ can be defined in terms of the density $n(\mathbf{r})$, which is valid for any external potential $V_{ext}(\mathbf{r})$. The exact ground state is the global minimum value of this functional with correct ground state density.*

The first theorem implies that all the properties of the system can be determined from the ground state electron density. The second theorem introduces the energy functional and provides a method to find ground state density of the system. Following from the theorems, the complicated problem of determining all ground state characteristics of the system is now reduced to the problem of finding the minimum of Hohenberg-Kohn functional, which can be expressed as [102]:

$$E[n] = F[n] + \int d\mathbf{r} n(\mathbf{r}) V_{ext}(\mathbf{r}) \tag{2.2}$$

where $E[n]$ is a total energy functional, and $F[n]$ is a universal functional, which is independent from the number of particles and the external potential. The ground state

energy is obtained by minimizing the total energy functional corresponding to the ground state energy density, $E_0[n_0]$. The functional, $F[n]$, is separated into kinetic energy, $T[n]$, Hartree (Coulomb), $E_{coul}[n]$, and exchange-correlation (XC), $E_{xc}[n]$

$$F[n] = T[n] + E_{coul}[n] + E_{xc}[nc]. \tag{2.3}$$

The ground state energy of the system can be obtained by solving the single particle Schrödinger-like equations, also called the Kohn-Sham (K-S) equations [103]:

$$H_{KS}\psi_i = \varepsilon_i\psi_i \tag{2.4}$$

$$\left[-\frac{1}{2}\,\nabla^2 + v_{eff}(\mathbf{r})\right]\psi_i = \varepsilon_i\psi_i \tag{2.5}$$

where H_{KS} represents the one electron K-S Hamiltonian, and $v_{eff}(r)$ represents the effective potential, which is expressed in terms of sum of the external potential (v_{ext}), Hartree (Coulomb) potential (v_H), and exchange correlation potential (v_{XC})

$$v_{eff} = v_{ext} + v_H + v_{XC} = v_{ext} + \int \frac{n(\mathbf{r}')}{|\mathbf{r} - \mathbf{r}'|} d\mathbf{r}' + \frac{\delta E_{XC}}{\delta[n(\mathbf{r})]}. \tag{2.6}$$

The Coulomb potential and the exchange-correlation potential both contain electron density and the electron density is determined from the potential, which requires Equation 2.5 to be solved self-consistently.

2.2.1. Exchange-Correlation Functional. The exchange-correlation potential includes all the many-body interactions, which are missing in the classical Hartree interaction potential. The biggest problem of the DFT is finding the exact functional for exchange and correlations, which are not known except for the free electron gas. Some of the most widely used approximations are summarized below.

2.2.1.1. The local density approximation. The local-density approximation is the most successful and well-tested approximation for the exchange-correlation energy. In

this approximation, the assumption made is that the local exchange-correlation energy per particle (energy density) depends on the local density. The exchange-correlation is also equal to the exchange-correlation energy density of homogeneous electron gas, provided homogeneous electron gas has the same density with a neutralizing positive background. The exchange-correlation energy can be written in terms of exchange-correlation energy density (ε_{XC}) as:

$$E_{XC}^{LDA} \approx \int n(\mathbf{r})\varepsilon_{XC}[n(\mathbf{r})]d\mathbf{r} \tag{2.7}$$

The exchange-correlation energy density ε_{XC} can be separable in terms of exchange and correlation part as:

$$\varepsilon_{XC} = \varepsilon_X + \varepsilon_C \tag{2.8}$$

where ε_X is the exchange component that denotes the exchange energy of an electron in a uniform electron gas and is defined as:

$$\varepsilon_X = -\frac{3}{4}\left[\frac{3n(\mathbf{r})}{\pi}\right]^{\frac{1}{3}} \tag{2.9}$$

The correlation term, ε_c, is obtained from numerical Quantum Monte-Carlo simulations on the homogeneous electron gas [110]. The LDA approximation works more accurately for the system with slowly changing density, as it assumes density is locally constant. The LDA overestimates the binding energy of solids and molecules, hence it underestimates the bond lengths. For the semiconductors, it underestimates band gaps, e.g., LDA predicts Ge to be metallic [111].

2.2.1.2. The generalized gradient approximation. The generalized gradient approximation (GGA) came as a possible improvement over the LDA. The GGA gives a good estimate of the total energies of the molecules [112, 113]. The general form of the

exchange-correlation functional in GGA approximation can be written as:

$$E_{XC}^{GGA}[n] = \int \varepsilon_{XC}(n, |\nabla n| \nabla^2 n) d\mathbf{r} \tag{2.10}$$

At the current stage, GGA approximation is popular among computational chemists as it gives reliable results for all primary types of the chemical bonds. In this work, we have used the GGA with Perdew-Buke-Ernzerhof (PBE) [114, 115] functionals as implemented in the Vienna *ab initio* Simulation Package (VASP) [105, 116, 117, 118].

The exchange energy of PBE approximation can be defined as:

$$E_x^{PBE} = \int d\mathbf{r} n(\mathbf{r}) \varepsilon_x^{PBE}(n(\mathbf{r}), s(\mathbf{r})) \tag{2.11}$$

where $s=|\nabla|/(2\kappa_F n)$ is the reduced gradient with $\kappa_F = (3\pi^2 n)^{1/3}$. The PBE exchange energy density is given by the product of LDA exchange and an enhancement factor, F_x^{PBE}, which depends on $s(r)$, i.e.,

$$\varepsilon_x^{PBE}(n(\mathbf{r}), s(\mathbf{r})) = \varepsilon_x^{LDA}(n(\mathbf{r}) \times F_x^{PBE}(s(\mathbf{r}))) \tag{2.12}$$

$$F_x^{PBE}(s) = -\frac{8}{9} \int_0^{\infty} dy J^{PBE}(s, y) \tag{2.13}$$

where $J^{PBE}(s, y)$ is the PBE exchange hole.

2.2.1.3. The hybrid functional. The LDA and GGA approximation are successful in accurately estimating properties of the materials such as lattice constant, and bulk properties such as total energy. However, LDA and GGA underestimate the band gaps. Improvement in the band gap calculation is accomplished by application of the so-called hybrid functionals. The hybrid functionals are obtained by admixing an adjusted value of the Hartree-Fock (HF) exchange to the GGA functional.

To date, several hybrid functionals have been proposed. The hybrid functional HSE06, introduced by Heyd, Scuseria, and Ernzerhof [119, 120], is one of the most widely used functionals. This functional replaces the slow decaying long-range part of the Hartree-Fock (HF) exchange by the analogous density functional counterpart. In HSE06, the expression for the exchange-correlation energy takes the following form:

$$E_{XC}^{HSE} = \frac{1}{4}E_X^{SR}(\mu) + \frac{3}{4}E_X^{PBE,SR}(\mu) + E_X^{PBE,LR}(\mu) + E_C^{PBE} \tag{2.14}$$

where SR and LR refer to the short- and long-range part of individual exchange interaction, and μ represents the parameter used to define the scale of the Coulomb kernel whose value ranges between 0.2 to 0.3Å. In molecules and solids, this approach is capable of providing the results of the lattice parameter, bulk moduli, formation energy, binding energy, and the band gap of semiconductors and insulators with experimental accuracy. Due to there capabilities, the popularity of HSE in the electronic structure calculations is increasing [121]. We have used the HSE06 functional to correctly estimate the electronic states and optical band gaps in our study.

2.3. METHOD FOR CALCULATING BAND STRUCTURE

Electronic structure of solids is often determined using periodic boundary conditions. The periodic symmetry of the perfect crystals and the use of periodic supercell for the study of non-periodic systems such as amorphous solids allows one to reduce the problem. The use of periodic boundary in modeling the system makes it convinent to handle with present computational resources. From the solution of the Khon-Sham equation (Eg. 2.5), one can calculate the electron eigenstates and related properties for the solid system represented by the atom within the cell. The effective potential, $V_{eff}(\mathbf{r})$ of Kohn-Sham

Hamiltonian, will be periodic with the lattice vector **R** of the cell, i.e.,

$$V_{eff}(\mathbf{r}) = V_{eff}(\mathbf{r} + \mathbf{R}) \tag{2.15}$$

Bloch's orbitals $\phi_{n\mathbf{k}}$ can be written as the product of the plane wave and a periodic function, $u_{n\mathbf{k}}(\mathbf{r})$.

$$\phi_{n\mathbf{k}}(\mathbf{r}) = e^{i\mathbf{k}.\mathbf{r}} u_{n\mathbf{k}(\mathbf{r})} \tag{2.16}$$

where **k** is the wavector and n is the band index. Since the function $u_{n\mathbf{k}}$ is periodic with the periodicity of the lattice, i.e.,

$$u_{n\mathbf{k}}(\mathbf{r}) = u_{n\mathbf{k}}(\mathbf{r} + \mathbf{R}), \tag{2.17}$$

for any energy eigenvalue, $E_{n\mathbf{k}}$, $E_{n\mathbf{k}+\mathbf{G}}$ is also the eigenvalue for all vectors **G** of the reciprocal lattice, i.e., the energy eigenvalues are periodic in the reciprocal space.

$$E_n(\mathbf{k}) = E_n(\mathbf{k} + \mathbf{G}) \tag{2.18}$$

With the use of Bloch's theorem, it is sufficient to calculate the electronic part of the total energy only inside the first Brillouin zone to get an electronic structure of the material. Below, we discuss some of the most common methods that have been used to calculate electronic band structure of the TCOs.

2.3.1. Plane Wave Pseudopotential Method. The plane waves are used as a basis set to expand the periodic function $u_{n\mathbf{k}}$:

$$u_{n\mathbf{k}} = \sum_{\mathbf{G}} c_{n\mathbf{k},\mathbf{G}}.e^{i\mathbf{G}.\mathbf{r}} \tag{2.19}$$

Thus, the electronic wave function takes the form

$$\phi_{n\mathbf{k}}(\mathbf{r}) = \sum_{\mathbf{G}} c_{n\mathbf{k},\mathbf{G}}.e^{i(\mathbf{G}+\mathbf{k}).\mathbf{r}} \tag{2.20}$$

i.e., the electronic wavefunctions at each k-point are expressed in terms of a discrete plane wave basis set. To make the problem solvable, one needs to truncate the basis set. One way to restrict the number of the plane waves is to place an upper limit to the kinetic energy of the plane waves, which is called energy cutoff, E_{cut}. Once E_{cut} is set, every plane wave meeting the condition

$$\frac{|\mathbf{k}+\mathbf{G}|^2}{2} < E_{cut} \tag{2.21}$$

is included in the calculation. DFT has reduced the complexity of the problem in electronic structure calculations; however, for systems containing large numbers of electrons, it remains still computationally very expensive. Further, the method of pseudopotentials makes computation feasible because the valance electron mainly determines the physical properties of solids. The pseudopotential method replaces the core electrons and the strong ionic potential with weaker pseudopotential, and that acts on a set of pseudo wave functions. The pseudopotential and the wave functions are both determined in such a way that after cutoff radius, they become indistinguishable to the actual potential and the wave functions (r_c)[100].

2.3.2. All-electron Methods. In this method, instead of separating core-valence electrons all the electrons are explicitly used in the calculation.

2.3.2.1. Augmented plane wave method (APW). The technique of APW uses an approximation for the ionic potential by so-called muffin-tin potential, which is spherically symmetric within some radius (MT) for each lattice site and it is constant outside. APW assumes that the potential is spherically symmetric inside the sphere and flat or slowly varying outside the sphere, the so-called interstitial region (I). The electron potential $V(\mathbf{r})$ in two different regions can be expressed as:

$$V(\mathbf{r}) = \begin{cases} \sum_{lm} V_{lm}(r) Y_{lm}(\hat{\mathbf{r}}) & (r \in MT) \\ \sum_{\mathbf{G}} V_{\mathbf{G}} e^{i\mathbf{G}.\mathbf{r}} & (r \in I) \end{cases} \tag{2.22}$$

The basis set used is:

$$\phi_{\mathbf{k}}n^{APW}(\mathbf{r}, \epsilon_{\mathbf{l}}) = \begin{cases} \sum_{lm} A_{lm,\mathbf{k_n}} u_l(r, \epsilon_l) Y_{lm}(\hat{\mathbf{r}}) & (r \in MT) \\ \frac{1}{\sqrt{V}} e^{i\mathbf{k}_n.\mathbf{r}} & (r \in I) \end{cases} \tag{2.23}$$

where $\mathbf{k_n} = \mathbf{k} + \mathbf{G}_n$; V represents the volume of a unit cell. In this method, energy depends on the functional $u_l(r, \epsilon_l)$ resulting from the non-linear eigenvalue problem.

2.3.3. Linearized Augmented Plane Wave (LAPW) Method. LAPW method solves the non-linearity problem in APW method. The radial wave function $u_l(r, \epsilon_l)$ is expanded using Taylor series. Error in the radial wave function is of second order, and the error in the energy is of fourth order. The LAPW basis set can be defined as:

$$\phi_{\mathbf{k}}n^{APW}(\mathbf{r}, \epsilon_{\mathbf{l}}) = \begin{cases} \sum_{lm} [A_{lm,\mathbf{k_n}} u_l(r, \epsilon_l) + B_{lm,\mathbf{k_n}} \dot{u}_l(r, \epsilon_l)] Y_{lm}(\hat{\mathbf{r}}) & (r \in MT) \\ \frac{1}{\sqrt{V}} e^{i\mathbf{k}_n.\mathbf{r}} & (r \in I) \end{cases} \tag{2.24}$$

The basis set in the interstitial region remained identical to that in the APW method, but in the muffin-tin spheres, it depended on u_l and its energy derivative $\dot{u}_l$. The modified basis function provides the extra flexibility so that it can include a large energy region around linearized energy. The coefficients A_{lm} and B_{lm} are determined from the boundary conditions.

2.3.4. Projector Augmented Wave (PAW) Method. The PAW method combines approaches of LAPW and the pseudopotential method. It was developed by Bloch [122]. This method retains the all-electron character; however, the all-electron (AE) wave function is decomposed in terms of a smooth pseudo-wave function, and a rapidly varying contribution localized within the core region. A linear transformation relates the true and pseudo-wavefunction as:

$$|\psi_n^{AE}\rangle = |\psi_n^{PS}\rangle + \sum_i (|\phi_i^{AE}\rangle - |\phi_i^{PS}\rangle)\langle p_i^{PS}|\psi_n^{PS}\rangle \tag{2.25}$$

The pseudo-wave functions ψ_n^{PS} are expanded in plane waves and are identical to the AE wave functions ψ_n^{AE} in the regions between PAW spheres. Inside the spheres, ψ_n^{PS} are only a rough approximation to the exact wave functions and are only used as a computational tool. In our work, we have used the PAW method as implemented in the VASP code [105, 117].

2.4. OPTICAL PROPERTIES

The frequency-dependent dielectric matrix can be determined from the electronic ground state. The imaginary part, $\varepsilon^{(2)}$, is determined by a summation over empty states using the equation:

$$\varepsilon_{\alpha\beta}^{(2)}(\omega) = \frac{4\pi^2 e^2}{\Omega}\frac{1}{q^2}\lim_{q\to 0}\sum_{c,v,k} 2\omega\delta(\epsilon_{ck} - \epsilon_{vk} - \omega) \times \langle u_{c\mathbf{k}+\mathbf{e}_\beta q}|u_{v\mathbf{k}}\rangle\langle u_{c\mathbf{k}+\mathbf{e}_\beta q}|u_{v\mathbf{k}}\rangle^* \qquad (2.26)$$

where c and v indicate conduction and valence band states, respectively, and $u_{c\mathbf{k}}$ is the cell periodic part of the orbitals at the k-point. The transitions are made from occupied states to unoccupied states within the first Brillouin zone. The real part of the dielectric tensor, $\varepsilon^{(1)}$, is obtained by the usual Kramers-Kronig transformation:

$$\varepsilon_{\alpha\beta}^{(1)}(\omega) = 1 + \frac{2}{\pi}\mathbf{P}\int_0^\infty \frac{\varepsilon_{\alpha\beta}^{(2)}(\omega')\omega'}{\omega'^2 - \omega^2 + i\eta}d\omega', \qquad (2.27)$$

where P denotes the principle value and η denotes the complex shift [123]. The reflectivity can be calculated from complex dielectric function as:

$$R(\omega) = \left|\frac{\sqrt{\varepsilon(\omega)} - 1}{\sqrt{\varepsilon(\omega)} + 1}\right|^2 \qquad (2.28)$$

The expression for energy-loss spectrum, $L(\omega)$, refractive index, n, and extinction coefficient, κ are listed below

$$L(\omega) = \frac{\varepsilon^{(2)}(\omega)}{(\varepsilon^{(1)}(\omega))^2 + (\varepsilon^{(2)}(\omega))^2} \qquad (2.29)$$

$$n = \left[\frac{\sqrt{(\varepsilon^{(1)})^2 + (\varepsilon^{(2)})^2} + \varepsilon^{(1)}}{2} \right]^2 \tag{2.30}$$

$$k = \left[\frac{\sqrt{(\varepsilon^{(1)})^2 + (\varepsilon^{(2)})^2} - \varepsilon^{(1)}}{2} \right]^2 \tag{2.31}$$

2.5. *AB INITIO* MOLECULAR DYNAMICS SIMULATIONS

Meeting the challenge in calculating the full set of many-body forces for a system became possible using *ab initio* molecular dynamics (MD) simulation, as proposed by Car and Parrinello [106]. In *ab initio* MD simulation, inter-atomic forces are derived directly from the ground state by solving density functional equations, Eq. 2.6. The DFT functional for the electronic energy is minimized at every step of MD simulation [124], then the Hellmann-Feynman theorem is used in calculating forces from the ground state energy of the system. The *ab initio* MD does not rely on any adjustable parameter unlike classical MD, but it depends only on the atomic positions, $\mathbf{R_I}$. The *ab initio* MD is summarized in the following steps:

(i) Fix the position of nuclei $\{\mathbf{R}_1, \mathbf{R}_2 \,.....\, , \mathbf{R}_N\}$ to solve Eq. 2.5 self-consistently for the electronic degree of freedom.

(ii) Find the electrostatic force on each atom by using Hellmann-Feynman theorem:

$$\mathbf{F_R} = -\frac{\partial E}{\partial \mathbf{R_I}(t)} \tag{2.32}$$

(iii) Integrate equations of motion for the nuclei over a time step, and find the new positions of the nuclei:

$$M_R \ddot{\mathbf{R}}(t) = \mathbf{F_R}\{\mathbf{R}_1(t), \mathbf{R}_2(t)....., \mathbf{R}_N(t)\} \tag{2.33}$$

In this work, we have used *ab initio* MD as implemented in the VASP code [105] to carry out the simulation of a liquid quench. The following steps are performed to model an

amorphous structure: (i) An initial crystalline structure is heated to several degrees above its melting point to ensure perfect mixing and to remove the memory effect of the crystalline structure. (ii) The initial structures are taken from the equilibrated melt and are subjected to MD simulations involving a stepwise linear cooling protocol with different rates of cooling depending upon the change in the structural features. (iii) The system is fully relaxed towards the energy minimum at the end of the cooling simulation.

The change in structural characteristics during the MD simulation can be seen from the general radial pair distribution function (RDF), $g(r)$, in Fig. 2.1. The RDF is defined

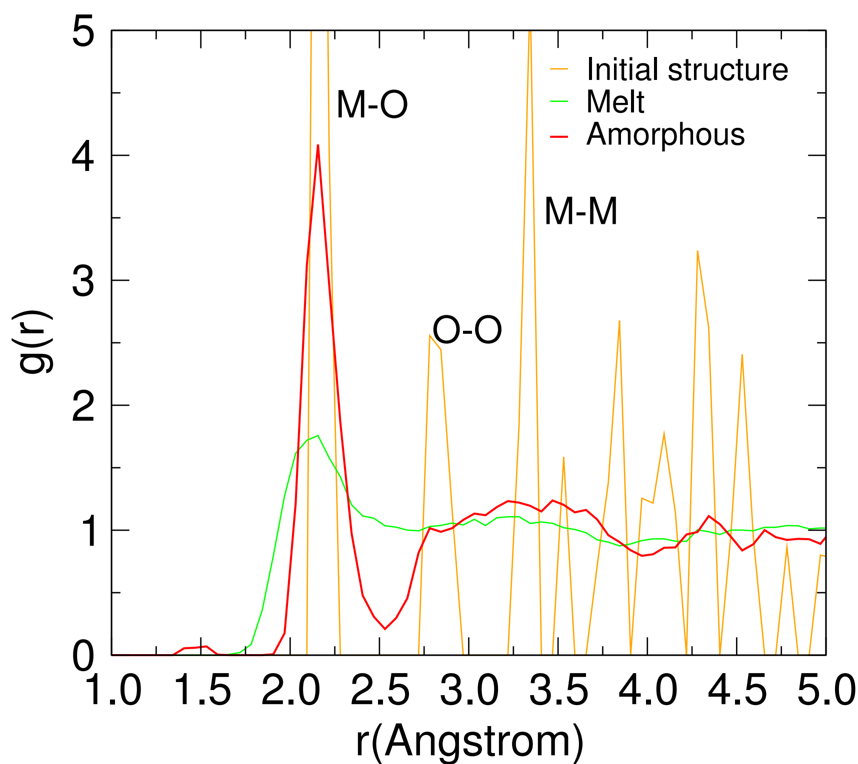

Figure 2.1. Pair distribution function, g(r), of indium oxide showing the three phases, i.e., initial (crystalline), liquid (melt) and amorphous during the liquid quench simulation.

as the probability of finding an atom in a spherical shell with tiny thickness dr at a distance r from a chosen central atom, in other words, this defines the average density of atoms at a distinct position r. In Fig. 2.1, we have shown the radial distribution function for liquid (melt), amorphous, and crystalline materials. Upon melting the initial structure, sharp peaks at definite positions, which characterize crystalline material, will disappear,

and $g(r)$ resembles that of a typical liquid. Once the system is cooled and relaxed at room temperature for the energy minimization, the first peak in the pair distribution function will appear distinctly while other peaks may not be clearly visible, as shown in Fig. 2.1. In total pair distribution shown in Fig 2.1, all peaks are averaged for every atom in the structure. Information obtained from the pair distribution function can be compared to the results obtained from experiment. For a more accurate comparison of the average M-O distances, we have calculated the effective bond distance [125, 126] according to:

$$l_{av} = \frac{\sum_i l_i \, exp\left(1 - \left(\frac{l_i}{l_{min}}\right)^6\right)}{\sum_i exp\left(1 - \left(\frac{l_i}{l_{min}}\right)^6\right)}, \tag{2.34}$$

where the summation runs over all oxygen neighbors of a particular M atom and l_{min} is the shortest M-O distance in the i-th MO_x polyhedron. The average effective bond distance is weighted by taking into account the individual metal-oxygen bond length. It eliminates the long-distance bonds that represent non-interacting M-O pairs. The effective coordination number (ECN) can be calculated based on the obtained effective bond distance (c.f., Eq. 2.34) for every M atom in the cell:

$$\mathrm{ECN} = \sum_i \exp\left(1 - \left(\frac{l_i}{l_{av}}\right)^6\right). \tag{2.35}$$

2.6. MEASURE OF LOCALIZATION IN AMORPHOUS SOLIDS

In the amorphous materials and disordered solids, it is difficult to perfectly describe localized midgap states and band tail states [127]. It is always important and necessary to identify localized states in semiconductors in order to determine the correct location of mobility edges.

There are mainly three ways that are used as the measure of localization [14]. (i) To use information entropy as a measure of localization, the estimate of the number of

accessible atoms, $W(E)$, for a given state is expressed as

$$W(E) = \exp(S(E)) \tag{2.36}$$

where $S(E)$ is the Shannon entropy for N number of atoms, i.e.,

$$S(E) = -\sum_{i=1}^{N} q_i(E)\ln q_i(E). \tag{2.37}$$

This approach uses the fact that is used in information theory – the entropy is a measure of randomness in the Mulliken (point) charge $\{q_i(E)\}$ residing at an atomic site i for an eigenstate with energy eigenvalue E. In this measure $W(E)$ takes the value equal to the total number of atoms for uniformly extended states and unity for an ideally localized state. (ii) To use the spread of the wavefunction in real space, the definition of the spread is used by considering total volume of the cubic supercell volume taking the defect site as a center.

$$\sigma^2 = [\langle \mathbf{r}^2 \rangle - \langle \mathbf{r} \rangle^2] \tag{2.38}$$

The large value of σ^2 corresponds to less localized or the extended states. (iii) A measure of the inverse participation ratio (IPR) is the most commonly used measure. For an orbital, $\psi_n(\vec{r}_i)$ of a system consisting of N atoms, the inverse participation ratio can be expressed as:

$$\mathrm{IPR}(E) = N \frac{\sum_i^N |\psi_n(\mathbf{r}_i)|^4}{|\sum_i^N |\psi_n(\mathbf{r}_i)|^2|^2} \tag{2.39}$$

The IPR is large for highly localized states and small for extended states. In our study, we have used IPR as a measure of localization of the states.

2.7. DISSERTATION OUTLINE

This dissertation is organized as follows. Motivation and status of the transparent conducting oxides and amorphous transparent conducting oxides have been discussed in Section 1. Section 2 contains background and description of the methods employed in the calculations. The main body of the dissertation contains four papers. Summaries of each of those paper are presented below.

Paper I: In this paper, we started our study by comparing interatomic distances and coordination numbers for the first shell (Metal-Oxygen bond) and the second shell (Metal-Metal bond) to the experimental results for the structures with the different degree of amorphization. The latter is obtained experimentally via different deposition temperatures and theoretically via different cooling rates. Based on the excellent agreement between EXAFS experimental results and our MD simulated results, we were able to study the structural feature for the third coordination shell (corner-shared In-In). Interestingly, we have shown that a long chain of InO_6 connected primarily via corner sharing is responsible for the enhancement in the carrier Hall mobility at the onset of the amorphous region. The percent contribution of corner-shared InO_6-InO_6 polyhedra to the total (edge and corner) shared InO_6 pairs are shown in Fig. 2.2, where the maximum in the observed mobility coincides with the maximum in the calculated number of the corner-shared InO_6 pairs. This finding highlights the importance of the medium/long-range structural characteristics in amorphous oxides.

Paper II: In this paper, we have investigated ternary In-based oxides, In-X-O with X=Sn, Zn, Ga, Cd, Ge, Sc, Y or La to determine their short range and medium/long range structural characteristics. Our investigation showed that the local features, i.e., the In-O coordination and bond distance, depend weakly on the presence of cation X in the system. However, the structural characteristics of the metal-metal shell, namely, the M-M distance and M-O-M angles which determine how MO polyhedra are integrated into a network,

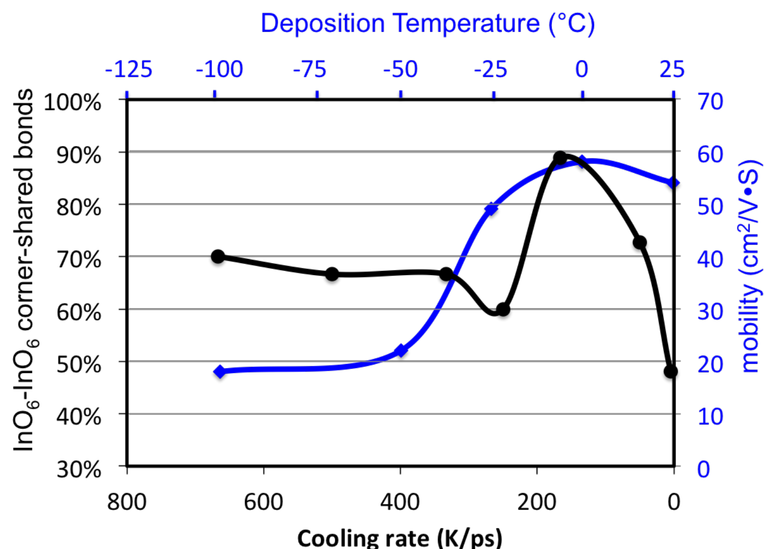

Figure 2.2. Percent contribution corner-shared InO_6-InO_6 polyhedra to the total (edge and corner) shared InO_6 pairs as a function of cooling rate (black): Low-temperature region of Hall mobility versus deposition temperature curve as given in Ref.[147].

are affected by the presence of X, which will play the key role in charge transport in the amorphous oxide. In particular, we found that while IZO and IGO have the same number of six-coordinated In atoms, Zn favors edge sharing between InO_6 polyhedra (ZnO polyhedra prefer corner-sharing) whereas as Ga favors their corner-sharing (GaO polyhedra prefers edge-sharing with its neighboring polyhedra). The presence of Sn leads to the formation of short-distant edge-shared InO_6 pairs resulting to the smallest average distance between the connected InO_6 pairs. The sharing between the MO polyhedra will affect the degree of amorphization of the materials and also the carrier mobility controlled by scattering on large XO clusters or nanocrystalline inclusions (In_2O_3).

Paper III: Here we have studied the nature of the charge transport and local structure in the amorphous oxide In-X-O with X=Sc, Y or La. Both experimental and theoretical study are combined to understand the role of cation size by taking three cations of the same valence but different ionic radii (0.89Å for Sc, 1.04Å for Y, and 1.17Å for La) in the structural and transport properties. In agreement with experimental observations, we

have found that the larger cations such as La are effective in producing amorphous state by reducing the relative number of fully coordinated In,i.e., InO_6, in comparison to Sc or Y.

Paper IV: The local bonding and the metal-O polyhedra are studied in detail in amorphous In-X-O with X= Sn, Zn, Ga, or Ge to understand the observed carrier concentration and the carrier Hall mobility behavior. Based on our simulation results, we have shown that an interplay between the local and long-range structural preferences of the constituent oxides give rise to a complex composition-dependent behavior in these multicomponent materials. The carrier concentration was found to correlate with the weak dependence of the local structural properties on the different cations. This finding suggests that different cations do not govern the carrier generation directly. At the same time, composition-induced differences in the connectivity and spatial distribution of InO_6 and XO_x polyhedra are found to determine the formation of the amorphous structures and to explain the observed carrier mobility.

PAPER

I. THE STRUCTURE AND PROPERTIES OF AMORPHOUS INDIUM OXIDE

D. Bruce Buchholz[†], Qing Ma[‡], Diego Alducin[◊], Arturo Ponce[◊], Miguel Jose-Yacaman[◊], Rabi Khanal [♯], Julia E. Medvedeva [♯], and Robert P. H. Chang[†]

[†]*Department of Materials Science and Engineering, Northwestern University, Evanston, IL 60208*

[‡] *DND-CAT, Northwestern Synchrotron Research Center at the Advanced Photon Source, Argonne National Laboratory, Argonne, IL 60439*

[◊]*Department of Physics and Astronomy, University of Texas at San Antonio, San Antonio, TX 78249*

[♯]*Department of Physics, Missouri University of Science & Technology, Rolla, MO 65409-0640*

ABSTRACT[*]

A series of In_2O_3 thin films, ranging from X-ray diffraction amorphous to highly crystalline, were grown on amorphous silica substrates using pulsed laser deposition by varying the film growth temperature. The amorphous-to-crystalline transition and the structure of amorphous In_2O_3 were investigated by grazing angle X-ray diffraction (GIXRD),

[*]Published in Chemistry of Materials **26**, 5401-5411 (2014).

Hall transport measurement, high resolution transmission electron microscopy (HRTEM), electron diffraction, extended X-ray absorption fine structure (EXAFS) and *ab initio* molecular dynamics (MD) liquid-quench simulation. On the basis of excellent agreement between the EXAFS and MD results, a model of the amorphous oxide structure as a network of InO_x polyhedra was constructed. Mechanisms for the transport properties observed in the crystalline, amorphous-to-crystalline, and amorphous deposition regions are presented, highlighting a unique structure-property relationship.

1. INTRODUCTION

Fundamental understanding of the chemical and structural origins of transparent conducting oxides (TCOs) has allowed TCOs to evolve into important materials for photovoltaic devices and optoelectronic applications [5, 21, 39, 128]. Transparent oxide semiconductors (TOSs), are currently being explored as thin film transistor (TFT) materials, as an enabling technology for the next generation of computing, communication and identification devices [30, 128]. Initially, the technological application of TCOs and TOSs employed these materials in their crystalline form. There is, however, an increasing shift towards the use of these materials in their amorphous form. In 2010, an estimated 30-40% of all flat panel displays employed an amorphous TCO material [58].

Amorphous TCOs and TOSs (*a*-TCOs and *a*-TOSs) have several advantages over their crystalline counterparts. In general, amorphous materials are deposited at lower temperatures [129] which tend to simplify the deposition process and expand the number of substrates the material can be deposited on, such as plastics. Amorphous materials, lack grain boundaries and are isotropic and, hence, tend to etch more uniformly, [42, 61, 62] have lower surface roughness, [63, 64] and can be deposited uniformly over large areas [42, 59]. Some amorphous materials can also be less prone to fracture, hence being more pliable, lending themselves to the possibility of flexible electronics [42, 130]. These advantages are realized without a significant loss to the seminal properties of conductivity and transparency, for optimized materials [32].

The electrical and optical properties of crystalline TCOs and TOSs (*c*-TCOs and c-TOSs) are strongly influenced by the oxygen content of the film [131]; the same is true for *a*-TCOs and *a*-TOSs [132]. For *c*-TCOs and *c*-TOSs, their properties are also affected by factors related to the crystal structure such as grain size [133] and crystallographic direction [134]. By understanding how structure affects properties, it has been possible to improve the performance of *c*-TCOs and *c*-TOSs. An understanding of the structure in *a*-TCOs and

a-TOSs would afford the same opportunity for materials optimization. There is, however, a much smaller knowledge base as to the structure of *a*-TCOs and *a*-TOSs than for their crystalline counterparts.

The basic structure for TCOs and TOSs is a network of MO_x polyhedra. Each metal ion is coordinated with some number of oxygen ions, known as the M-O coordination number (N_{M-O}), at some bond distance or distances, known as the M-O bond-distance (R_{M-O}), to form polyhedra. The polyhedra are then linked together either at their corners, sharing one oxygen between two polyhedra (corner-sharing polyhedra); at their edges, sharing two oxygen between two polyhedra (edge-sharing polyhedra); or, much less common, along their faces, sharing three or more oxygen between polyhedra (face-sharing polyhedra), see Figure 1. The linking of polyhedra results in the formation of a network where, ignoring the interposing oxygen for the moment, each metal ion is coordinated with some number of other metal ions, the M-M′ coordination number ($N_{M-M'}$), at some distance or distances, the M-M′ distance ($R_{M-M'}$). Here M and M′ are used since in multication materials a specific cation can be coordinated with a multiplicity of other cation species. The fact that there is an interposing oxygen between cations leads to the concept of a M-O-M′ bond angle. In discussing the structure of a TCO or TOS, one looks at both the polyhedra structure (N_{M-O} and R_{M-O}) and the network formed by the linked polyhedra ($N_{M-M'}$, $R_{M-M'}$ and the M-O-M′ bond angle). It is the distortions in the MO_x polyhedra and integration of the polyhedra into a continuous network that ultimately govern the properties of the oxides.

The crystalline structure for many of the indium oxide based TCOs and TOSs is that of indium oxide, In_2O_3 (IO), bixbyite structure (space group I*a*3, number 206). Bixbyite is a fluorite-type structure with one-quarter of the anions missing; a periodic structure that produces “structural vacancies". In the crystalline structure, the oxygen atoms are octahedrally coordinated around indium; all indium cations are surrounded by six oxygen atoms (c-N_{In-O} = 6) and two “structural vacancies". This is also known as the first-shell around indium. The structural vacancy positions can sit along the body diagonal (*b*-site)

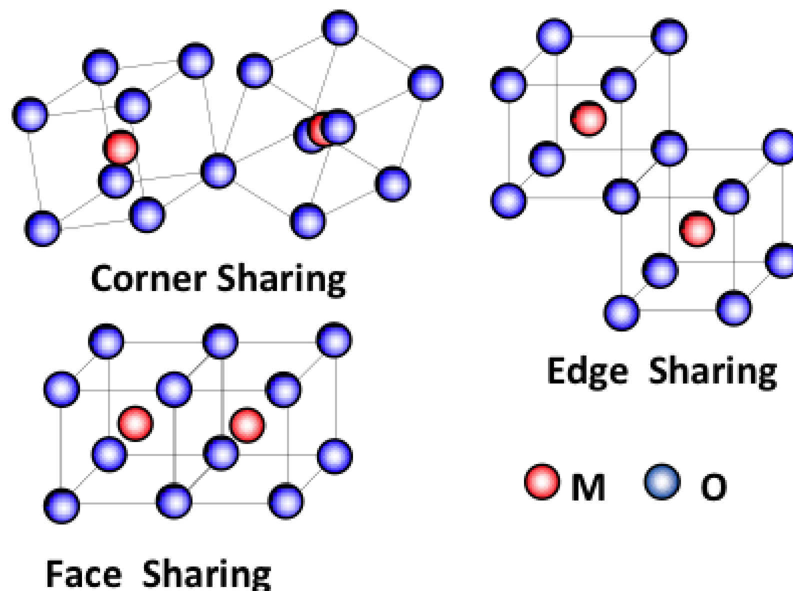

Figure 1. Corner, edge and face sharing polyhedra

or along a face diagonal (d-site), Figure 2. The b-site represents 25% of the octahedra arrangement and the d-site 75% of the octahedra arrangement. In the b-site arrangement all the oxygen are equidistant from the indium at 2.18 Å. In the d-site arrangement there are two oxygens at each distances 2.13, 2.19 and 2.23 Å. The average In-O bond distance for all arrangements in the theoretical structure is 2.18 Å ($c - R_{In-O}$ = 2.18 Å). The existence of structural vacancies gives rise to two configurations by which InO_6 octahedra link together in crystalline In_2O_3: In the first, both an oxygen and a structural vacancy are shared between adjacent polyhedra with the end result that the polyhedral are only joined at a corner, hence “corner sharing"; in the second two oxygen are shared between the adjacent polyhedra with the end result that the polyhedral are joined along the entire edge, “edge sharing", Figure 2. This leads to two distinct sets of adjacent polyhedra In-In neighbors: There are six-adjacent edge-sharing polyhedra, N_{In-In} = 6, at a distance of ~3.34 Å, R_{In-In} = 3.34 Å, and six-adjacent corner-sharing polyhedra, N_{In-In^*} = 6, at a distance of ~3.83 Å, R_{In-In^*} = 3.83 Å. These make up the second and third shells around indium, respectively, the first shell being the InO_6 octahedra. A common method of probing the structure of these

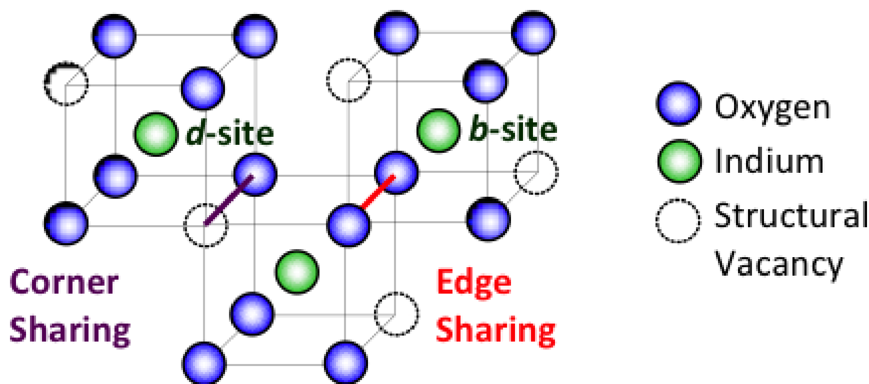

Figure 2. Structure of crystalline In_2O_3 (bixbyite)

materials is extended X-ray absorption fine structure (EXAFS) [104]. Fourier transform analysis of the EXAFS data yields structural information in the vicinity of each kind of atom whose absorption is probed. This information can include M-O and M-M′ coordination numbers (N) and bond distances (R) as well as the statistical spread of bond distances (σ^2) due to thermal motion and/or static disorder; this last factor is of particular interest in amorphous materials [135]. As mentioned, in materials built up of MO_x polyhedra, the M-O structure is often referred to as the first shell and the nearest M-M′ structure as the second shell. In the first shell there are no multiple scattering effects and the interpretation of data is fairly straightforward even in multiple cation systems. Interpretation for data in the second shell where multiple scattering effects can occur is complex, particularly in multiple cation systems. The interpretation of the second shell becomes more complex in amorphous systems where the second shell is less well ordered; the third shell is even harder to interpret.

Several EXAFS studies have been done on the structure of In, Ga, Sn and Zn containing *a*-TCOs and *a*-TOSs. These studies are summarized in the Ref. [136]. All but one deal exclusively with the first shell, that is the coordination of oxygen around the metal cations. Similarly, available theoretical models of amorphous oxides derived from molecular dynamics simulations focus primarily on the first shell M-O results with no or

limited information on the M-M distances and coordination [47, 49, 50, 68, 81, 84, 137, 138, 139]. The coordination of oxygen around indium is frequently compared to that of crystalline indium oxide (bixbyite); c-N_{In-O} of 6 and $c-R_{In-O}$ of 2.18 Å. With the exception of the studies by D-Y. Cho, et al., there is general agreement that in the amorphous materials R_{In-O} is contracted relative to that found in the crystalline material. There is, however, little agreement in N_{In-O} which ranges from a low of 4.5 to a high of 6.1. Differences in the chemical environments for the different materials might contribute to the large spread of values for N_{In-O}, however, even for compositionally equivalent materials, such as $InGaZnO_4$ where N_{In-O} ranges from a 4.5 to 5.8 and $Zn_{0.3}In_{1.4}Sn_{0.3}O_7$ where N_{In-O} ranges from 5 to 6 (albeit set), there is little agreement. Although these differences may be due, in part, to differences in processing methods, the complexities encountered when modeling multi-cation systems make it possible to obtain different results from the same data depending on the simplifying assumptions and modeling parameters used. These difficulties in data interpretation are greatly compounded for the second shell where multiscattering effects and the suppression of the Fourier transform at the higher R-range require additional simplifying assumption.

Although pure indium oxide (IO) is rarely used in technological applications it is the progenitor of many TCO and TOS systems. In structural studies like these, IO has the advantage over more complex systems in that fewer constraints and assumptions need to be imposed when modeling the data. For this study, a series of IO films, 350 nm thick, were grown by pulsed laser deposition (PLD) at temperatures ranging from -100 to 600 °C in order to determine variations in the structural characteristics and to relate those to the optimum properties. X-ray absorption spectroscopy and EXAFS analysis was performed on these samples to determine the indium-oxygen coordination number (N_{In-O}) and the average indium-oxygen bond distance (R_{In-O}), as well as the statistical spread of the bond distance (σ^2_{In-O}). Additionally the next-nearest neighbor indium-indium coordination

number (N_{In-In}) and the bond distance (R_{In-In}), as well as the statistical spread of the bond distance (σ^2_{In-In}), were determined.

A powerful model for the construction of a plausible structure of an amorphous material is molecular dynamics (MD) liquid-quench simulations. In a liquid-quench simulation a crystalline structure is heated to several thousand degrees for mixing. The equilibrium melt is then cooled rapidly (quenched) in a stepwise fashion to a final temperature; different total quench times are realized by changing the quench rate. In some simulations the cooled structure is allowed to relax at constant volume to an energy-minimized quenched structure. PLD is a physical analogue to a liquid-quench simulation. In PLD a crystalline target is heated to several thousand degrees by a laser pulse. The plasma plume is rapidly cooled to a solid structure at the substrate. The structure then relaxes, to some extent, to a local energy minimum. The results of these experiments, therefore, readily lend themselves to interpretation by MD liquid-quench simulations. In this work, first-principles density-functional-based molecular dynamics is employed to obtain *a*-IO structures at different quench rates in order to understand their effect on the structural properties of *a*-IO and to explain the experimentally observed trends in PLD-grown samples. With the aid of MD simulations, it was possible not only to corroborate the first and second shell results by EXAFS, but also to extract additional information for the third-shell structure of *a*-IO.

2. EXPERIMENTAL SECTION

IO thin-films, ~350 nm thick, were grown by PLD from a dense hot-pressed indium oxide target (25 mm diameter). PLD was accomplished with a 248 nm KrF excimer laser with a 25 ns pulse duration and operated at 2 Hz. The 200 mJ/pulse beam was focused onto a 1 mm × 2 mm spot size. The target was rotated at 5-rpm about its axis to prevent localized heating. The target-substrate separation was fixed at 10 cm. The films were grown on fused-silica substrates in an O_2 ambient of 8 mTorr. The substrates were attached to the

substrate holder with silver paint. For films grown above room temperature a resistively heated substrate-holder was used; for films grown below room temperature a liquid nitrogen cooled substrate holder was used.

Sheet resistance (Rs: Ω/□), carrier type, area carrier-concentration (na: $1/cm^2$), and carrier mobility (μH: $cm^2/V.s$) were measured with a Ecopia 3000 Hall measurement system on samples in the van der Pauw geometry. Carrier density (nv: $1/cm^3$) and resistivity (ρ: Ω.cm) were calculated by dividing the area carrier-concentration and sheet resistance, respectively, by the film thickness. Film thickness (d: nm) was measured using a spectral reflectometer (Filmetrics F20). Grazing incidence X-ray diffraction (GIXRD) was performed using an 18 kW Rigaku ATX-G diffractometer. CuKα radiation (λ = 1.54 Å) was conditioned by a parabolic multilayer mirror and collimated to produce a 0.1 mm (vertical) by 5 mm (horizontal) beam with incident flux of $\sim 2\times10^8$ photons/s; a beam incident angle of 0.46^o was used. Film composition was measured by X-ray Photoelectron Spectroscopy (XPS) using a Thermo Scientific ESCALAB 250Xi using a Al K α source and a take-off angle of 90°. An argon ion source was used to clean carbon from the surface prior to analysis. The flood gun was used on all analysis although it was only needed on the more insulating samples to maintain charge neutrality.

X-ray absorption spectroscopy (XAS) was performed at the 5-BMD beamline of DND-CAT at the Advanced Photon Source (APS) of Argonne National Laboratory (Argonne, IL). The In-Kα, fluorescence emissions from the indium oxide thin films was measured using a four-element Si-drifted detector (SII) with the incident X-ray angle θ at about 45° with respect to the sample surface. The XAS data was analyzed with the ATHENA software packages [140]. The data were Fourier transformed with a Hanning window over multiple k ranges where one-shell and three-shell fits were examined; see the Ref. [136] for a detailed analysis of the rationale behind the choice of fit parameters. The k-range of the EXAFS data used in the analyses was k = 2.24 - 12.67 Å^{-1} with a k-weight of 2. Fitting carried out in R space was from R = 1.0 to 2.0 Å for the one-shell model and R

= 1.0 to 4.0 Å for the three-shell model. Paths for the first (In-O), second (In-In) and third (In-In*) were used in the three-shell model; only the first shell was used in the one-shell model.

For transmission electron microscopy (TEM), the indium oxide films were mechanically cleaved from the substrate and deposited onto a holey carbon grid. The samples were studied using a Jeol ARM 200F microscope operated at 200 keV. In order to prevent crystallization by the electron beam, the samples were examined under low electron-dose illumination using the smallest condenser lens aperture (10 μm), In this way, the same illumination conditions were used for selected area electron diffraction (SAED) patterns were taken with a beam current ranging between 5 to 15 pA/cm^2 and patterns were collected at exposure times of 10 to 20 s.

3. THEORETICAL

The amorphous In-O structures were generated using first-principles molecular dynamics as implemented in the Vienna Ab Initio Simulation package [105, 116, 117, 118]. These calculations are based on the density functional theory (DFT) within generalized gradient approximation (GGA) with PBE functional [114]. For initial structure, bixbyite In_2O_3 supercells containing 80, 130 or 180 atoms and with density 7.12 gm/cm^3 were used. To remove the memory of the atomic arrangement, the initial structure was melted at 3000K for 6 ps. Next, the melt was cooled to 2200K-1700K at the rate of 100K/1.2 ps, and then rapidly quenched to 100K using different quench rates ranging from 700K/ps to 5K/ps. In order to make these challenging calculations computationally efficient, a low cut-off of 260 eV was used and k-point sampling was restricted to Γ point only. The final structures were equilibrated at 300K for 6 ps with cut-off of 400 eV. All simulations were carried out within NVT ensemble with Nosé-Hoover thermostat using integration time step of 2 fs. For the amorphous structures with different supercell sizes, we analyzed the pair distribution

functions and found that 80-atom supercell is sufficient to describe the amorphous character, as found in previous theoretical calculations [81].

We note here that a typical cooling rate employed in *ab initio* MD simulations of amorphous oxides is 200K-100K/ps; slower cooling rates in DFT-based MD require significant computational efforts and were not previously reported for amorphous oxide semiconductors (in contrast to classical MD simulations). These quench rates were shown to produce reliable amorphous structures [47, 81, 91, 141, 142]. Indeed, simple estimations based on the thermal conductivity, heat capacity, and density of In_2O_3 suggest that a time of 10^{-12} to 10^{-13} s is required to cool a 1nm thick oxide by 1K. In this work, cooling rates ranging from ~700K/ps to 5K/ps are employed to compare the MD simulation results to the experimentally observed dependence of the structural properties on the PLD deposition temperature. The agreement between EXAFS and MD results helps explain the intriguing behavior of mobility near the crystalline-amorphous transition. Additionally, the results of the MD simulations are used to apply reasonable constraints on the EXAFS analysis of the second and third shells.

4. RESULTS AND DISCUSSION

For many thin-film material systems, the transition between amorphous and crystalline can be accomplished by changing the temperature of deposition; the crystalline phase being favored by higher deposition temperatures. Such is the case for IO deposited on fused quartz by PLD. Figure 3 is the GIXRD patterns of IO films ~350 nm thick. Films grown at temperatures of 0 °C and below are all X-ray diffraction amorphous (*a*-IO). The first sign of crystallinity is observed at +25 °C. The GIXRD spectra for the crystalline films (*c*-IO) are typical of that observed for polycrystalline bixbyite In_2O_3.

The films deposited at 0 °C and below have been referred to as “X-ray diffraction amorphous" rather than simply amorphous because they can still contain nanocrystalline

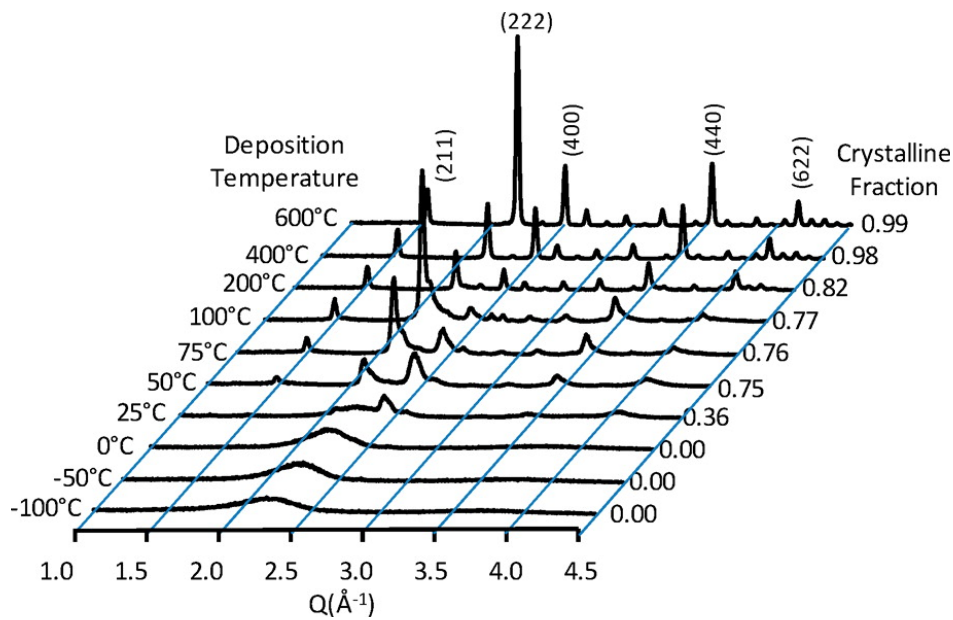

Figure 3. GIXRD patterns of indium oxide films, ~350 nm thick, as a function of deposition temperature. The *c*-IO/*a*-IO ratio, is determined by the area of the crystalline XRD peaks to the combined areas of the crystalline XRD peaks and the “amorphous hump".

inclusions. At deposition temperatures as low as -50 °C nanocrystalline inclusions, 1.9 to 2.4 nm in size, can be found in a dominant amorphous phase as seen in the HRTEM image of Figure 4a; the SAED inset confirms the presence of a dominate amorphous phase. As the deposition temperature is increased to 0 °C, the size of the nanocrystalline inclusions increases to between 2.2 to 3.4 nm; the amorphous phase is still dominate, Figure 4b. At a deposition temperature of +100 °C, where crystallinity is clearly visible by X-ray diffraction, the crystals are quite large and more dominate as evidenced in Figure 4c where the inset SAED pattern has begun to form diffraction reflections which are closer in appearance to a highly crystalline sample, Figure 4d, than the amorphous samples, Figures 4a and b. Although nanocrystalline inclusions exist in the diffraction amorphous films, to simplify notation, for the remainder of the paper the diffraction amorphous films will simply be referred to as amorphous and the advent of crystallinity to occur at +25 °C where it is first observable by X-ray diffraction.

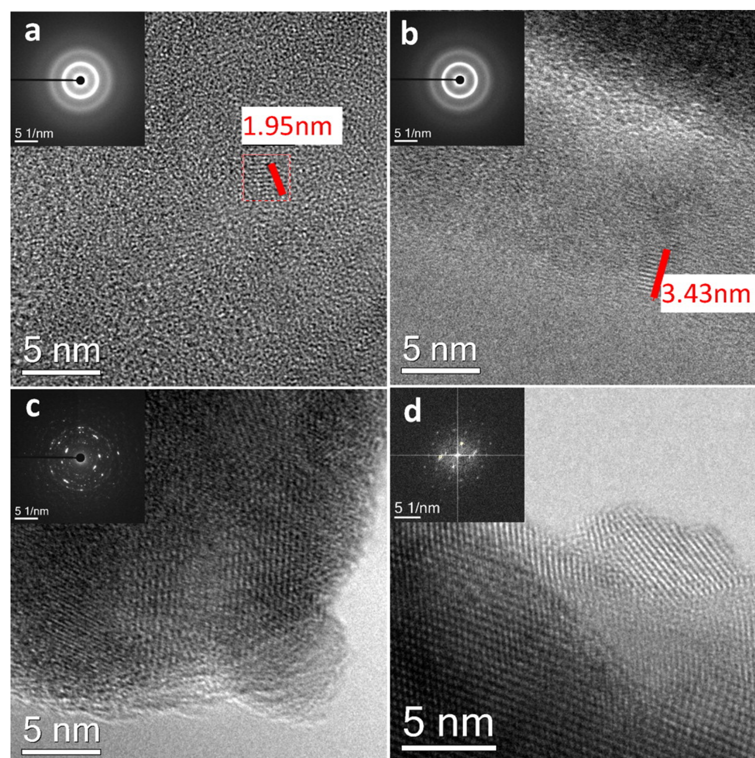

Figure 4. HRTEM images of indium oxide films deposited at a) -50 °C, b) 0 °C, c) +100 °C and d) +600 °C. Insets are representative SAED patterns from the respective films.

One of the main objectives for the study of structure is to optimize properties; for TCOs and TOSs one property of major interest is carrier mobility (μH). Figure 5 shows the Hall carrier mobility of the 350 nm films as a function of growth temperature. In the high temperature *c*-IO region (+400 to +600°C), μH is high (60-70 cm^2/V.S), typical of highly crystalline (albeit polycrystalline) films. The value of μH is again quite high (~60 cm^2/V.s) right at the advent of crystallinity (0°C to +25°C); the possible origins of this high mobility will be explored in the EXAFS analysis and MD simulations sections. The mobility decreases between -25°C to -100°C and reasons for this will also be explored in the EXAFS analysis and MD simulations sections. The region between the *a*-IO and *c*-IO films has a decrease in mobility from that observed for both the films deposited in the high temperature crystalline region (≥400°C) and the films deposited right at the advent of crystallinity (0°C to 25°C). This region contains both crystalline and amorphous material

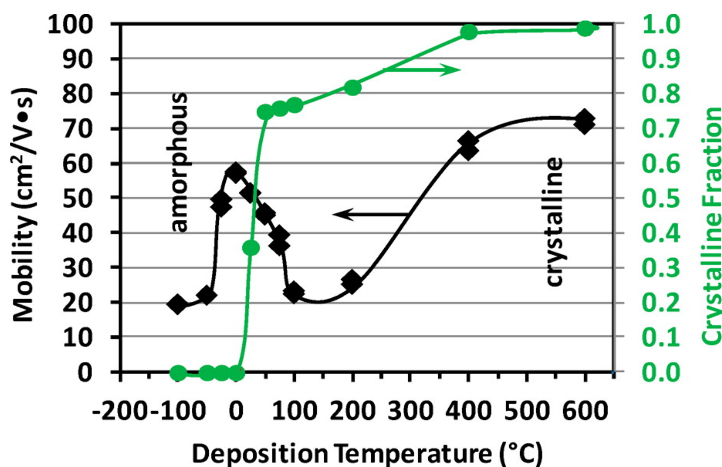

Figure 5. Hall mobility of indium oxide films, ~350 nm thick, as a function of deposition temperature.

in sufficient quantities to be detectable by X-ray diffraction; incoherent boundaries between the crystalline and amorphous phases can serve as scattering centers. As the first crystallites form in a majority amorphous phase they act as scattering centers that lower the mobility; further increase in deposition temperature increases the number of crystalline scattering centers attended by further decrease in mobility until the crystalline phase becomes the major percolation path through the material. At this point the amorphous regions become the *de facto* scattering centers. Further increase in temperature decrease the amorphous fraction thereby decreasing the number of scattering centers and increasing mobility.

XAS and EXAFS analysis was performed on the same samples to gain greater insight into the differences in film structure. The In-O coordination numbers are shown in Figure 6a. The highly crystalline samples have six-fold oxygen-coordination around indium (c-N_{In-O} ~ 6) consistent with the bixbyite structure. The fully amorphous films have significantly lower oxygen-coordination around indium (a-N_{In-O} ~ 5.3). Two possible reasons for the lower oxygen-coordination are a difference in stoichiometry or a change in structure. XPS was used to compare the composition of a similar set of thinner (65 nm) films deposited over the same temperature range (-100 to 600°C); all the films had the same

In/O ratio within ±5% with no observable trend with respect to deposition temperature. Hence, a change in structure is the more plausible explanation for the change in N_{In-O}.

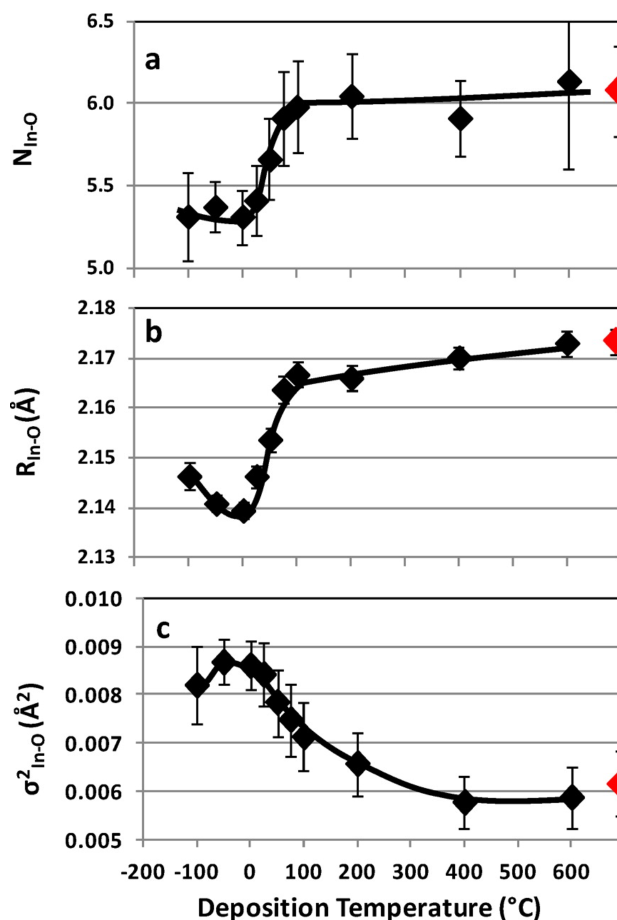

Figure 6. a) In-O coordination number, N_{In-O}, b) In-O bond-distance, R_{In-O} and c) σ^2_{In-O} for the In-O shell of indium oxide films, ~350 nm thick, as a function of deposition temperature: Red markers, powdered In_2O_3 standard.

The In-O bond distance for the highly crystalline samples is, on the average, ~2.17 Å (R_{In-O} =2.17 Å), Figure 6b, just slightly less than the ideal structural distance of 2.18 Å. There is a further contraction in the average In-O bond distance in the amorphous films. This is consistent with a reduced coordination number observed in the amorphous films; lower oxygen-coordination also allows a reduction in In-O distance while maintaining O-O separation. The minima at 0°C, ~2.14 Å, is interesting in that it also corresponds to the highest temperature at which an amorphous film can be grown and the point of highest carrier mobility. However, because of the relatively small variation in R_{In-O} for the

amorphous samples additional measurements would be needed to confirm a minimum. The statistical spread of bond distances (σ^2_{In-O}) due to thermal motion and/or static disorder ranges from a low of ~0.0054 Å^2 to a high of ~0.0085 Å^2, Figure 6c. As might be expected, the lowest σ^2_{In-O} corresponds to the highly crystalline films deposited at 400°C and 600°C, and the highest σ^2_{In-O} to the amorphous films.

To achieve an amorphous structure the regularity of the crystalline structure, Figure 7a, must be perturbed, usually in bond distance and/or bond angle. If, for the moment,

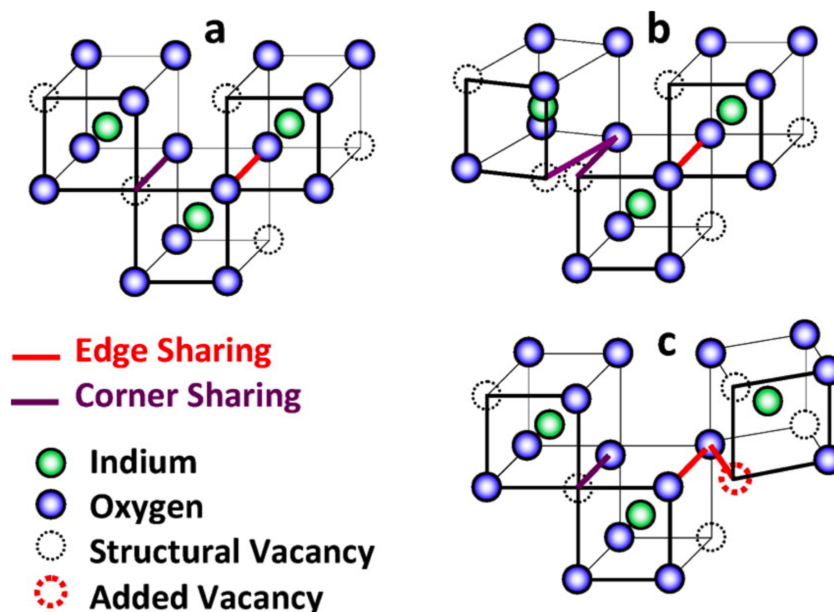

Figure 7. a) unperturbed lattice; b) rotation of corner sharing polyhedra; c) rotation of edge sharing polyhedra

the polyhedra are assumed relatively undistorted, the structure can still become amorphous by virtue of distortions in the way the polyhedra are linked. Consider what happens when the In-O-In bond angle is changed by the rotation of the polyhedra edges about an oxygen. If the rotation occurs between corner-sharing polyhedra, Figure 7b, the net effect is to change the In-In bond distance as well as the In-O-In bond angle. If the rotation occurs between edge-sharing polyhedra, Figure 7c, the net effect is not only to change the In-O-In bond angle and In-In bond distance but to also require the introduction of an additional structural vacancy thus lowering the In-O coordination number by an average of 1/2 for the

two polyhedra involved, Figure 7c; the polyhedra will also change from being edge-sharing to corner-sharing. A second way the In-O coordination number could be lowered is by rotating the polyhedra along an edge thereby disjoining adjacent polyhedra; the separation of corner-sharing polyhedra would result in lowering the In-O coordination number by an average of 1/2 for the two polyhedra involved, Figure 8b, and the separation of edge-sharing poly-hedra would result in lowering the In-O coordination number by an average of 1 for the two polyhedra involved, Figure 8c. The caricatures of the rotations in Figures 7 and 8 are greatly simplified. In the crystalline solid the polyhedra are linked over large volumes; when a polyhedra is rotated the bonds with all adjacent polyhedra are perturbed which are, in turn, displaced within the lattice network. The net effect, if stoichiometry is maintained, is to reduce N_{In-O}.

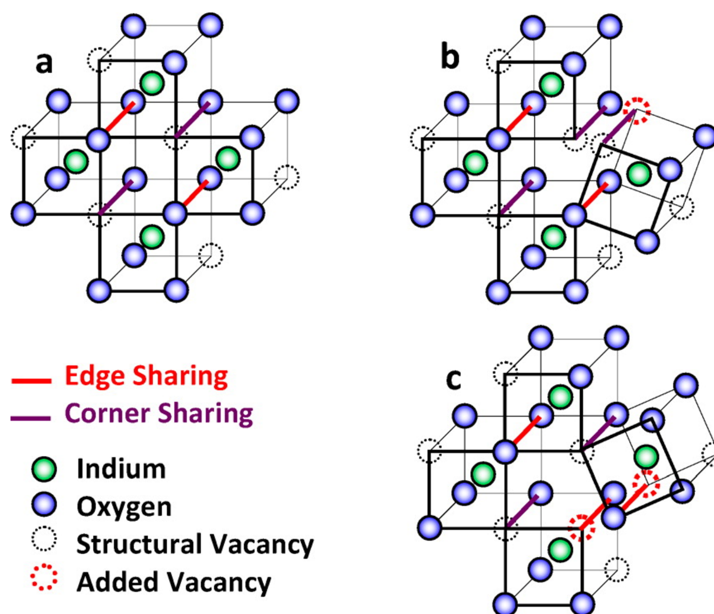

Figure 8. a) unperturbed lattice; b) breaking of corner sharing bond; c) breaking of edge sharing bond.

For c-IO, the second shell is made up of the six-adjacent edge-sharing polyhedra, N_{In-In} = 6, at a distance of R_{In-In} ~3.34 Å. The highly-crystalline samples, 400°C and 600°C, have six-fold nearest-neighbor indium-indium coordination (c-N_{In-In} ~ 6) consistent with the number of edge-sharing nearest-neighbor polyhedra in the bulk bixbyite

structure. The fully amorphous films have significantly lower nearest-neighbor indium-indium coordination (a-$N_{In-In} \sim 2$), Figure 9a. For the highly crystalline films, the nearest-neighbor indium-indium distance is, on the average, 3.36 Å (c-$R_{In-In} \sim 3.36$ Å); slightly larger than the value for the ideal bixbyite structure. This decreases to a minimum of 3.29 Å for the fully amorphous sample grown at 0°C (a-$R_{In-In} \sim 3.31$ Å), Figure 9b. Again, the minimum bond distance is observed at the point of highest mobility. The statistical spread of In-In bond distances (σ^2_{In-In}) due to thermal motion and/or static disorder ranges from a low of ~0.004 Å^2 to a high of ~0.014 Å^2, Figure 9c. As might be expected, the lowest statistical spread corresponds to the highly crystalline films deposited at 400 and 600°C; the highest statistical spread to the amorphous samples.

The decrease in N_{In-In} is consistent with the mechanism proposed for the decrease in N_{In-O}. The rotation pictured in Figure 7c would convert two edge-shared second-shell polyhedra into two corner-shared third-shell polyhedra while increasing the number of structural oxygen vacancies by only one. A similar effect has been observed in quartz where crystalline quartz was observed to have c-$N_{Si-O} \sim 4.0$ and c-$N_{Si-Si} \sim 4.0$ while fused silica was observed to have a-$N_{Si-O} \sim 3.7$ and a-$N_{Si-Si} \sim 1.1$ [143]. The rotation in the In-O-In bond angle can also account for the decrease in R_{In-In}. The second shell bond distance, R_{In-In}, is more or less a maximum in the crystalline structure, therefore, R_{In-In} would be expected to decrease in the amorphous phase and be attended by an increase in σ^2_{In-In}. A decrease in R_{In-In} increases the In-In bond orbital overlap which would contribute to higher mobility. The decrease in mobility with a further decrease in deposition temperature from 0°C is attended by an increase in R_{In-In}. Here we believe the lattice is frozen in a less relaxed state before polyhedra can rotate into closer proximity. X-ray reflectivity studies on thinner films (60 nm thick) indicate as the deposition temperature is lowered below the point at which the films become X-ray diffraction amorphous the density of the films decrease [144]; this would be consistent with a more open structure being frozen in place.

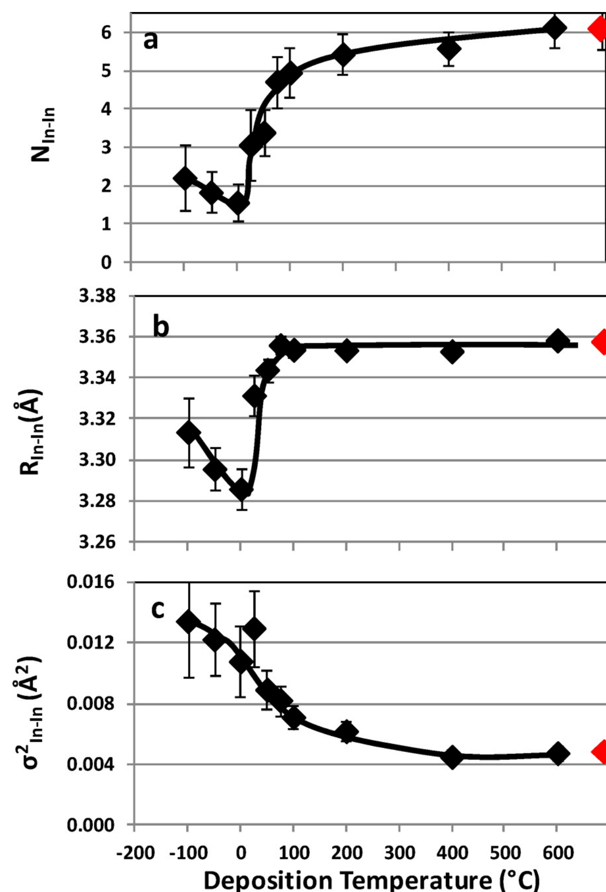

Figure 9. a) In-In coordination number, N_{In-In}, b) In-In bond-distance, R_{In-In} and c) σ^2 for the In-In shell, σ^2_{In-In}, of indium oxide films, ~350 nm thick, as a function of deposition temperature: Red markers-powdered In_2O_3 standard.

The analysis of the third shell, the structure of the corner shared polyhedra, is more difficult to determine; even for the highly crystalline samples the calculated third-shell coordination number is ~5 (c-$N_{In-In^*} \approx 5$), see the Ref. [136]. There is, however, a *piori* knowledge that this value should be ~ 6 because of the highly crystalline nature of the samples. When the value of N_{In-In^*} is constrained in the model to 6, the computed value for the third-shell neighbor-distance is 3.84 Å, with a statistical spread of 0.006 Å^2. The calculated bond distance is just slightly larger than the value of 3.83 Å found in an ideal crystal and the statistical spread is consistent with the values found for the first and second shell, ~0.006 Å^2 and ~0.005 Å^2 respectively. It would be convenient to be able to have

a *piori* knowledge of the amorphous structure. One source would be MD liquid-quench simulations of the amorphous structure. However, as shown in the Ref. [136], because of the large value of $\sigma^2_{In-In^*}$ in the amorphous structure even the results of the MD-simulations hold marginal utility in extracting information about the third shell in a-IO from the EXAFS results. The MD-simulations themselves can be used as a source of information about the third shell if the simulation can be validated by good agreement with the EXAFS results for the first and second shells.

The results of *ab initio* MD liquid-quench simulations for a-IO were analyzed. From the calculated radial pair distribution functions of the optimized structures, independent of the cell size, an average In-O bond distance, $\bar{R}_{In-O}$ ~ 2.16 Å, and an average In-O coordination number, $\bar{N}_{In-O}$ ~5.2, were obtained, in agreement with previously reported MD values for a-IO and other In-based oxide semiconductors [47, 49, 50, 68, 81, 84, 137, 138]. The value of $\bar{N}_{In-O}$ is also in excellent agreement with N_{In-O} obtained from the EXAFS results. The calculated In-O distances are slightly overestimated compared to the experimental values, as expected from the PBE approximation of the density-functional calculations [114]. For a more accurate comparison of the local order in the structures obtained via different cooling rates, the effective coordination number (ECN) and the average pair correlation function was calculated for each structure [125, 126]. The results are shown in Figure 10. Both $\bar{R}_{In-O}$ and $\bar{N}_{In-O}$ decrease as the cooling rate increases from 5 K/ps to about 250 K/ps, i.e., for more amorphous structures. A minimum for $\bar{R}_{In-O}$ and $\bar{N}_{In-O}$ values as well as a maximum value for of σ^2_{In-O} occur within 200-400K/ps cooling range; then, both $\bar{R}_{In-O}$ and $\bar{N}_{In-O}$ slightly increase in faster-cooled structures. The trend is in excellent agreement with the experimental ones observed for both N_{In-O} and R_{In-O} within the amorphous region of the deposition temperatures, Figure 6 a and b; the low temperature regions of Figure 6 are replotted in Figure 10. Thus, both the In-O bond length and the In-O coordination decrease upon amorphization; the obtained deviations in the first shell, however, cannot alter the electronic band structure (e.g., electron effective mass)

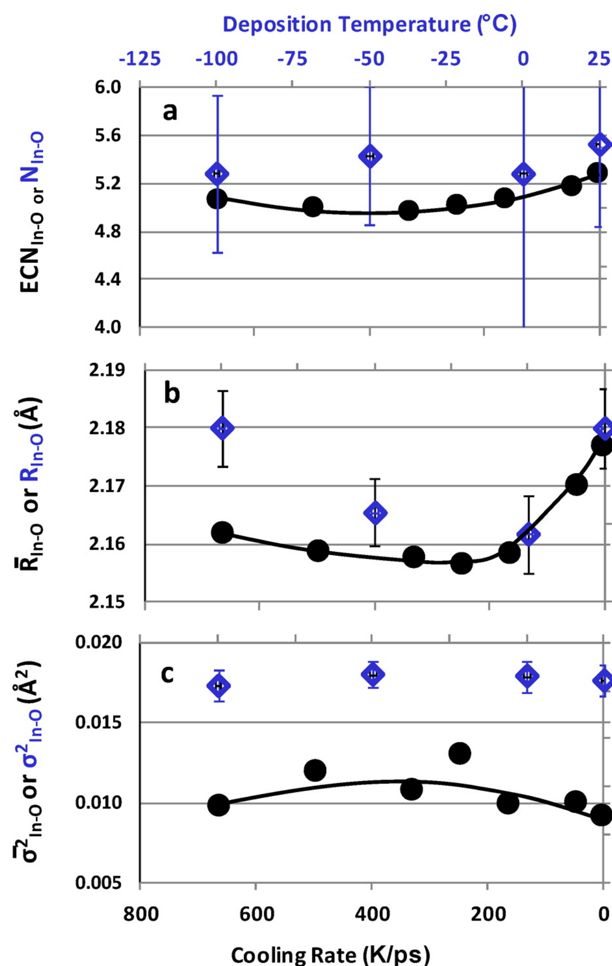

Figure 10. First-shell, In-O a) Effective coordination number, b) average bond distance, and c) bond-distance statistical-spread obtained from the MD simulations for 80-atom cell amorphous InO with different cooling rates on bottom axis (black circle markers). Blue diamond markers; low deposition temperature region (top axis) of EXAFS data.

sufficiently enough to explain the observed 3-fold change in the electron mobility, Figure 5. It should be noted that the alignment of the deposition temperature axis (upper axis) and the cooling rate axis (lower axis) of Figure 10 are based on a “fit by eye" and have no empirical correlation; the alignment, however, is consistent for all parts of Figures 10, 12 and 14.

As already mentioned above, experimental description of the In-In distribution in amorphous oxides is challenging; theoretical works also lack important details about the

In-In distances and coordination in amorphous oxides. The challenge arises from the proximity of the second and third shells (at 3.35 Å and 3.83 Å in *c*-IO), causing the corresponding pair distribution functions to overlap in the amorphous state. The total In-In distribution becomes over 1 Å wide, making the exponential fit in the ECN calculations inapplicable. In order to distinguish between the second and third shells, the optimized atomic coordinates of the MD simulated structures were used to perform the following analysis. For every In-atom the number of In-neighbors that share one, two, or three oxygen atoms with the central In-atom was determined. The resulting average In-In coordination numbers represent corner, edge, or face-shared In-In, respectively. In this analysis, the maximum In-O distance to be considered as an In-O bond was set to 2.36 Å. This cut-off value is greater than the longest first-shell In-O distance in crystalline In_2O_3 and ensures that most of the first-shell In-O distances in the In-O pair distribution function (i.e., those that belong to the first-shell peak) are included. The In-In pair distribution functions calculated separately for edge-shared and corner-shared In atoms are given in Figure 11a. In addition, the average In-In distances, coordination numbers and statistical spreads for both edge- and corner-shared In-In pairs were calculated, Figure 12. (The large statistical spread (Figure 12c) would certainly render the EXAFS data to contain little, if not be completely absent of, information on the third shell or corner-shared In-In interaction.) Based on the results, the following three important conclusions can be made:

1. The edge-shared In-In distances are distributed between 3.0 and 3.8 Å with the peak located around 3.3 Å, Figure 11a, which corresponds to the second shell edge-shared In-In distance in *c*-IO. The average In-In distance calculated for the edge-shared In-In pairs, $\bar{R}_{In-In}$, varies with cooling rate, Figure 12b: the lowest values of 3.26-3.27 Å were obtained for the structures cooled at 333K/ps-167K/ps. The trend in $\bar{R}_{In-In}$ agrees well with the experimental observation for the second shell R_{In-In}, Figure 9b, where the lowest value of 3.28 Å was observed for the structure deposited at 0°C. Furthermore, the calculated edge-shared In-In coordination, $\bar{N}_{In-In}$, remains at about 2.0 for all structures except for

the one cooled at the slowest rate, in excellent agreement with the experiment, Figure 9a. The value of $\bar{N}_{In-In}$ increases to 2.7 for the most “ordered" structure (5K/ps) as might be expected towards the onset of crystallinity. Thus, the number of edge-shared In-In does not determine the transport properties in oxides.

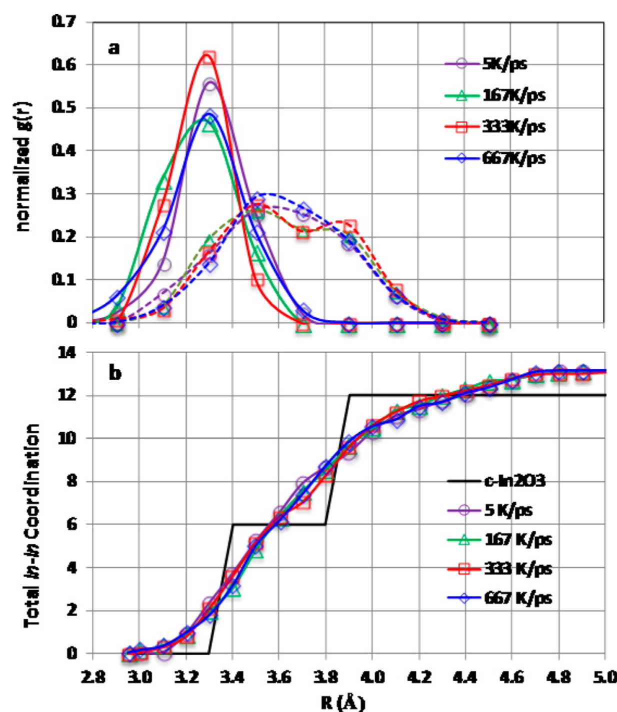

Figure 11. a) Pair distribution functions for edge-shared In-In (solid lines: centered at ~3.4 Å) and corner-shared In-In (dashed lines: centered at ~3.7 Å) as obtained from the MD simulations for 80-atom cell a-IO with different cooling rates. b) Total In-In coordination as a function of distance.

2: Although the edge-shared In-In coordination is significantly suppressed (from 6 to 2) in a-IO, the total In-In coordination which combines face-, edge-, corner, and non- sharing In-In pairs, remains close to the one for the c-IO Figure 11b: the total In-In coordination reaches 6 at about 3.6 Å and 12 at about 4.2 Å in all amorphous IO structures independent of the cooling rates. Hence, a significant part (about 60%) of the edge-shared In-In pairs become corner-shared upon amorphization, as, indeed, can be seen from the average corner-shared In-In coordination of about 8, Figure 13, left axis.

3: Accordingly, the corner-shared In-In distance distribution begins at around 3.0 Å, Figure 11a, resulting in a significant overlap with the edge-shared In-In distribution function. This finding highlights the challenge in distinguishing between the second and third shells from the general pair distribution function. Moreover, the corner-shared In-In distance distribution is almost twice as wide as the edge-shared one and includes long In-In distances at and above 4 Å. The average corner-shared In-In distance, $\bar{R}_{In-In^*}$, is about 3.63 Å for all structures (Figure 13, right axis) which is smaller than the crystalline corner-shared In-In distance of 3.8 Å. Because the In-O (first-shell) distances are generally preserved upon amorphization, c.f., Figures 6 and 10, the wide distribution of the corner-shared In-In distances determines the In-O-In angle distribution. The In-O-In angle defines the connection between the InO_x polyhedra as well as the molecular p-orbital of the oxygen atoms. To understand the role played by the In-O-In angle in the properties of amorphous oxides, the In-O-In angle distribution for corner- and edge-shared In-In pairs was calculated (given in the Ref. [136].)

As expected, the edge-shared In-O-In angle distribution is narrow with the average value of 98° which is close to the edge-shared In-O-In angle value of 99.5^o in c-IO. Also, the values of the average edge-shared In-O-In angle in a-IO vary insignificantly with the cooling rate. For the corner-shared In-In pairs, the average In-O-In angle is 115°, which does not have an analogous value in c-IO. The corner-shared In-O-In angle distribution function is wide, ranging from 95° to 130°, with two visible peaks at 109° and 124°. The latter angle value is close to the corner-shared In-O-In angle of 126° in c-IO. Importantly, the structures, obtained via intermediate cooling rates (333K/ps and 250K/ps), exhibit a plateau in the corner-shared In-O-In angle distribution having the weight of the first peak reduced, and a shoulder appears at 140°. Indeed, these structures exhibit the largest average In-O-In angle of 134° (calculated for corner-shared In-In distance range of 3.9-4.1 Å) as compared to 129-131° for both the fastest and slowest cooling rates.

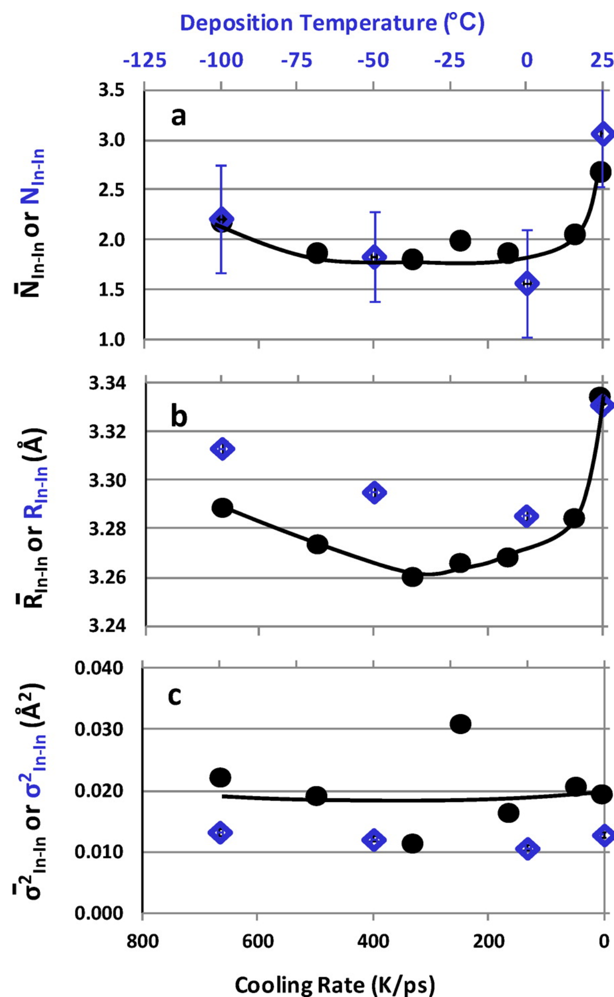

Figure 12. Second-shell, In-In a) Coordination number, b) average bond distance, and c) bond-distance statistical-spread obtained from the MD simulations for 80-atom cell *a*-IO with different cooling rates on bottom axis (black circle markers). Blue diamond markers; low deposition temperature region (top axis) of EXAFS.

Strikingly, the intermediate cooling rates resulted in the structures with the lowest distances, R_{In-O} ($\bar{R}_{In-O}$) and R_{In-In} ($\bar{R}_{In-In}$), and coordination numbers, N_{In-O} ($\bar{N}_{In-O}$) and N_{In-In} ($\bar{R}_{In-In}$), for the first and second shells as obtained both from the experiment and theoretical simulations. Since the structures with largest corner-shared In-O-In bond angle (obtained via intermediate cooling rates, 333K/ps and 250K/ps) seem to correspond to the highest mobility observed near the deposition temperature of 0°C (Figure 4), it is critical to investigate this further. A large In-O-In angle may suggest a higher-symmetry molecular

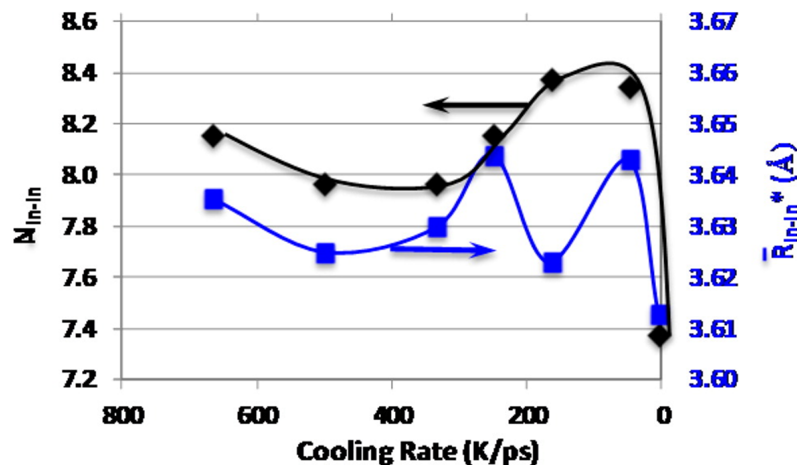

Figure 13. Third-shell, black diamonds: left axis, In-In* coordination number; blue squares: right axis, average bond distance.

orbital for the oxygen p-states, and, hence, a better overlap between the spherical s-states of In atoms with the two directional p-orbitals of the shared oxygen atom, giving rise to a smaller electron effective mass. However, the obtained angle deviations cannot result in a significant change in the effective mass; another mechanism should be responsible for the observed three-fold mobility increase near the amorphous-crystalline transition. As mentioned above, the In-O-In angle determines the spatial distribution of the InO_x polyhedral, i.e., the way the InO_x polyhedra are connected. Large corner-shared In-O-In angles correspond to a longer In-In distances (of ~4.0 Å on average); hence, one can suggest a formation of connected In-O-In chains in these structures. Spatially spread, connected chains may represent long conductivity paths and lead to an enhanced mobility.

To verify the above assumption, the atomic structures of the a-IO obtained via different cooling rates were analyzed. First, we identify the InO_6 polyhedra in every structure and determine the number of the corner- and edge-shared pairs for the InO_6 polyhedra only; Figure 14 is the percentage of edge-shared InO_6-InO_6 bonds as a function of cooling rate. We find that the slow-cooled structure (5 K/ps) possesses the largest number of edge-shared InO_6-InO_6 bonds (above 50%), whereas for fast-cooled structures

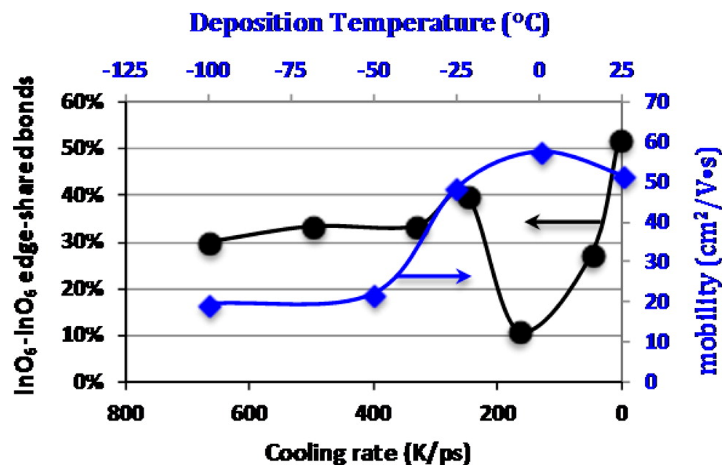

Figure 14. Percent contribution edge-shared InO_6-InO_6 polyhedra with respect to total (edge and corner) shared InO_6 pairs as a function of cooling rate (black): Low temperature region of Hall mobility versus deposition temperature curve of Figure 5 (blue).

(300 K/ps and above), the contribution from the edge-shared InO_6 pairs remains at about 30%. Most strikingly, the number of edge-shared InO_6 pairs is suppressed to as low as 10% for the structure obtained via 166 K/ps cooling rate so that the InO_6 polyhedra are primarily connected via corner-sharing polyhedra. Also plotted on Figure 14 is the low temperature region of Figure 5, Hall mobility as a function of deposition temperature. The maximum in mobility coincides with the minimum in edge-shared InO_6 pairs; the alignment of the deposition temperature and cooling rate scale is consistent with that used to compare the simulations with the EXAFS data.

In Figure 15, the spatial distributions of the InO_6 polyhedra are plotted for the representative structures-those obtained via 500 K/ps, 250 K/ps, and 50K/ps quench rates. The following important observations are made. In the fast-cooled samples (500 K/ps and above), disconnected InO_6 polyhedra and small clusters of 2-3 InO_6 polyhedra connected via corner sharing were found. In contrast, the samples obtained via intermediate cooling rates (333-167 K/ps) feature long chains of mostly corner-shared InO_6 polyhedra. As discussed above, these cooling rates correspond to an increased probability for large In-O-In angles and long In-In distances. Consequently, at these cooling rates the InO_6 are connected

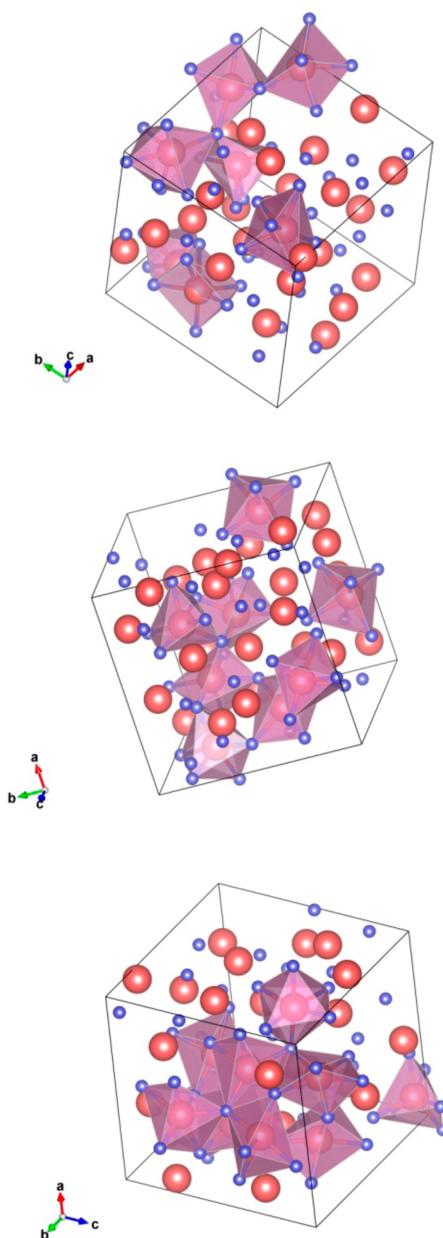

Figure 15. Spatial distribution and connectivity of the InO_6 polyhedra in amorphous InO obtained via 500 K/ps (top), 250 K/ps (middle), and 50 K/ps (bottom) cooling rates. Indium and oxygen atoms are shown with large (red) and small (blue) balls. Only InO_6 polyhedra are shown in these plots.

throughout the cell, enabling continuing conductivity paths for charge carriers. At a slower cooling rate, the number of edge-shared In-In pairs increases, Figures 9a and 12a. Indeed, in the slow-cooled samples (50-5K/ps), large clusters of InO_6 connected via edge and

face sharing were found. Such clusters represent the on-set of nucleation of crystallites observed above the amorphous-crystalline transition (i.e., above the room temperature), Figure 4. The presence of such crystallites in the multiphase system leads to an enhanced scattering and, hence, to a decreased mobility. From additional MD simulations of a-IO within an 180-atom cell, the trends in the spatial distribution of InO_6 polyhedra with the cooling rates were confirmed; moreover, it was found that at slow cooling rates (83 K/ps) the large InO_6 clusters are disconnected from each other, even at an In-In distance as large as 4.0 Å.

5. CONCLUSIONS

Thorough experimental and theoretical analyses of the structural characteristics of IO systems reveal the key mechanisms governing the properties of this oxide under amorphous-to-crystalline transition. The EXAFS and MD results for coordination numbers, bond distances, and statistical spreads are consistent with a concept of an amorphous oxide structure as one built of InO_x polyhedra joined at the corners or edges to form a network structure in which the number of edge-sharing polyhedra are greatly diminished. Based on excellent agreement between EXAFS experimental results and MD liquid quench simulations obtained for the first and second shells of *a*-IO, important conclusions about the third shell (corner-shared In-In) were derived from the MD simulations.

The local maximum in Hall mobility observed at the onset of crystallinity has several plausible contributing factors. The minimum in the first shell (In-O) and the second shell (In-In) bond distances coincides with the maximum in mobility and can be a contributing factor to a small effective mass. Significant reduction of the edge-shared In-In coordination (from 6 to 2) is associated with a wide distribution of the corner-shared In-In distances and the corresponding In-O-In bond angles that determine the interconnection of the InO_x polyhedra. Large In-O-In bond angles facilitate higher symmetry p-orbital on the shared

oxygen atom leading to a better overlap with the s-states of In atoms. A more significant factor that results from the increase in the In-O-In bond angle, however, is a transition from disconnected InO_x clusters to extended connected chains of InO_x polyhedra that can form long conductivity-paths. The in-depth understanding of the structural characteristics opens up a route to attain optimal properties in technologically viable amorphous oxide semiconductors.

6. ACKNOWLEDGMENTS

For this research, R.P.H.C., R.K., and J.E.M. were supported by the MRSEC program of the National Science Foundation at Northwestern University under grant no. DMR-1121262. D.B.B. was supported by the U.S. Department of Energy, Office of Science, Office of Basic Energy Sciences under the Award Number DE-FG02-06ER46320. This work made use of the J.B. Cohen X-ray Diffraction Facility supported by the MRSEC program of the National Science Foundation (DMR-1121262) at the Materials Research Center of Northwestern University; the Optical Microscopy and Metallography Facility MRSEC program of the National Science Foundation. X-ray absorption measurements were performed at the DuPont-Northwestern-Dow Collaborative Access Team (DND-CAT) located at Sector 5 of the Advanced Photon Source (APS). DND-CAT is supported by E.I. DuPont de Nemours & Co., The Dow Chemical Company, and Northwestern University. Use of the APS, an Office of Science User Facility operated for the U.S. Department of Energy (DOE) Office of Science by Argonne National Laboratory, was supported by the U.S. DOE under Contract No. DE-AC02-06CH11357. Computational resources were provided by the NSF-supported XSEDE program, grant TG-DMR080007. Electron microscopy was supported by the National Center for Research Resources (5 G12RR013646-12) and Department of Defense #64756-RT-REP. D.A., A.P., and M.J.-Y. also thank NSF PREM Grant # DMR 0934218.

II. LONG-RANGE STRUCTURAL CORRELATIONS IN AMORPHOUS TERNARY IN-BASED OXIDES

Julia E. Medvedeva, Rabi Khanal

Department of Physics, Missouri University of Science & Technology,

Rolla, MO 65409

ABSTRACT[*]

Systematic investigations of ternary In-based amorphous oxides, In-X-O with X=Sn, Zn, Ga, Cd, Ge, Sc, Y, or La, are performed using ab-initio molecular-dynamics liquid-quench simulations. The results reveal that the local M-O structure remains nearly intact upon crystalline to amorphous transition and exhibit weak dependence on the composition. In marked contrast, the structural characteristics of the metal-metal shell, namely, the M-M distances and M-O-M angles that determine how MO polyhedra are connected into a network, are affected by the presence of X. Complex interplay between several factors such as the cation ionic size, metal-oxygen bond strength, as well as the natural preference for edge, corner, or face-sharing between the MO polyhedra, leads to a correlated behavior in the long-range structure. These findings highlight the mechanisms of the amorphous structure formation as well as the specifics of the carrier transport in these oxides.

[*]Published in VACUUM **114** 142-149 (2015).

1. INTRODUCTION

Although the unique properties of transparent amorphous oxide conducting and semiconducting materials were first demonstrated almost a decade ago [32, 42], basic structural properties of these oxides – namely, the structural characteristics associated with the crystalline-to-amorphous transition – are far from understood. Most of the experimental characterization of the transparent amorphous oxides deal almost exclusively with the first shell, i.e., the coordination of oxygen atoms around metal cations [43, 45, 51, 54, 56, 145, 146]. Similarly, available theoretical models derived from molecular dynamics (MD) simulations of the amorphous oxides focus primarily on the Metal-Oxygen data with no or limited information on the Metal-Metal distances and coordination [47, 49, 50, 68, 81, 84, 137, 138, 139]. However, the first-shell remains nearly intact upon the crystalline-to-amorphous transition, owing to the strong oxygen electronegativity. Instead, integration of the Metal-Oxygen polyhedra into a continuous network – governed by the Metal-Metal distances, coordination, and oxygen sharing – plays a key role in the formation and properties of the amorphous oxides. Indeed, recent experimental and theoretical investigations of amorphous indium oxide [147] revealed that interconnectivity and spatial distribution of the InO polyhedra determines the electron transport limited by charge scattering: the observed peak in the electron mobility was found to correspond to the structure with long chains of InO_6 polyhedra connected primarily via corner sharing.

To gain a thorough systematic understanding of the role of composition in the structural properties of amorphous In-based oxides, eight ternary In-X-O structures with X=Sn, Zn, Ga, Cd, Ge, Sc, Y, or La, denoted below as a-IXO, were modelled using liquid-quench MD simulations. The choice for X cations in this study covers the typical compositional chemistry in both crystalline and amorphous transparent conducting and semiconducting oxides: all cations are pre- or post-transition metals with ns^0 electronic configuration. The structural characteristics of the first, second, and third shells as well

as the connectivity between the MO polyhedra are compared for amorphous indium oxide (a-IO) and a-IXO. The results highlight the importance of the spatial distribution of the InO_6 and XO polyhedra from the point of view of amorphization and charge transport and facilitate the progress in fundamental understanding of amorphous oxides.

2. COMPUTATIONAL METHOD

The amorphous a-InO and a-InXO structures were generated using first-principles molecular dynamics as implemented in the Vienna Ab Initio Simulation package (VASP)[105, 116, 117, 118]. The calculations are based on the density functional theory (DFT)[102, 103] with PBE functional based on the projector augmented-wave method [115, 122, 148]. For the initial structure, we used a cubic 130-atom cell of bixbyite In_2O_3 with density 7.12 gm/cm^3. To obtain ternary IXO structures, we randomly replaced 20% of the In atoms in the initial structure by respective metal X (Sn, Zn, Ga, Cd, Ge, Sc, Y or La) and adjusted (i) the number of oxygen atoms to maintain stoichiometry; and (ii) the cell volume to maintain the density in the In-based samples. The resulting lattice parameters that we have used in our studies are: 11.898 Å for InO; 12.11 Å for InSnO; 11.78 Å for InZnO; 11.80 Å for InGaO; 12.06 Å for InCdO; 11.86 Å for InGeO; 11.66 Å for InScO; 11.91 Å for InYO; and 12.17 Å for InLaO.

For each initial IO or IXO structure, we performed molecular dynamics simulations of liquid quench as follows. First, to remove any crystalline memory, each initial structure was melted at 3000 K for 6 ps. The melt was then cooled to 1700 K at the rate of 100 K/1.2 ps, and then rapidly quenched to 100 K at the rate of 200 K/1.2 ps. In order to make the calculations computationally efficient, we used low cut-off of 260 eV and restricted the k-point sampling to Γ point only during melting and quenching processes. Finally, each structure was equilibrated at 300 K for 6 ps with a cut-off energy of 400 eV. All simulations

were carried out within NVT ensemble with Nosẽ Hoover thermostat using integration time step of 2 fs.

3. RESULTS AND DISCUSSION

3.1. In-O and X-O distances in amorphous IO and IXO.

To understand the role of composition in the structural properties of amorphous In-based oxides, first, the local structure of the InO_x polyhedra in a-IO and a-IXO with X=Sn, Zn, Ga, Cd, Ge, Sc, Y, or La, is analysed. For this, the distribution of the In-O distances and the In coordination with oxygen atoms in a-IXO are compared to the corresponding In-O values in a-IO as well as those in crystalline In_2O_3. For an accurate comparison of the average In-O distances in a-IO and a-IXO, the average pair correlation function [125, 126] was calculated according to:

$$l_{av} = \frac{\sum_i l_i \, exp\left(1 - \left(\frac{l_i}{l_{min}}\right)^6\right)}{\sum_i exp\left(1 - \left(\frac{l_i}{l_{min}}\right)^6\right)} \tag{1}$$

where the summation runs over all oxygen neighbors of a particular In atom and l_{min} is the smallest In-O distance in the i-th InO_x polyhedron. The results, shown in Fig. 1, reveal that the average pair correlation function increases for X=Sn, Zn, Ga, or Ge, and decreases for X=Cd, Sc, La, or Y, with respect to the In-O value in a-IO. The average In-O distance in all In-based oxides remains to be below the corresponding value in crystalline In_2O_3, namely, 2.18 Å. The shortest average In-O distance in case of a-IYO is in accord with the short In-O distance in crystalline hexagonal $YInO_3$, namely, 2.10 Å.

The above trends in the average In-O distance in a-IXO, Fig. 1, reveal no correlation with the ionic radii of the X cations. Indeed, the In-O distance cannot be affected directly by the presence of X cation since the In-O-M bond angle (M=In or X) is significantly less than 180° (on average, the In-O-M angles are equal to 98° and 116° for edge- and corner-shared

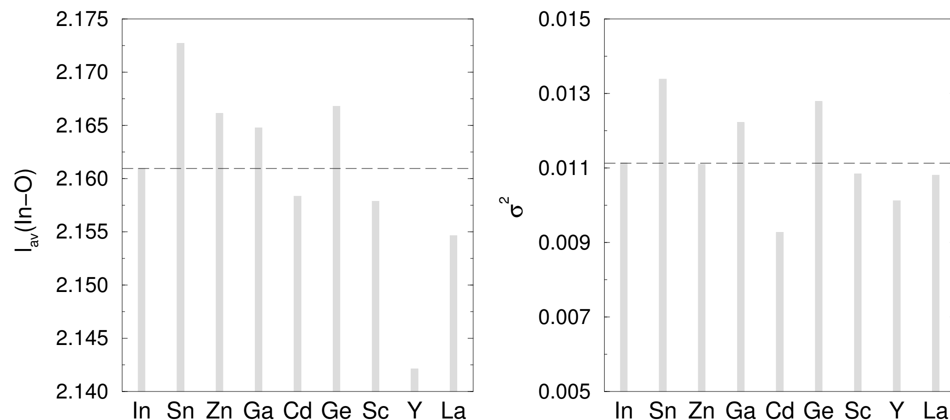

Figure 1. (Left) Calculated average In-O pair correlation function, l_{av}, in Å, for amorphous IO and IXO. (Right) Calculated standard deviation of the radial In-O distance distribution, σ^2, in Å^2, for amorphous IO and IXO. The horizontal dash lines represent the corresponding values in amorphous IO.

In-M pairs, respectively.) For all X, the changes in the average In-O correlation function are insignificant, i.e., less than 1 %. Moreover, the presence of X appears to have little effect on the radial In-O distance distribution: the calculated standard deviation, σ^2, shows only a small variation with composition, Fig. 1. The standard deviation increases for X=Ga or Ge which may be explained by their small ionic radii and the strength of the X-O bonds. A different mechanism should be sought for X=Sn in order to explain the increase of the average In-O distance and the distance distribution in a-ITO with respect to a-IO, c.f., Fig. 1. We believe that spatial distribution and connectivity of SnO_x and InO_6 polyhedra in a-ITO are important in determining the structural characteristics, as described below.

It is important to stress that local changes in the InO structure averaged out by the standard characterization procedures, Fig. 1, may be important from the crystallization and charge transport points of view. In particular, the strength of the X-O bonds with respect to that of the In-O bond (the so-called “oxygen-getter" behavior of X cation [149]) may affect the local In-O structure: (i) by introducing a “ripple” effect when the In-O bond distance fluctuates with the number of X neighbors [150]; and (ii) by changing the relative contributions from the differently coordinated In atoms (discussed below). Clearly, the

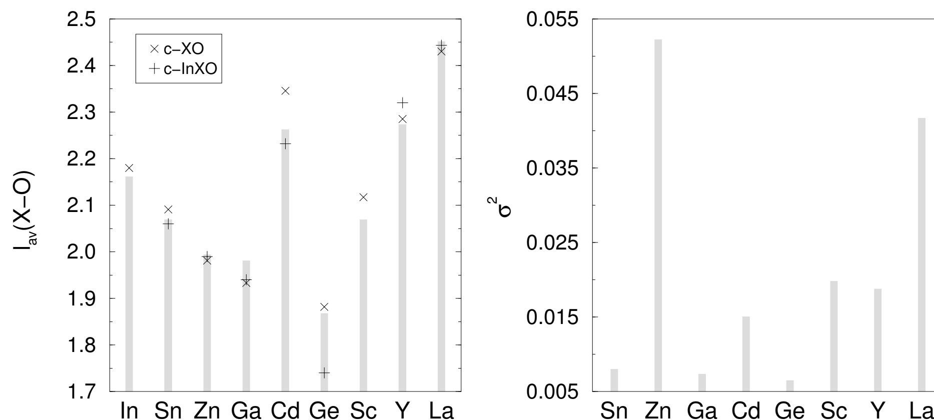

Figure 2. (Left) Average X-O correlation function, l_{av}, in Å, in amorphous IXO. Also, the X-O distance in the corresponding crystalline binary (cross) and In-containing ternary (plus) oxides are given for comparison. (Right) Calculated standard deviation of the radial X-O distance distribution, σ^2, in Å^2, for amorphous IXO.

spatial distribution of XO polyhedra within the InO framework (e.g., clustering *vs* uniform distribution of XO) becomes critical in determining the crystalline to amorphous transition as well as the transport properties (conductivity paths and scattering) in multicomponent oxides and will be addressed below.

The calculated average pair correlation function l_{av}(X-O), Eq. 1, for each a-IXO structure is given in Fig. 2. The results reveal that for X=Sn, Cd, Ge, Sc, or Y (for X=Zn, Ga, or La), the average X-O distance is shorter (longer) than the natural X-O distance, i.e., the distance in the corresponding crystalline binary oxides. Interestingly, the X-O distances in the available crystalline ternary In-containing oxides (we considered $In_4Sn_3O_{12}$, In_2ZnO_4, $GaInO_3$, $CdIn_2O_4$, $In_2Ge_2O_7$, $YInO_3$, and $LaInO_3$; all structural properties found in the Inorganic Crystal Structure Database), in general, predict the average X-O distances in a-IXO rather well (e.g., for X=Sn, Zn, Cd, or La). However, the preference of the X cation to have a particular oxygen coordination should be taken into consideration. For example, about a half of Ge atoms are found to be six-coordinated in a-IGeO (similar to rutile GeO_2) whereas Ge is four-coordinated with oxygen atoms in $In_2Ge_2O_7$; hence, the Ge-O distance in a-IGeO deviates significantly from that in $In_2Ge_2O_7$, Fig. 2.

In marked contrast to the small variation in the standard deviation for the In-O distances in a-IXO, Fig. 1, the X-O distance distribution is narrow only for X=Sn, Ga, and Ge, Fig. 2. (Note that the the standard deviation for the In-O distances is large for these three cases, Fig. 1). The calculated standard deviation, σ^2, is above 0.015 Å^2 for X=Cd, Sc, and Y, that is notably larger than the corresponding In-O value in a-IXO (c.f., Fig. 1). Most significantly, the standard deviation is above 0.04 Å^2 and 0.05 Å^2 for X=La and Zn, respectively. The corresponding radial X-O distributions are asymmetric towards longer distances, i.e., there is an appreciable amount of long-distance Zn-O and La-O bonds. This finding may be explained by the Zn and La tendency to be over-coordinated: many Zn and La atoms acquire higher than natural coordination in a-IXO (see below). This is in accord with crystalline oxides: La has 8 oxygen neighbors in $InLaO_3$ and Zn is five-coordinated in crystalline multicomponent oxides [151, 152]. The presence of the long-distance X-O bonds may favor connectivity between the XO polyhedra via corner-sharing – as opposed to isolated short-bonded polyhedra or clusters of edge-shared polyhedra.

3.2. In-O and X-O coordination in amorphous IO and IXO. Based on the obtained pair correlation function (Eq. 1), the effective coordination number (ECN) can be calculated as follows:

$$\mathrm{ECN} = \sum_{i} \exp\left(1 - \left(\frac{l_i}{l_{av}}\right)^6\right). \qquad (2)$$

The average effective coordination numbers calculated for a-IXO, Fig. 3, reveal that indium is under-coordinated with oxygen atoms in all In-based amorphous oxides – as compared to the crystalline In_2O_3 with six-coordinated In atoms. Moreover, at 20 % substitution, all X additions considered in this work have little effect on the average In-O coordination changing it only slightly as compared to <ECN>=5.0 in a-IO: Sn, Zn, Ga, and Y result in <ECN>~5.1, whereas Ge and Sc increase it to <ECN>~5.3. La has the smallest effect on the average In coordination whereas Cd decreases it to 4.98.

Although the average In-O coordination remains nearly unchanged in a-IXO, the statistical distribution of the In coordination, i.e., the relative number of differently coordinated In atoms, reveals a strong dependence on the composition. Within a radial distance of 2.36 Å from a central In atom (to be compared to the longest In-O distance in the first shell in crystalline In_2O_3, 2.25 Å), there are three, four, five, and six-coordinated In atoms, denoted below as InO_x, Fig. 4. In a-IO and all a-IXO except for IGeO and IScO, most of the In atoms (around 50 % or above) are five-coordinated. The number of six-coordinated In atoms in a-IXO suggests a particular grouping of the addition elements. Specifically, Sn stands apart from the other X additions since it has the least effect on the In coordination statistics. X=Cd, Y, and La result in an increase of both the five- and six-coordinated In atoms. In contrast, for X=Zn, Ga, Ge, and Sc, only the number of six-coordinated In increases – up to 30 % for Zn or Ga and up to 40 % for Ge and Sc. Hence, addition of Ge or Sc leads to the most pronounced tendency to fulfil the natural In coordination. As discussed below, spatial distribution and connectivity of the InO_6 plays the key role during amorphization of In-based oxides and may also govern the charge transport.

In contrast to under-coordinated In, the average coordination of all the addition elements except for Cd and Sc is close to their natural coordination, i.e., the coordination in the corresponding crystalline binary oxides. In a-IXO, Ga and Ge are, on average, five-coordinated (both can be found four and six-coordinated in binary oxides); Y and La reach or exceed their natural coordination of six; Sn and Zn are close to being six- or four-coordinated, respectively, in accord with their coordination in binary oxides. Only Sc and especially Cd are notably under-coordinated; both have the natural coordination of 6 in the corresponding binary oxides. We note that the low coordination of Cd in amorphous ICdO (4.5) is in accord with crystalline ternary oxide In_2CdO_4 where Cd is four-coordinated. This may be explained by weaker Cd-O bonds as compared to the In-O bonds.

3.3. In-M coordination and distances. Amorphous oxide structure can be considered as a network of distorted MO polyhedra. A thorough understanding of the In-M

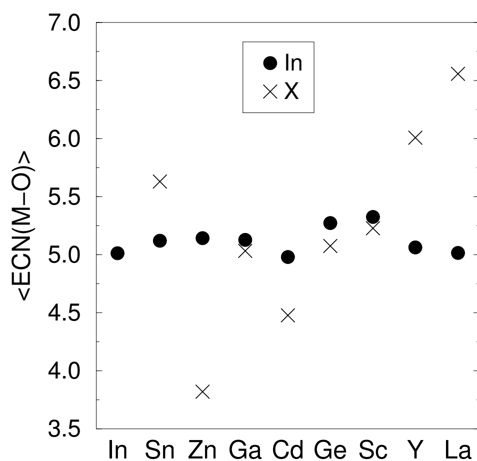

Figure 3. Average effective coordination number of In with oxygen atoms in amorphous IO and IXO.

shell structure, i.e., the average In-M distances and In-O-M angles, provides valuable information about interconnectivity between the MO polyhedra. However, characterization of the In-M shell is challenging. The proximity of the second and third shells in the crystalline In_2O_3 associated with six edge-shared In-In bonds at ~3.35 Å and six corner-shared In-In bonds at ~3.83 Å, respectively, leads to significant overlap of the corresponding distribution functions in amorphous indium oxide [147]. Hence, it is hard to distinguish between the second and third shells from a measured general pair distribution function. Moreover, the total In-M distance distribution becomes over 1 Å wide, making the exponential fit in the l_{av} and ECN calculations, Eqs. 1 and 2, inapplicable in this case.

Independent of the type of sharing (edge vs corner), the total In-M coordination (or running coordination) can be calculated as a function of the distance from a central In atom. In amorphous IO, it reaches the expected 6.0 (12.0) at ~3.6 Å (4.3 Å), i.e., above the crystalline In_2O_3 value of 3.4 Å (3.8 Å). Addition of Ga, Zn, Ge, Sc, Y or Cd increases the total In-M coordination as compared to that in a-IO, whereas Sn or La slightly reduces it, Fig. 5. These results do not correlate with the ionic size of the X cation: the ionic radius of La (1.17 Å) is the largest among all X cations considered, while the ionic radius of Sn

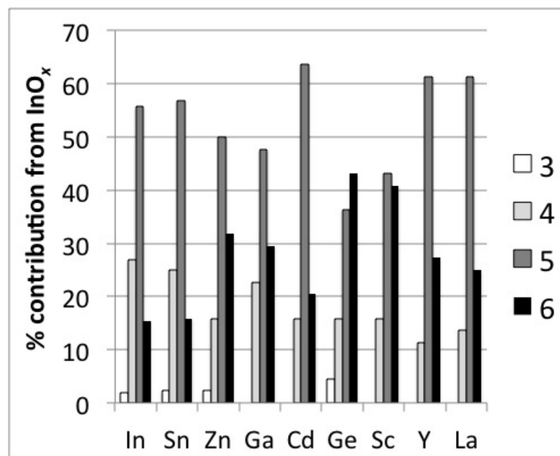

Figure 4. Relative number of differently coordinated indium atoms in amorphous IO and IXO calculated within 2.36 Å around a central In atom.

(0.83 Å) is smaller than that of In (0.94 Å) as well as of Sc (0.89 Å), Y (1.04 Å), or Cd (1.09 Å). The Sn- or La-induced decrease of the total In-O coordination is in accord with the longest average In-O distance in a-ITO, Fig. 1, and the strong tendency of La toward over-coordination in a-ILaO, Fig. 3.

To distinguish between the edge- and corner-shared In-M pairs, we determine the number of metal neighbors (In or X) that share one, two, or three oxygen atoms with a central M atom. The resulting In-M coordination numbers represent the number of corner, edge, or face-shared metal atoms, respectively, for every M atom. In this analysis, one should choose a maximum metal-O distance to be considered as M-O bond in the metal-metal sharing – this cut-off value should ensure that the first shell M-O distances in the corresponding pair distribution function (i.e., those that belong to the first In-O or X-O peak) are included into consideration. In our analysis, we set the cut-off values to 2.36 Å for In-O bond and Sn-O bond; 2.20 Å for Zn-O bond and Ga-O bond; 2.10 Å for Ge-O bond; 2.27 Å for Sc-O bond; 2.44 Å for Y-O bond; 2.55 Å for Cd-O bond; and 2.75 Å for La-O bond. As a result, average M-M distance and M-O-M angle for edge-, corner-, and face-shared M-M pairs are derived for each oxide.

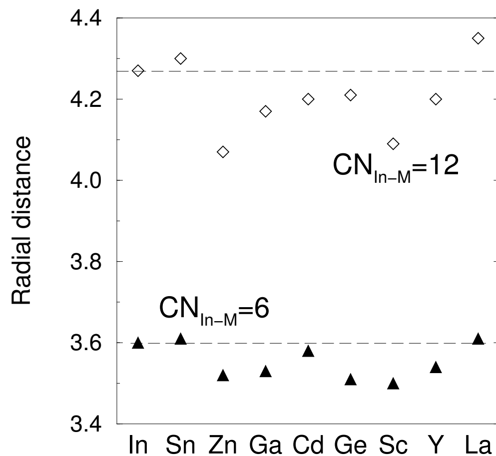

Figure 5. Radial distance, in Å, from a central In atom at which the average In-M coordination number becomes 6.0 (triangles) and 12.0 (diamonds) in a-IO and a-IXO. The horizontal dash line corresponds to the values for a-IO and is given to guide the eye.

First of all, we find that addition of X=Sn or Cd does not change the relative number of the edge- *vs* corner-shared In-In pairs which is 15% *vs* 85%, respectively, of the total shared In-In pairs in a-IO as well as in a-ITO and a-ICdO. The number of edge-shared In-In pairs increases to 19-21% for all other X cations. The low number of edge-shared In-In pairs in In-based oxides (about a half of the edge-shared pairs become corner-shared upon amorphization) does not translate into a low mobility in amorphous oxides. Indeed, the observed mobility peak in a-IO was found to correspond to the structure with the *smallest* edge-shared In-In coordination number [147]. This counter-intuitive result was explained by the abundance of long-distance corner-shared In-In pairs that enables formation of long chains of connected InO_6 polyhedra [147]. The extended InO_6 chains (as opposed to InO_6 clusters of edge-shared polyhedra) are believed to be responsible for lower scattering and, hence, an improved mobility.

The average In-In distance and In-O-In angle for both edge- and corner-shared In-In pairs in a-IO and a-IXO are given in Figure 6. There is a correlation between the average In-In distance for edge-shared and corner-shared In-In pairs: a shorter edge-shared distance generally correspond to a longer corner-shared distance, and vice versa. Accordingly,

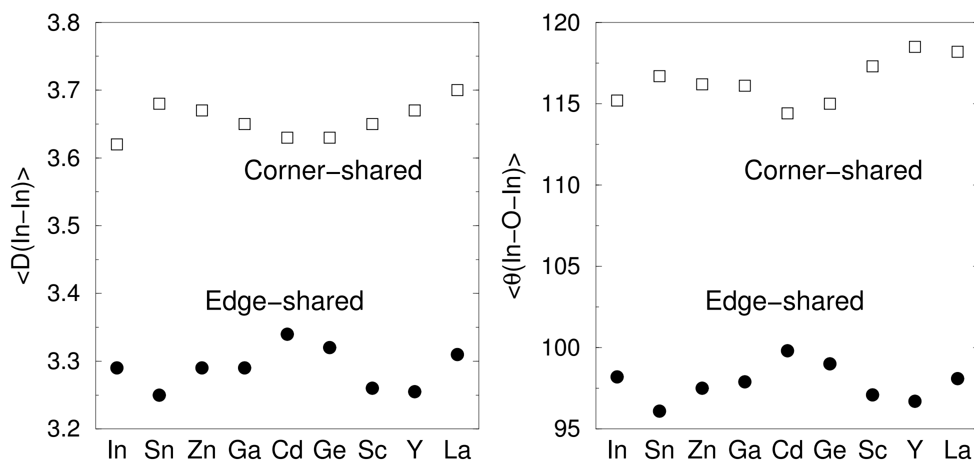

Figure 6. Average In-In distance, in Å (left) and average In-O-In angle, in degrees, (right) for edge-shared (circle) and corner-shared (square) In-In pairs in amorphous IO and IXO. For comparison, the crystalline In_2O_3 edge-shared and corner-shared In-In distances are 3.4 Å and 3.8 Å, respectively, and average In-O-In angles are 99-101° and 126°, respectively.

the average In-O-In angles for the edge-shared and corner-shared In-In pairs show a clear correlation, Fig. 6(b). However, the effect of X is more complex: only X=Sn, Sc, or Y reduce the average edge-shared In-In distance, whereas all X additions increase the average corner-shared In-In distance as compared to those in a-IO. The longest corner-shared In-In distance in a-ITO and a-ILaO is in accord with the increased total In-M coordination which may be explained by the Sn and La tendency toward overcoordination and clustering. Therefore, owing to the higher degree of freedom, the corner-shared In-In pairs serve to compensate changes in the edge-shared shell (if any) as well as to adjust to the presence and spatial distribution of XO polyhedra.

3.4. InO_6 connectivity and spatial distribution. The reduced number of edge-shared In-In pairs in the amorphous In-based oxides signifies changes in the connectivity between InO polyhedra upon crystalline-to-amorphous transition. For amorphous InO, it has been shown that the size and distribution of nanocrystalline In_2O_3 inclusions which are present in the amorphous oxide samples even below the transition to the so-called "X-ray amorphous" state, limit the transport properties via scattering [147]. Nucleation of

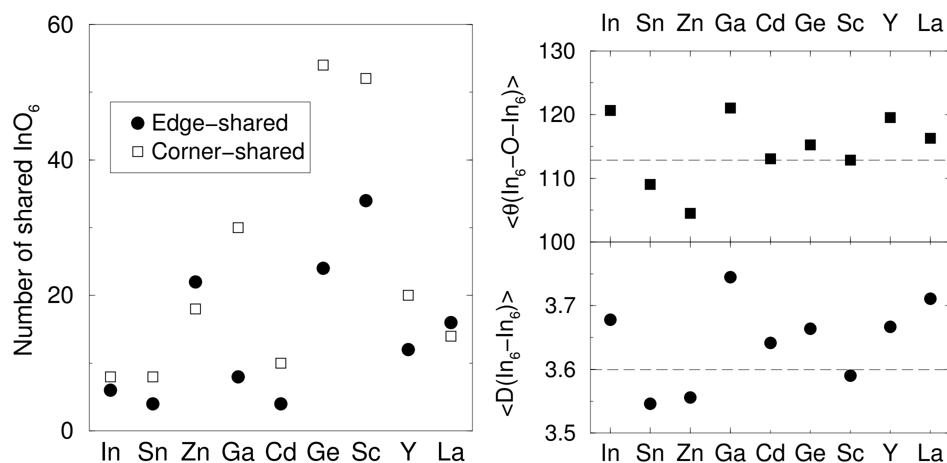

Figure 7. (Left) Number of edge-shared and corner-shared In_6-In_6 pairs in amorphous IO and IXO. (Right) Average In_6-In_6 distance, in Å, and average In_6-O-In_6 angle, in degrees, for the InO_6 polyhedra connected via edge- and corner-sharing in amorphous IO and IXO. The horizontal dash line represents the corresponding values averaged for the second and third shells in crystalline In_2O_3.

such nanocrystallites was found in amorphous InO structures obtained via MD simulations at slow cooling rates (5K/ps), and it was shown that the spatial distribution of the InO_6, i.e., homogeneous distribution of separate-standing (i.e., not connected) InO_6 polyhedra vs chains vs clusters, depends strongly on the deposition temperature in PLD-grown samples or quench rates in MD simulated structures and ultimately determines the properties of amorphous indium oxide [147]. In this work, the MD quench rates employed for a-IO and a-IXO (170 K/ps) are expected to be fast enough to prevent InO_6 clustering and, hence, to avoid nucleation of In_2O_3 nanocrystallites. Indeed, in a-IO obtained at this cooling rate, only 13% of In atoms are six-coordinated, and these InO_6 are distributed uniformly throughout the cell volume: the number of connected InO_6 (via edge or corner-sharing) is small, Fig. 7, and the average distance between shared InO_6 polyhedra is 3.68 Å which is greater than the average shared In-In distance in crystalline In_2O_3, 3.6 Å. The latter is primarily due to the presence of long-distance corner-shared InO_6-InO_6 pairs that result in the average corner-shared In_6-O-In_6 angle of 138° (to compare, the average corner-shared In-O-In angle in crystalline In_2O_3 is 126°).

Significantly, all X cations considered in this work except for Sn increase the number of six-coordinated In atoms, Fig. 4. The number of connected InO_6 polyhedra increases accordingly, Fig. 7, but composition also affects the way the InO_6 polyhedra connect with each other, i.e., the relative number of edge- vs corner-shared In_6-In_6 pairs is different in a-IXO, Fig. 7. In particular, although Sn has little effect on the fractional number of six-coordinated In atoms, Fig. 4, it affects the spatial distribution of the In_6 atoms by suppressing the number of edge-shared InO_6 polyhedra, Fig. 7. At the same time, Sn leads to the formation of short-distant edge-shared In_6 pairs (~3.1 Å) that results in the smallest average distance between connected In_6-In_6, Fig. 7. The effect of composition is manifested clearly when the InO_6 features are compared for a-IZO and a-IGO. In these oxides, the relative number of six-coordinated In atoms is nearly the same (and doubled as compared to a-IO and a-ITO, Fig. 4); however, Zn promotes edge-sharing between the InO_6 polyhedra whereas Ga favors their corner-sharing, Fig. 7. Such differences in the InO_6 connectivity are likely to reflect different charge transport in a-IZO and a-IGO.

The average In_6-In_6 distance for the connected InO_6 polyhedra in a-IXO varies with composition: it increases for X=Ga or La; decreases for X=Sn, Zn, or Sc; and remains similar to that in a-IO for X=Ge, Y, or Cd, Fig. 7. The variation does not follow the trend in the fractional number of In_6 (c.f., Fig. 4) and does not correlate with the ionic size of X. This finding highlights that different composition-dependent mechanisms are responsible for the formation of the amorphous oxide structure, and also may signify a tendency toward InO_6 clustering in some a-IXO. To verify this assumption, the number of In_6 neighbors was calculated within a radial cut-off distance of 3.8 Å from a central In_6. (Note that oxygen sharing, i.e., connectivity between the InO_6 polyhedra, was not taken into account in these calculations, and the distance of 3.8 Å is simply to include the In-In distance of the second and third shells in crystalline In_2O_3). The results are grouped according to the fractional number of six-coordinated In atoms (c.f., Fig. 4) for comparison. One can see, Fig. 8, that addition of Cd increases the probability of finding 5 In_6 neighbors as compared to a-IO.

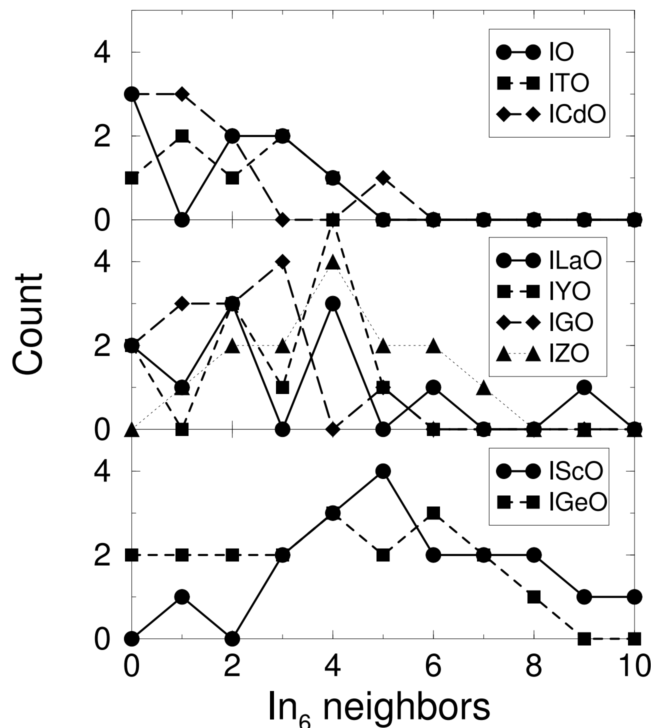

Figure 8. The probability of the number of In_6 neighbors calculated within a radial cut-off distance of 3.8 Å from a central In_6 in a-IO and a-IXO. The oxides are grouped according to the fractional number of the six-coordinated In atoms, c.f., Fig. 4, that is ~20 % for a-IO, a-ITO, and a-ICdO; ~30 % for a-ILaO, a-IYO, a-IGO, and a-IZO; ~40 % for a-IScO, and a-IGeO.

For X=Y, La, Ga, and Zn, the fractional number of In_6 increases to about 30 %, yet the spacial distribution of the InO_6 polyhedra is different: in a-IGO and a-IYO, the number of In_6 neighbors does not exceed 5, whereas in a-ILaO there is a cluster of as many as 9 In_6 neighbors. Amorphous IZO has a bell-shape distribution of In_6 neighbors, Fig. 8, with 4 In_6 neighbors to be the most likely arrangement. Finally, the spatial distribution of InO_6 polyhedra in a-IGeO appears to be more uniform than that in a-IScO: the probability to find a In_6 cluster of any size (no or 1 to 8 neighbors) is nearly the same in a-IGeO, whereas presence of Sc results in the largest InO_6 cluster of 10 neighbors, Fig. 8. We must stress here that the role of oxygen-non-stoichiometry and deposition temperatures (or cooling

rates) on the structural properties of a-IXO was not taken into account in this work. Such investigations are ongoing and are expected to elaborate the effect of X addition.

3.5. XO connectivity and spatial distribution. At 20% fraction of X, the spatial distribution and connectivity of XO polyhedra are expected to play a more important role in charge scattering than the distribution of InO_6 polyhedra discussed above. In Fig.2, a tendency toward the X-O natural distances (i.e., those found in the crystalline binary counterparts) has been demonstrated. Here, the second and third shells, i.e., X-X distances and X-O-X angles, as well as the type of sharing between the connected XO polyhedra are analysed. First, we find that the number of shared XO polyhedra correlates with the X ionic radius: for X=Zn, Ga, Ge, or Sc with a small ionic radius, there are 12-14 connections per cell, whereas for X=Sn, Cd, Y, or La with a large ionic radius, the total number of connections increases to 20-24, Fig. 9. Furthermore, the average X-X distances and average X-O-X angles for the connected XO polyhedra in a-IXO resemble those found in the corresponding crystalline counterparts, Fig. 9.

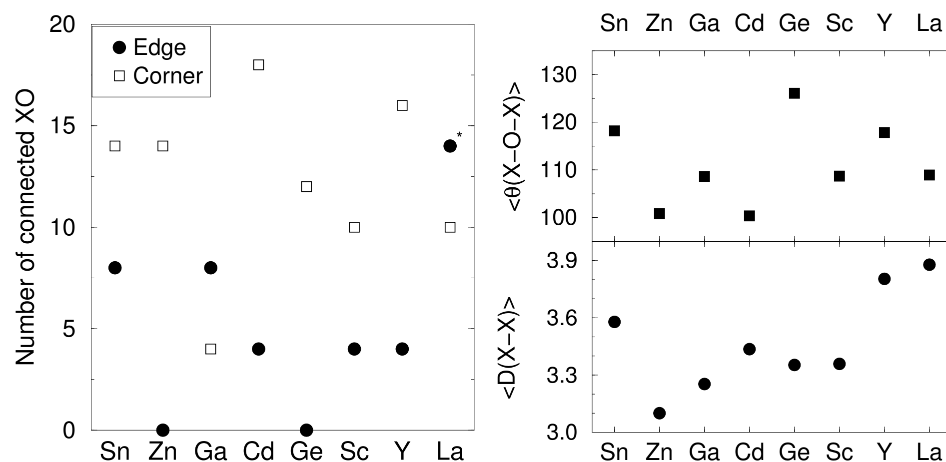

Figure 9. (Left) Number of edge-shared and corner-shared X-X pairs in amorphous IXO. (Right) Average X-X distance, in Å, and average X-O-X angle, in degrees, for the XO polyhedra connected via edge- and corner-sharing in IXO.

In addition to the expected cation size effect on the connectivity between XO polyhedra, we find that some X cations have a strong preference for either corner or edge sharing of the XO polyhedra. Specifically, no edge-shared Zn-Zn or Ge-Ge pairs are found

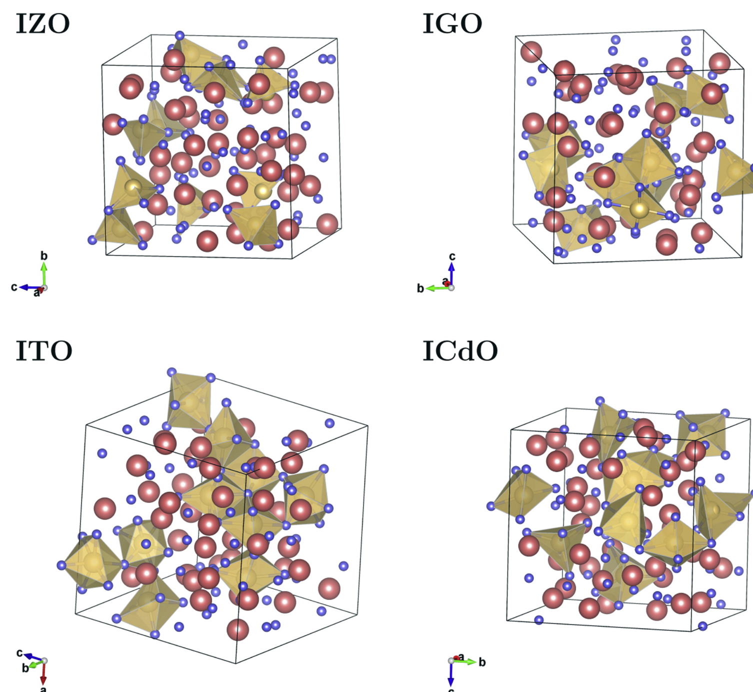

Figure 10. (Color online) Atomic structures of a-IXO, X=Zn, Ga, Sn, or Cd, highlighting the X-O bonds and XO polyhedra only. Small spheres represent oxygen atoms, and large spheres that are not connected with oxygen atoms represent In atoms.

in a-IZO and a-IGeO, in excellent agreement with crystalline binary (wurtzite ZnO and cristobalite GeO_2) as well as ternary (In_2ZnO_4 and $In_2Ge_2O_7$) oxides. On the other hand, Ga and La favor edge sharing so that the fractional number of the edge-shared Ga-Ga or La-La is significantly larger than that of corner-shared, Fig. 9. In a-ILaO, La also promotes face-sharing between LaO polyhedra (four La-La pairs were found to share three oxygen atoms) that is likely to be associated with La strong tendency toward over-coordination. In a-IGO, the strong preference for edge-sharing leads to the formation of GaO clusters, Fig. 10 – in marked contrast to a homogeneous distribution of ZnO and GeO polyhedra with a similar number of connected XO polyhedra in amorphous IZO, IGO and IGeO, Fig. 9. Similarly, a larger number of edge-shared Sn-Sn connections as compared to X=Cd, Fig. 9, signifies SnO polyhedra clustering: indeed, five SnO_6 polyhedra connected via edge-sharing with the rest of the SnO_6 polyhedra attached via corner-sharing are found in a-ITO,

Fig. 10. This finding may be explained by the Sn strong ability to attain full coordination with oxygen atoms as compared to In atoms that are more adaptable to distortions (this is opposite to Cd atoms that accept very low coordination with oxygen atoms, Fig. 3). Indeed, in the crystalline $In_4Sn_3O_{12}$, a fraction of Sn atoms form regular SnO_6 polyhedra, whereas all In atoms have a low symmetry coordination with the In-O distances ranging from 2.07 Å to 2.31 Å. Therefore, Sn addition may help to attain amorphous In-based oxide structure by distorting the InO polyhedra and, hence, preventing InO_6 clustering and the subsequent formation of In_2O_3 nanocrystallites. On the other hand, Sn has a strong tendency to cluster itself which ultimately limits the electron mobility as the fraction of Sn increases. Further investigations of the role of oxygen-non-stoichiometry and cooling rates on the spatial X distribution in amorphous In-based oxides are expected to shed additional light on the tunable properties of oxides and are in progress.

4. CONCLUSIONS

The results of ab-initio molecular-dynamics liquid-quench simulations for eight ternary In-based amorphous oxides, a-IXO with X=Sn, Zn, Ga, Cd, Ge, Sc, Y, or La, reveal that several factors, ranging from local (ionic size and metal-oxygen bond strength) to long-range (natural preference for connectivity between MO polyhedra), play an important role in the structural properties of a-IXO and result in a complex composition-dependent behavior.

The local structure of the MO polyhedra remains, on average, nearly unchanged upon the transition from crystalline to amorphous state. Moreover, the average In-O coordination is 5.0-5.2 in a-IO and all a-IXO considered in this work. Such a weak dependence of the In coordination on composition may signify that In atoms remain to serve as a main source of oxygen defects upon fractional substitution with X. However, charge transport in a-IXO is likely to be affected strongly by the composition-dependent distribution of the InO_6 and

XO polyhedra. Presence of X may result in a random distribution of the MO polyhedra or facilitate the formation of corner-shared chains or edge-shared clusters of the InO_6 and XO polyhedra that, in turn, will affect (i) the degree of amorphization of the In-based framework, and (ii) the carrier mobility controlled by scattering on large XO clusters or nanocrystalline inclusions. Preferred long-range distribution of MO polyhedra may also affect the mechanical properties of amorphous oxides.

Further investigations of the role of oxygen non-stoichiometry and deposition temperatures (or cooling rates) on the structural properties of a-IXO are expected to elaborate the effect of X addition on the carrier concentration and carrier transport.

5. ACKNOWLEGEMENTS

The work was performed under the collaborative MRSEC program at Northwestern University and supported by the National Science Foundation (NSF) grant DMR-1121262. Computational resources were provided by the NSF-supported XSEDE program, grant TG-DMR080007.

III. CATION SIZE EFFECTS ON THE ELECTRONIC AND STRUCTURAL PROPERTIES OF SOLUTION-PROCESSED IN-X-O THIN FILMS

Jeremy Smith[1], Li Zeng[1,2], Rabi Khanal[3], Katie Stallings[1], Antonio Facchetti[1,4], Julia E. Medvedeva[3], Michael J. Bedzyk[5], and Tobin J. Marks[1]

[1]*Department of Chemistry and Materials Research Center, Northwestern University, Evanston, IL, USA*

[2]*Graduate Program in Applied Physics, Northwestern University, Evanston, IL, USA*

[3]*Department of Physics, Missouri University of Science & Technology, Rolla, MO*

[4]*Polyera Corporation, Skokie, IL, USA*

[5]*Department of Materials Science and Engineering and Materials Research Center, Northwestern University, Evanston, IL, USA*

ABSTRACT*

The nature of charge transport and local structure are investigated in amorphous indium oxide-based thin films fabricated by spin-coating. The In-X-O series where X = Sc, Y, or La is investigated to understand the effects of varying both the X cation ionic radius (0.89-1.17 Å) and the film processing temperature (250-300 °C). Larger cations in particular are found to be very effective amorphosizers and enable the study of high mobility (up to 9.7 $cm^2V^{-1}s^{-1}$) amorphous oxide semiconductors without complex processing.

*Published in Advanced Electronic Materials **1**, 1500146 (2015).

Electron mobilities as a function of temperature and gate voltage are measured in thin-film transistors, while X-ray absorption spectroscopy and ab initio molecular dynamics simulations are used to probe local atomic structure. It is found that trap-limited conduction and percolation-type conduction mechanisms convincingly model transport for low- and high-temperature processed films, respectively. Increased cation size leads to increased broadening of the tail states (10-23 meV) and increased percolation barrier heights (24-55 meV) in the two cases. For the first time in the amorphous In-X-O system, such effects can be explained by local structural changes in the films, including decreased In-O and In-M (M = In, X) coordination numbers, increased bond length disorder, and changes in the polyhedra interconnectivity.

1. INTRODUCTION

In the past decade amorphous metal oxides (AMOs) have become attractive contenders as semiconducting and conducting materials for thin-film electronics [28, 39, 42, 153, 154]. There is a major driving force for applications based on optoelectronic device production using large-area, roll-to-roll processing methods enabled by mechanical flexibility and low-cost fabrication [155]. These include, but are by no means limited to, display backplanes, smart windows, solar cells, and radio-frequency identification tags. A combination of high carrier mobility, even in the amorphous state, excellent optical transparency, and the ability to process these thin-film materials from solution offers the potential of novel applications and a paradigm shift away from current technologies such as those based on amorphous silicon (a-Si). AMOs have recently achieved industrial prominence, with amorphous indium-gallium-zinc oxide (a-IGZO) for optical displays being a key example [156]. Typically, for both conducting and semiconducting electronic components, indium and/or zinc-based oxides are heavily doped with secondary cations such as Ga,[42] Y,[157] Cd,[158] or Sn.[159] These transition and post-transition metal ions with large spherical ns-orbitals ($n \geqslant 4$) provide the dispersive conduction band required for electron transport, even in the amorphous phase [22]. In general, the secondary metal cations also affect several important film properties such as the degree of crystallinity, the local lattice structure, the formation of defects, as well as the electronic structure.[49, 91, 160] Furthermore, such cations are almost always necessary to control the film charge carrier concentration and to disrupt the lattice crystallinity, thus generating the amorphous phase. Therefore, deeper understanding of the role of these cations will be necessary to design future oxide systems with tailored properties.

High-performance AMO films are typically grown by chemical vapor deposition, [161] physical vapor deposition such as sputtering and pulsed laser deposition, [42] or by atomic layer deposition [162]. In these cases, the resulting thin film transistors (TFTs)

have electron mobilities exceeding 10 $cm^2V^{-1}s^{-1}$ [82]. However, solution-based methods are attractive because of their roll-to-roll compatibility, reduced materials waste, and atmospheric pressure growth conditions. Additionally, it becomes possible to tune the oxide composition by simply changing the precursor solution composition in a straightforward and comprehensive fashion. Numerous oxide precursor routes have been developed, often based on sol-gel chemistry, [163] and generally high-temperature annealing steps (>400 °C) are required to remove impurities and achieve full oxide lattice condensation. Recently, several new methods have been reported that reduce processing temperatures [164, 165, 166, 167, 168, 169]. Here we employ the “combustion" synthesis approach as developed in this laboratory, [165] and previously applied to In_2O_3, In-Zn-O, In-Sn-O, In-Y-O, and In-X-Zn-O (X = Ga, Sc, Y, La) systems [149]. The precursor solution consists of an oxidizer in the form of the metal nitrate and a fuel (in this case acetylacetone), where, upon annealing at 250-300 °C, a rapid, highly exothermic and localized chemical reaction drives the formation of the metal oxide lattice/network, while not significantly increasing the film temperature. Combustion synthesis and other low-temperature routes allow complete conversion to the oxide in this temperature range but often result in device performance that varies with annealing temperature [164, 165, 166, 167, 168, 169].

The incorporation of secondary elements into the indium oxide lattice is expected to alter the local structure and lead to diminished long-range order. Furthermore, the composition dependence of the film crystallinity is predicted to differ for each added element due to the increased disorder induced by disparate cation sizes within the lattice. The chemical properties of Sc^{3+}, Y^{3+}, and La^{3+} are similar, namely a 3+ oxidation state, octahedral coordination of oxygen around the metal in M_2O_3, and comparable oxide lattice enthalpies; however, their ionic radii $R_{\text{ionic}}(\text{X})$ range from $0.95R_{\text{ionic}}(\text{In}^{3+})$ to $1.25R_{\text{ionic}}(\text{In}^{3+})$ [170]. The size of the cation, which is determined by its electron configuration, will therefore be the dominant variable in this particular series and is expected to result in changes to the oxide properties. Consequently, in this contribution, we focus on the In-X-O system, where

X = Sc, Y, La, with X concentrations varied between 2.5 and 12.5 at%, which crosses the crystalline-to-amorphous transition while maintaining complete oxide solid solution. We employ two processing temperatures, 250 and 300 °C, which for the In-X-O system, represent a “lower-quality" and “higher-quality” oxide film respectively, and which have noticeable differences in their structural and electronic properties.

The amorphous compositions are of particular interest from both a fundamental perspective and a technological one. Long-range order is absent, necessitating multiple relatively sophisticated techniques to elucidate structure-function relationships compared to crystalline semiconductors. X-ray absorption spectroscopy (XAS) analysis is one important method used to probe AMO materials on the ≈5 Å length scale and provides information on coordination number, average atomic separations, and atomic positional disorder of the different shells surrounding the central absorbing atom [54, 104]. The XAS methods employed here are outlined in Sections ‘X-Ray Absorption Spectroscopy’ and ‘Experimental Section’. Computational modeling methods, specifically ab initio molecular dynamics (MD) simulations of the amorphous In-X-O lattices, are also employed, and it will be seen that they confirm the experimental trends. Since grain boundary defects are also largely suppressed in AMO materials, which is a significant factor influencing their electronic and mechanical properties, high electron mobilities can be achieved even by expeditious solution-processing methods. For example, this report demonstrates amorphous In-La-O (La: 5 at%) with μFET = 9.7 cm^{2}V^{-1}s^{-1}. Furthermore, electron transport in In-X-O TFTs is characterized as a function of temperature in the range 150-300 K. It will be seen that these films exhibit thermally activated transport, and this can be associated with either trap-limited conduction for more disordered films, or percolation conduction for more ordered films (details of these models are provided in Section ‘Thin Film Transistor Charge Transport Models’). Activation energies as a function of the X cation size are used to extract tail state distributions as well as conduction band potential barriers, and therefore

provide a direct link between the electrical properties and the structural disorder induced by the secondary cation.

2. STRUCTURAL AND ELECTRONIC CHARACTERIZATION

2.1. X-Ray Absorption Spectroscopy. Due to large oxygen electronegativity, the structure of an amorphous oxide can be described as a network of MO_x polyhedra where distortions and the connectivity of the polyhedra govern the transport properties. Therefore, it is crucial to investigate these structural characteristics in detail. For amorphous samples, which lack long-range order, XAS is an ideal technique complement to X-ray diffraction (XRD). XAS can be divided into two parts: X-ray absorption near-edge structure (XANES) which is indicative of the chemical state and site symmetry, and extended X-ray absorption fine structure (EXAFS), which can be analyzed quantitatively to obtain local structural information. The normalized linear EXAFS absorption coefficient χ(k) can be fitted by Equation (3) [54]

$$\chi(k) = S_0^2 \sum_i \frac{N_i f_i(k)}{k R_i^2} \exp\left(\frac{-2\mathrm{R_i}}{\lambda(\mathrm{k})}\right) \exp(-2\mathrm{k}^2\sigma_{\mathrm{R_i}}^2) \sin\left(2\mathrm{kR_i} + \delta_\mathrm{i}(\mathrm{k})\right) \quad (3)$$

where S_0 is the intrinsic loss factor, λ(k) is the electron mean free path, N_i and R_i are the coordination number and bond distance of the ith shell of the absorbing atom, respectively, $f_i(k)$ and $\delta_i(k)$ are the backscattering amplitude and the phase shift, and $\exp(-2\mathrm{k}^2\sigma_{\mathrm{R_i}}^2)$ is the Debye-Waller factor-a measure of the structural disorder or the variation in R_i. The Fourier transformation of $\chi(k)$ generates a pseudo-radial distribution function (p-RDF) for the absorbing atom. For amorphous oxides we are interested in how the coordination number, bond distances, and the Debye-Waller factors change with processing temperature and choice of X cation.

2.2. Ab Initio Molecular Dynamics Simulation. The results of the EXAFS analysis can be compared to the local structure characteristics of amorphous oxides obtained

from ab initio molecular dynamics (MD) simulations. The total, M-O, and M-M radial distribution functions are readily available from the MD models of amorphous oxide structures. Furthermore, an accurate comparison of the local (first-shell) structural characteristics in amorphous indium oxide (a-InO) and In-X-O materials can be made based on the average pair correlation function (Equation (4)) [125, 126]

$$R_{\mathrm{av}} = \frac{\sum_i l_i \, exp\left(1 - (l_i/l_{\min})^6\right)}{\sum_i exp\left(1 - (l_i/l_{\min})^6\right)} \tag{4}$$

where l_i and $l_{\min}$ are individual metal-oxygen bond lengths and minimum bond length in the polyhedron, respectively. Using the pair correlation function Rav the effective coordination number N_{ECN} can be calculated for each polyhedron according to Equation (5)

$$N_{\mathrm{ECN}} = \sum_i \exp\left(1 - (\mathrm{l_i}/\mathrm{R_{av}})^6\right) \tag{5}$$

We stress here that the above equations are used only to obtain the In-O and X-O first shell information; the wide distribution of the second-shell In-In and In-X distances makes the exponential fit in the R_{av} and N_{ECN} calculations inapplicable and a running coordination number N_{RCN} is used instead. It is possible, however, to distinguish between the second and third shells using the optimized atomic coordinates of the MD simulated structures. For every In atom, the number of M (In or X) neighbors that share one, two, or three oxygen atoms with the central In can be determined, giving the average coordination number for corner, edge, or face-shared In-M, respectively. Then, the pair distribution functions, average distances, and statistical spreads can be found for edge- and corner-shared In-In pairs separately [147].

Once a satisfactory agreement between the EXAFS and MD results for the structural properties as a function of cation size is obtained, the electronic structure of amorphous In-X-O materials is calculated. The ab initio nature of the MD simulations (density-functional

equations are solved at every step during the MD quench) allows us to accurately describe the electronic states, defects, and the orbital character of all cations ($5s^0$ for In vs $(n-1)d^0ns^0$ for Sc, Y, or La) even during the quench. As such, our ab initio MD approach differs from a classical MD simulation, commonly employed to obtain amorphous oxide structures: the classical approach cannot describe the electronic localization and defects.

To analyze the localized states in the band gap and near the band edges, the inverse participation ratio (IPR) of an orbital $\psi_n(\vec{r}_i)$ can be found from ab initio density-functional calculations according to Equation (6), where N is the number of volume elements in the cell and i is the index of the volume element

$$\mathrm{IPR}(\psi_\mathrm{n}) = \mathrm{N}\frac{\sum_\mathrm{i}^\mathrm{N} |\psi_\mathrm{n}(\vec{r}_\mathrm{i})|^4}{\left|\sum_\mathrm{i}^\mathrm{N} |\psi_\mathrm{n}(\vec{r}_\mathrm{i})|^2\right|^2} \tag{6}$$

2.3. Thin Film Transistor Charge Transport Models. Charge transport in AMO semiconductors has been widely studied, both by TFT and Hall effect measurements. In general, amorphous semiconductors possess tail states that extend into the band gap close to the conduction band edge as a result of energetic disorder, as well as lower energy states arising from a variety of defects [154]. For example, in metal oxides there is evidence for subgap states [85, 171], which can result in effects such as persistent photoconductivity [172] and bias instability [173]. The AMO density of tail states is usually much less than that of amorphous silicon due to the more isotropic nature of the s-orbital derived conduction band. Additionally, it has been found that carriers can percolate between potential barriers at the conduction band edge. Generally, there exists the possibility for charge transport by Mott variable range hopping (VRH) through localized states [154], as well as transport by carriers in extended states above the mobility edge E_m, either by trap limited conduction (TLC) or percolation conduction (PC) [174, 175]. VRH gives rise to a characteristic $1/T^{1/4}$ mobility relationship while TLC models can be described by a simple Boltzmann expression

(1/T). The Kamiya-Nomura [176] PC model based on work by Adler et al. [177] assumes a Gaussian distribution of potential barriers attributed to the secondary cation; in the present case X, for the In-X-O system. This model ignores VRH because there is no evidence for the Hall voltage sign anomaly in AMO semiconductors but reproduces the apparent $1/T^{1/4}$ behavior at low temperature. Note, however, that Germs *et al.* argue that this is in fact a result of tail state VRH combined with band transport rather than PC [178].

For n-type TFT operation the Fermi level E_F moves toward the conduction band edge as the gate voltage V_G is increased to more positive values. The ratio of free (n_f) to trapped (n_{tr}) charge carriers is, therefore, a function of V_G as well as temperature and the density of tail states. For most amorphous semiconductors, a linearly increasing V_T is observed with decreasing temperature as carriers are thermally generated from localized states, which in the case of a-IGZO has been shown to be ionization of oxygen vacancies [91]. It is also well known that as the gate field is increased, E_F moves toward the mobility edge E_m and reaches the tail states at around V_G -V_T = 0. The percolation voltage V_p is then defined as the point at which carriers can begin to move through extended states ($E_F \approx E_m$); however, the exact transition from TLC to PC dominated conduction is not abrupt. At higher voltages still, band transport may be feasible and the mobility becomes temperature independent. In this study, the focus is on relatively high-temperature measurements ($300 \geqslant \mathrm{T} \geqslant 150$ K) and effective mobilities μ_{EFF} are extracted in the linear regime ($V_D << V_G$) for $V_G > V_T$. Therefore, a combination of TLC and PC models can be applied while assuming negligible VRH in this regime. The mobilities in each of these limits are given by Equations (7) and (8), respectively,

$$\mu_{\mathrm{TLC}} = \quad \mu_0 A^* \left[\frac{C_i(V_G - V_T)}{qN_{tr}^0}\right]^{\frac{T_0}{T}-1} \tag{7}$$

$$\mu_{\mathrm{PC}} = \quad \mu_0 \exp\left(-\frac{\mathrm{q}\varphi_{\mathrm{B}}}{\mathrm{kT}} + \frac{(\mathrm{q}\sigma_{\mathrm{B}})^2}{2(\mathrm{kT})^2}\right) \mathrm{B}^*(\mathrm{V_G} - \mathrm{V_P})^{\alpha} \tag{8}$$

where μ_0 is the band mobility, A* and B* are constants that depend on the density of conduction band states, C_i is the dielectric geometric capacitance, N_{tr}^0 is the areal density of tail states, kT_0 is the width of the tail state distribution, φ_B is the percolation barrier height, σ_B is the variation in φ_B assuming a Gaussian distribution of barriers, and α is related to the spatial coherence ratio of the barriers. The constant α depends on the spatial barrier width W_B and separation D_B and is given by $\alpha = 4(D_B - W_B)/D_B$. In both of these limiting cases, an activation energy E_A can be extracted from the slope of the Arrhenius plot and is given by Equation (9)

$$E_A(V_G) = -k\frac{\partial ln(\mu)}{\partial(1/T)} = \begin{cases} kT_0 ln\left(\frac{qN_{tr}^0}{C_i}\right) - kT_0 ln(V_G - V_T) & \text{for TLC} \\ q\varphi_B - \frac{(q\sigma_B)^2}{kT} & \text{for TC} \end{cases} \tag{9}$$

As can be seen here, the activation energy will be independent of V_G for the PC case, and be inversely related for the TLC case. Therefore by analyzing E_A as a function of ln(V_G -V_T) as well as μ as a function of (V_G -$V_{T,p}$), the relative importance of TLC versus PC can be estimated, and the relevant physical parameters, N_{tr}, kT_0, and qφ_B can be extracted.

3. RESULTS AND DISCUSSION

The processing temperature T_a and the choice of X cation have a strong influence on the degree of crystallinity χ_c of the final oxide film as shown in Figure 1. In the case of X = Sc at T_a = 300 °C all films are crystalline as estimated from the XRD peak areas (χ_c > 0.90). Note that moving to larger cations drastically reduces the crystallinity with In-Y-O showing a transition to the amorphous phase between 5 and 7.5 at% Y and In-La-O between 2.5 and 5 at% La. At T_a = 250 °C, most compositions are amorphous with the exception of 2.5 at% Sc which has a crystallinity of around χ_c = 0.15. Some films, for both processing temperatures, exhibit partial crystallinity (χ_c < 0.15) in the vicinity of the transition composition. As a control sample, an In_2O_3 film processed at T_a = 450 °C

had a crystallinity of χ_c > 0.98. Despite differences in crystallinity, there is no significant difference in r.m.s surface roughness between these films as measured by AFM, which is found to be on average ≈0.17 nm. This demonstrates that: (i) differences in back surface roughness will not affect our electrical measurements, and (ii) even when crystalline, these films do no exhibit large grains or prominent grain boundaries.

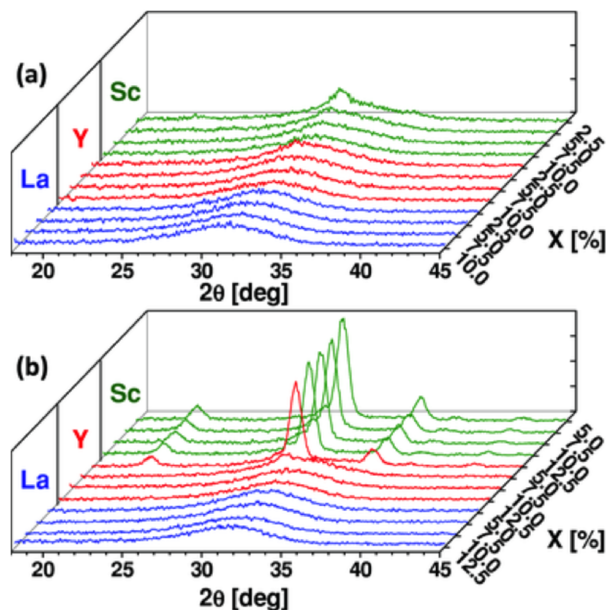

Figure 1. Grazing incidence XRD scans for In-X-O thin films processed at a) T_a = 250 °C and b) T_a = 300 °C. Film compositions are given as at% of the secondary cation, X (X = Sc, Y, La). Peak positions for the crystalline samples are at $2\theta = 21.7^o$, 30.8^o, 35.7^o and are consistent with the In_2O_3 bixbyite structure. The broad amorphous peak is centered at $2\theta = 29\text{-}33^o$.

In accord with the observed reduction in crystallinity with the X ionic size, ab initio MD simulations of amorphous In-X-O reveal that the number of InO_6 polyhedra varies with X: it is largest for X = Sc and notably smaller for X = Y or La (Figure 2). Moreover, in In-Sc-O the InO_6 polyhedra are mostly connected via edge sharing, resulting in the formation of large InO_6 clusters. The appearance of such clusters signifies the nucleation of In_2O_3 nanocrystallites, as was observed for a-InO [147]. In marked contrast to In-Sc-O, the InO_6 polyhedra in amorphous In-Y-O and In-La-O are distributed uniformly throughout the cell with a few polyhedra connected via edge- or corner sharing. This highlights the

effectiveness of the larger cations such as Y or La in achieving amorphous In-based oxide structures.

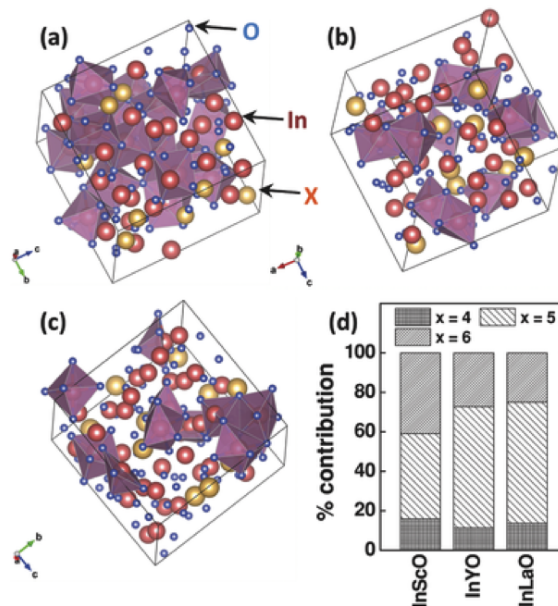

Figure 2. Representative structures of a) In-Sc-O, b) In-Y-O, and c) In-La-O from ab initio MD simulation. In each case, 20% of the In atoms are replaced with the secondary cation, X. InO_6 polyhedra are indicated on the structures in purple with In represented as red spheres, X as yellow spheres, and O as blue spheres. The proportion of InO_x polyhedra with x = 4, 5, and 6 are shown in d).

The TFT properties at room temperature for all compositions and processing temperatures are shown in Figure 3 and typical transfer and output curves are plotted in the Ref [179]. We will first distinguish between compositions that are measured to be amorphous by XRD ($\chi_c = 0$) and those that are crystalline or partially crystalline ($\chi_c > 0$). For $\chi_c = 0$, the maximum electron mobilities are measured to be 9.7 and 5.1 $cm^2V^{-1}s^{-1}$ for $T_a = 300$ and 250 °C, respectively, and are obtained in the In-La-O system. It is important to note that the use of X = La provides the highest performance amorphous films, since the large cation can be introduced into the system at relatively low concentrations, thus minimizing impurity scattering while still realizing the amorphous state. This approach, therefore, provides a useful strategy to readily introduce amorphous character into otherwise easily crystallizable materials. However, it should be noted that when considering all films, for

a fixed X concentration, the general trend is that mobility decreases with increasing cation size similar to the previously reported In-X-Zn-O system [149]. The crystalline ($\chi_c > 0.7$) and partially crystalline ($0 < \chi_c < 0.15$) samples typically exhibit good TFT characteristics (μ = 1-10 cm^{2}V^{-1}s^{-1}), however, tend to be slightly more inconsistent in their device parameters, often having negative (and less controllable) threshold voltages, and more variability between devices in subthreshold behavior, especially in cases of low X content. This result highlights the fact that although In-Y-O and In-Sc-O may have higher electron mobilities than In-La-O for a given X concentration, their increased propensity to crystallize can, especially in this case, be disadvantageous, and motivates the more detailed study of the electrical and local structure properties presented herein.

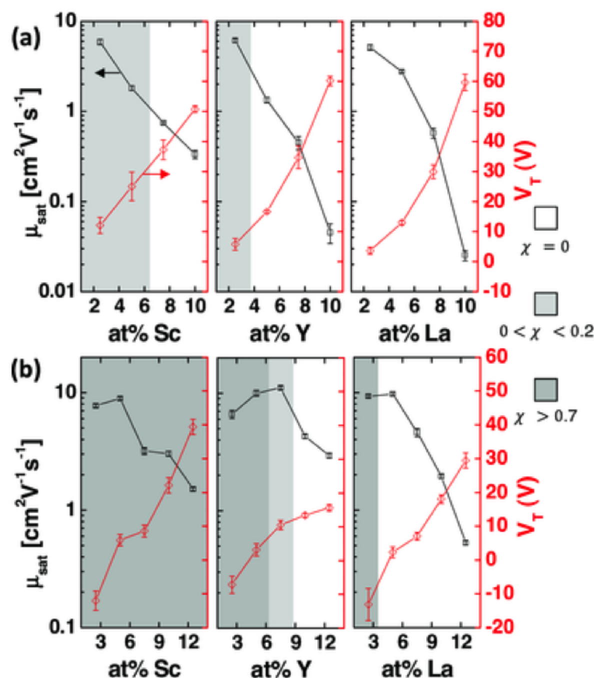

Figure 3. Thin film transistor data for measurements at room temperature taken in saturation to extract values of μ_{sat} and V_T. Regions corresponding to crystalline, semicrystalline, and amorphous films are indicated for films processed at a) T_a = 250 °C and b) T_a = 300 °C. Optimal devices characteristics are around 5 and 10 at% doping for the low and high-temperature processed films, respectively.

For all In-X-O films, increasing X concentration lowers μ and increases V_T. Especially at T_a = 250 °C, this effect is decidedly detrimental for X concentrations above 7.5 at% since significant charge is trapped within localized states arising from the structural disorder. To further quantify the effects of this disorder, as well as that of the cation size, on the electron transport within the film, TFT parameters were measured as a function of temperature in the range $300 \geqslant T \geqslant 150$ K. Samples with 10 at% X at T_a = 300 °C and 5 at% X at T_a = 250 °C were chosen to provide optimal device operation and encompass a range of structural differences (see the Ref. [179] for TFT characteristics). Typical Arrhenius plots for the In-La-O films are shown in Figure 4a, c. Linear fits at various values of V_G-V_T yield the activation energies plotted in Figure 4b, d. There is a significant difference between films with 250 and 300 °C processing temperatures T_a. The former appear to be dominated by a TLC mechanism, whereas the latter have a much weaker dependence of the activation energy on the gate voltage, thus implying a PC dominated mechanism (Equation (9). In all cases, there is no strong dependence of E_A on temperature, suggesting that the barrier height distribution σ_B is very small. This is reasonable considering that these films only have two distinct cations unlike more complex oxides such as a-IGZO. From the present data, it is, therefore, possible to extract both tail state distributions (N_{tr}^0 and kT_0) from the T_a = 250 °C films, and the approximate percolation barrier heights ($q\varphi_B$) from the T_a = 300 °C films; these parameters are summarized in Table 1. Note that kT_0 is comparable to kT and therefore a purely TLC model is not appropriate. However, the advantage of the activation energy analysis is that the effects of TLC and PC can be separated by their V_G dependence, and therefore an estimate of kT_0 can be made even for small values. For larger R_{ionic}(X), increased structural disorder broadens the tail state distribution while the overall areal density of trap states at E_m remains approximately constant. The DFT-calculated inverse participation ratios (IPR) for the MD-simulated nonstoichiometric amorphous In-X-O structures illustrate the existence of localized states within the band gap and near the band edges. These results support the broadening of the localized state distribution with

the ionic size: a significant contribution from the localized states is found below, below and at, or below and above the Fermi level for X = Sc, Y, or La, respectively (full IPR data can be found in the Ref. [179]).

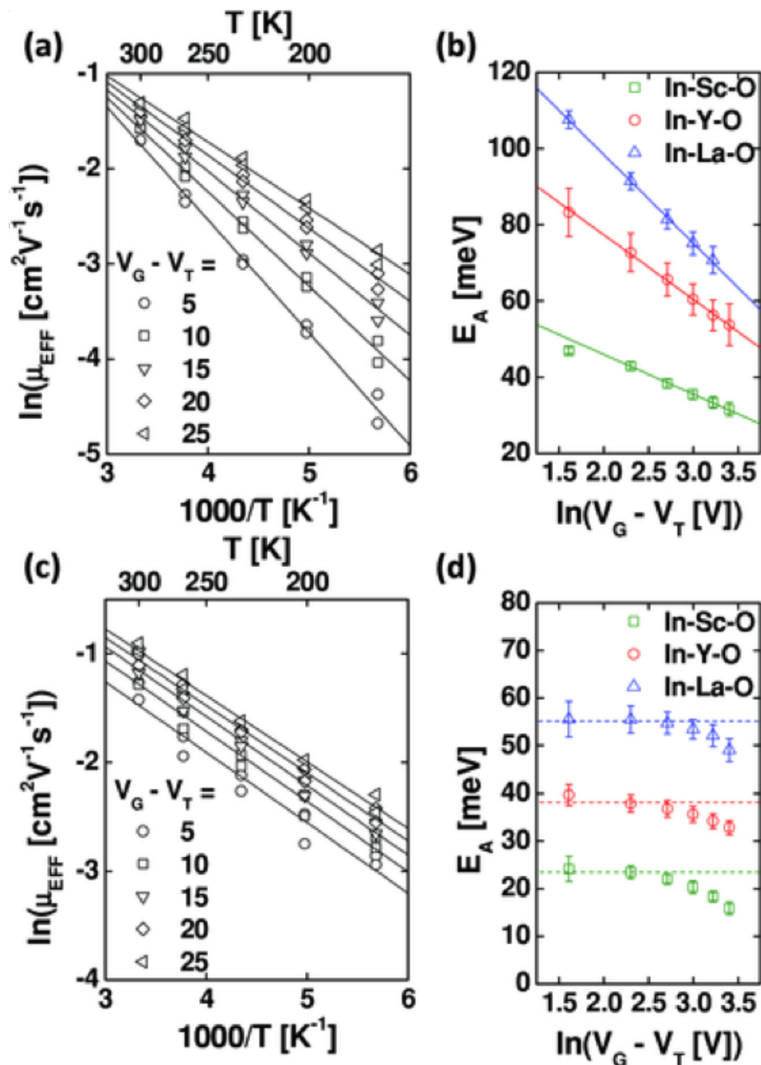

Figure 4. Temperature-dependent field-effect electron mobility showing linear fits for the extraction of the activation energy, E_A. Effective linear mobility is plotted for values of V_G -V_T between 5 and 25 V for the In-La-O case with a) T_a = 250 °C and c) T_a = 300 °C. The extracted values of E_A are plotted as a function of ln(V_G -V_T) for each film and at processing temperatures of b) T_a = 250 °C and d) T_a = 300 °C. Linear fits are made to the T_a = 250 °C data while the lines through the T_a = 300 °C data are guides to the eye.

For the more structurally ordered films that show percolation behavior, φ_B also increases with increasing R_{ionic}(X). It has been suggested previously [174] that percolation

Table 1. Model fit parameters for the TFT measurements calculated from Equation (9)

	T_a[°C]	kT$_0$[meV]	N^0[cm^{-2}]	qφ_B[meV]	Dominant mechanism[a)]
In-Sc-O	250	10	$\approx 4 \times 10^{13}$	-	TLC
In-Y-O	250	17	$\approx 4 \times 10^{13}$	-	TLC
In-La-O	250	23	$\approx 4 \times 10^{13}$	-	TLC
In-Sc-O	300	-	$\approx 4 \times 10^{13}$	24	PC
In-Y-O	300	-	$\approx 4 \times 10^{13}$	38	PC
In-La-O	300	-	$\approx 4 \times 10^{13}$	55	PC

[a)]Mechanisms: TLC=trap-limited conduction; PC=percolation conduction.

can arise due to secondary cations perturbing the conduction band, which is primarily derived from the In s-states. Here, we are able to show, for the first time, a direct relationship between the measured potential barrier and the radius of the secondary cation, thus supporting this model. Values of the spatial coherence ratio for the potential barriers $(D_B - W_B)/D_B$ are also extracted from the V_G dependence of the mobility (Figure 5a) and vary from 0.04 to 0.32, with the largest ratio observed in In-Y-O. Furthermore, a trend in the spatial distribution of XO_x polyhedra within the amorphous cell is clearly observed in the results of the MD simulations (Figure 5b). In the In-Sc-O series, the ScO_x polyhedra are connected primarily via corner sharing; several ScO_x polyhedra stand separate from each other, i.e., remain disconnected. In In-Y-O, the number of corner-shared YO_x polyhedra increases substantially, leading to the formation of long chains spread over the cell-in agreement with the observed largest spatial coherence ratio. In In-La-O, the large ionic radius of La as well as its tendency for over-coordination leads to formation of clusters of LaO_x polyhedra more than half of which are connected via edge- or even face-sharing. Such LaO_x clustering may be connected with the observed large potential barrier in amorphous In-La-O and the resulting TFT mobility decrease for larger La contents. At the same time, the observed spatial coherence ratios have some dependence on temperature suggesting that a purely PC model is inadequate for these materials, which is consistent with the deviation of E_A from a constant in Figure 4d. While alternatives to PC descriptions have been

proposed,[178] additional studies will be required before the current models for charge transport in amorphous metal oxide TFTs can be refined.

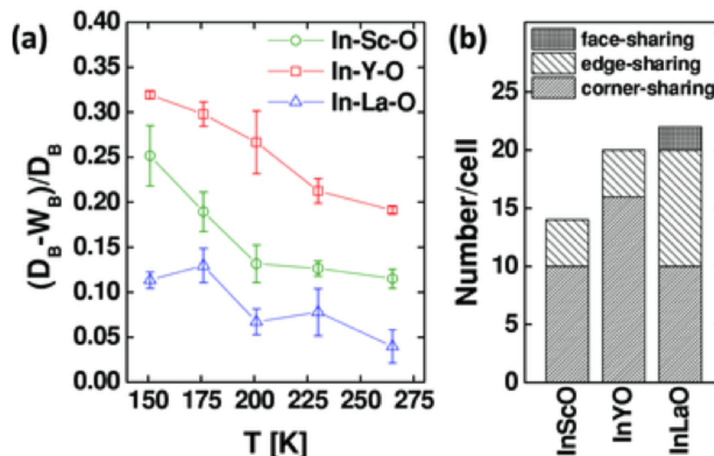

Figure 5. a) Values of the spatial coherence ratio calculated by fitting Equation (8) to the gate voltage dependence of the In-X-O electron mobility at temperatures between 150 and 275 K. b) Sharing statistics for XO_x polyhedra as calculated from MD simulations of the structures. Numbers of corner-, edge-, and face-sharing polyhedra are shown per computational cell.

From the present TFT transport data, it is clear that two variables are especially important in these solution-processed In-X-O films: (i) the processing temperature, which strongly affects the charge transport mechanism; and (ii) the identity of the secondary cation, which influences both the tail state distribution and the percolation barriers. XAS is used here to further elucidate the nature of the structural disorder as seen in the electrical characterization.

Film XANES data at the In, Sc, Y, and La edges align well with their powder references (see the Ref. [179]). Combined with the XPS peak positions, all metal ions maintain the 3+ oxidation state in the films after the combustion process. A more quantitative analysis from the EXAFS region provides the coordination number N_i and Debye-Waller coefficient $\sigma^2_{R_i}$ for the first In-O shell and the first In-M shell (M = In or X), as shown in Figure 6, and the fitting results presented in Table 2. For all films, the calculated radii R_i are relatively constant at 2.16 Å for the In-O shell and 3.36 Å for the In-M shell, which are comparable to the radii for crystalline In_2O_3 reference powder samples. The

reductions in peak intensities in the p-RDF, especially for shells beyond the first In-M, correspond to a decrease in the coordination number and increased Debye-Waller factor in

Table 2. EXAFS fitting parameters for the first In-O and In-M (M = In or X) shells calculated using Equation (3)

	T_a[°C]	N_i		R_i[Å]		$\sigma^2_{R_i}$[10^{-3}Å^2]	
		In-O	In-M	In-O	In-M	In-O	In-M
In-Sc-O	250	5.62	3.04	2.152	3.358	6.45	7.02
In-Y-O	250	5.45	2.20	2.151	3.316	7.45	8.13
In-La-O	250	5.11	2.4[a)]	2.156	3.340	7.10	9[a)]
In-Sc-O	300	5.95	4.21	2.166	3.363	6.29	4.46
In-Y-O	300	5.75	3.62	2.155	3.365	6.96	7.46
In-La-O	300	5.56	3.32	2.147	3.368	7.69	13.5

[a)]Shells beyond the first have very low intensity (approaching EXAFS-free amorphous); therefore, the coordination number and Debye-Waller factor for the second shell cannot be uniquely fitted.

these shells, which are commonly seen as films become semicrystalline or amorphous. As the size of the secondary cation, X, increases N_i decreases, whereas $\sigma^2_{R_i}$ increases. This effect is much more pronounced for the In-M shell, suggesting that InO_x polyhedra remain relatively intact in the amorphous structure while disorder arises from distortions to the polyhedra network, i.e., to their interconnectivity. When comparing films annealed at 250 and 300 °C, the lower processing temperature leads to a greater drop in In-M coordination number-between 2.1 and 3.0 at T_a = 250 °C versus 3.3 and 4.2 at T_a = 300 °C. We can thus conclude that the introduction of larger secondary cations and/or lowering the processing temperature increases the amorphous network disorder, moving further away from the crystalline structure. In particular for the most amorphous samples, the “EXAFS-free" case is approached where all shells beyond the first In-O have very low intensities. This renders extraction of a unique In-M coordination number and Debye-Waller coefficient impossible in the In-La-O case with T_a = 250 °C. Note that the effect of the 50 °C change in Ta is greater than moving from X = Sc to X = La. This may partially explain the different transport mechanisms (PC and TLC) observed in the transistor measurements.

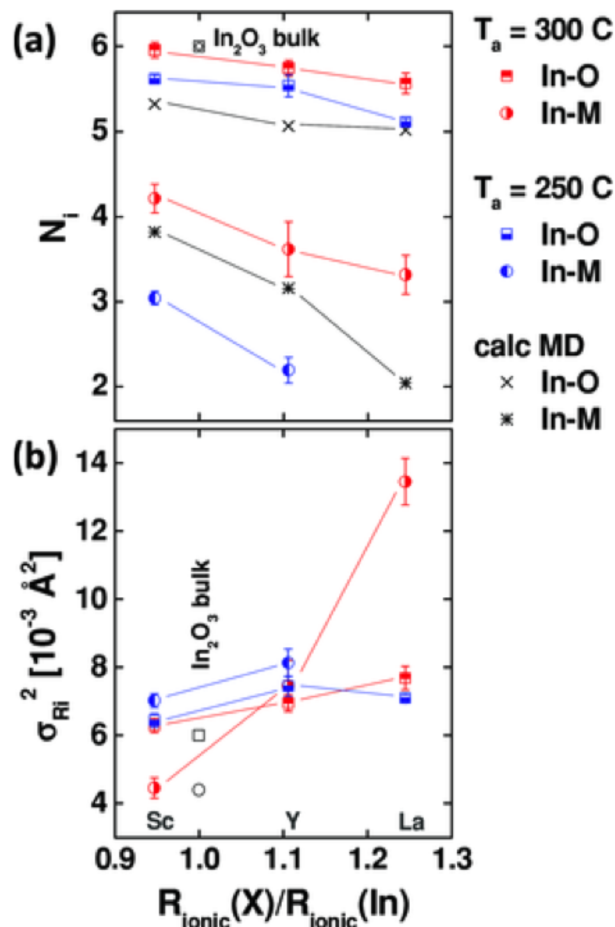

Figure 6. Fitting parameters from the In-X-O EXAFS measurements and ab initio MD simulations plotted as a function of the ionic radius of the X cation normalized to the radius of In^{3+}. a) The change in coordination number, N, for both the In-O and In-M (M = In or X) shells. b) The same for the change in Debye-Waller factor coefficient, $\sigma^2_{R_i}$.

The ab initio MD simulations for the In-X-O systems support the coordination number and bond length variations seen in the EXAFS experiments. For the first In-O or X-O shell, the calculated effective coordination numbers N_{ECN}s and bond lengths R_{av}s are summarized in Table 3. These values are in agreement with EXAFS showing: (i) a slight contraction in the In-O coordination number as the X cation size is increased and (ii) nearly invariant In-O bond lengths. For comparison, the average In-O distance and In-O coordination number in a-InO obtained from MD simulations are 2.16 Å and 5.0,

respectively. Although the In-O local structure characteristics show little sensitivity to the X cation size, the N_{ECN} and R_{av} values for X-O vary significantly among X, as expected from the strong X-O bonds. The average X-O distances in amorphous In-X-O nearly match the corresponding natural X-O distances, i.e., those found in the respective crystalline X_2O_3 materials. The average effective coordination N_{ECN} increases as the cation size increases, with Sc and La being under- and over-coordinated with O atoms, respectively, whereas the Y atoms retain the natural coordination number of 6.

Table 3. Structural characteristics of the first In-O and X-O shell as obtained from the ab initio MD simulations. The average coordination N_{ECN} and average distance R_{av} parameters were calculated according to Equations (4) and (5).

	N_{ECN}(In-O)	R_{av}(In-O)[Å]	N_{ECN}(X-O)	R_{av}(X-O)[Å]
In-Sc-O	5.32	2.158	5.23	2.068
In-Y-O	5.06	2.142	6.01	2.273
In-La-O	5.02	2.154	6.56	2.451

As noted in Section 'Ab Initio Molecular Dynamics Simulation', Equations (4) and (5) are not applicable for the second shell and beyond owing to broad In-M distance distributions. Instead, the total In-M coordination or a running coordination number N_{RCN} is calculated as a function of the radial distance r from an In atom. The N_{RCN} values for both In-O and In-M shells, Figure 7a,b, respectively, decrease with increasing cation size, but the effect is far more pronounced for the In-M shell. At r = 3.35 Å , which corresponds to the edge-shared In-In distance in crystalline In_2O_3, N_{RCN}(In-M) decreases from 3.82 Å to 3.16 Å to 2.05 Å for Sc to Y to La, respectively. In a-InO, the calculated N_{RCN}(In-In) is 2.69. Accordingly, the average distance between In and X connected via edge-sharing (second shell) increases with X ionic size: from 3.08 to 3.36 Å to 3.52 Å for In-Sc to In-Y to In-La, respectively. For comparison, the average edge-shared In-In distances are less affected, increasing from 3.26 to 3.31 Å for Sc and Y to La, respectively. Although it is impossible to directly compare these numbers to the experimental EXAFS data, which are derived from solution-processed films rather than a melt-and-quench simulation, it is

evident that these numbers correlate well with those in Figure 6 and follow the same trend. The increased second shell (In-M) bond distances can contribute to a larger effective mass; however, the spatial distribution and interconnection of the InO_x and XO_x polyhedra are expected to play the key role in determining the electron mobility in these amorphous oxides.

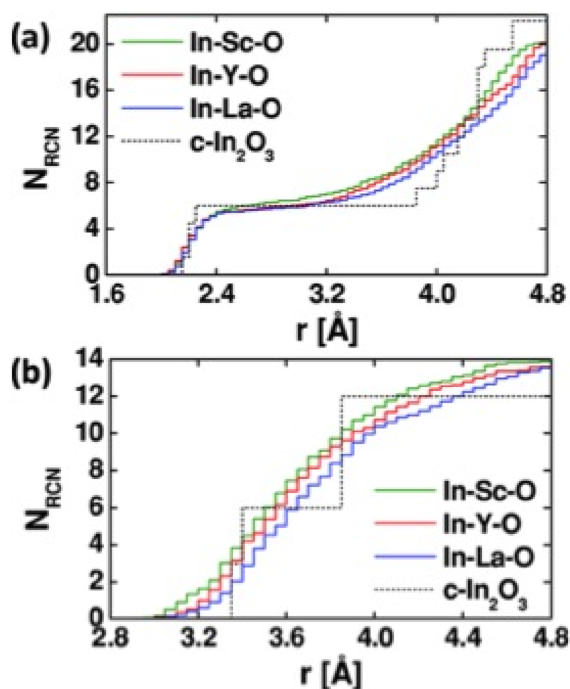

Figure 7. Ab initio MD simulation results for the In-X-O systems showing the calculated running coordination number, N_{RCN}. The radius r is the distance from the central In atom with a) showing the In-O coordination and b) showing the In-M coordination (where M = In or X). Crystalline In_2O_3 values are also shown for reference.

In addition to local disorder, the strength and type of M-O bonding have been shown to be good indicators of electron transport properties since weakly bound oxygen or oxygen not fully coordinated by a metal ion can introduce trap states and reduce the mobility and bias-stress stability in TFTs [180]. Previous work in this laboratory on oxygen “getter" effects in In-X-Zn-O materials suggests this may also be relevant to the In-X-O system [149]. XPS measurements were therefore carried out, focusing on the O1s peak, deconvoluting it into a M-O-M peak, a M-O(H) peak, and a weakly bound M-O-R surface

peak (Figure 8 a,b). The ratio of M-O-M peak area to total peak area η_{M-O-M} is shown in Figure 8c and represents the fraction of oxygen in the film that is completely incorporated into the metal oxide lattice. Additionally, using the ratio of O1s peaks to the In 3d, Sc 2p, Y 3d, or La 3d peaks allows estimation of the In-X-O film stoichiometry, which indicates that the oxide films preserve the precursor solution stoichiometry. All films, independent of the processing temperature or composition, are found to be close to stoichiometric (60 at% O). However, it is evident that η_{M-O-M} is a function of the processing temperature. For the T_a = 300 °C case, the oxide is well formed and η_{M-O-M} is relatively unaffected by the secondary cation since the thermal energy at this processing temperature allows good relaxation of the oxide lattice. However, η_{M-O-M} is lower for all compositions processed at T_a = 250 °C, suggesting that the oxide film is more defective, leading to the change from charge transport being limited by percolation in the conduction band to trapping and detrapping from tail states. Additionally, the larger cations tend to reduce η_{M-O-M} further, unlike in the high-temperature case, which is consistent with the broadening of the density of tail states at T_a = 250 °C when changing from Sc to Y to La.

4. CONCLUSION

The incorporation of the Group 3/4f cations Sc, Y, and La into indium oxide thin films by straightforward solution-processing techniques at low temperatures provides important information about the structural and electronic properties of amorphous oxide semiconductors. First and importantly, to facilitate the study of these systems, note that these elements can be introduced without the need for complex processing equipment and over a wide compositional range. It is found that large values of the X ionic radius $R_{ionic}(X)$ compared to indium, such as when X = La, can induce the amorphous state even at relatively low X concentrations, resulting in thin films with high electron mobilities. The effect of the cation size and processing temperature on the electron transport mechanism was also

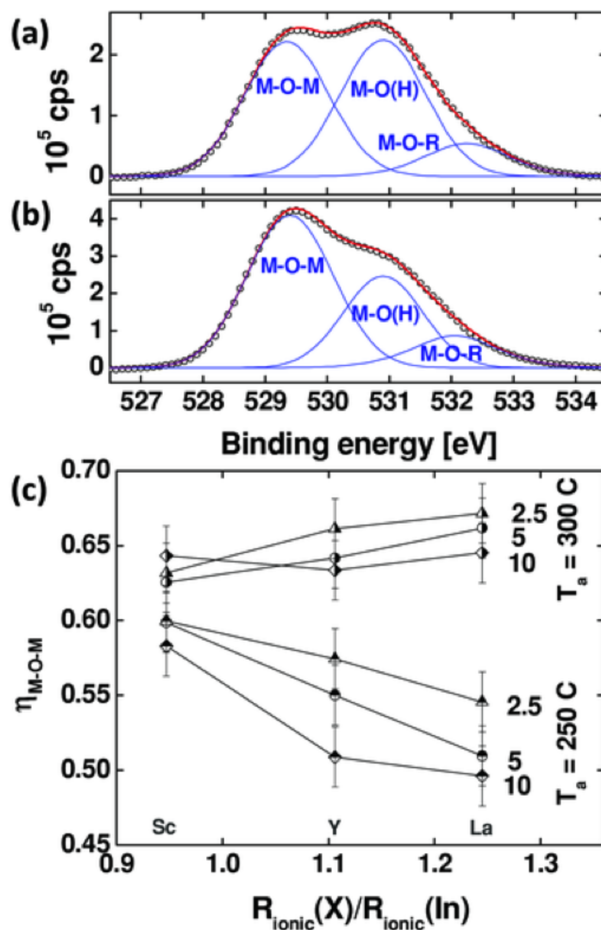

Figure 8. Fitting of the O1s XPS peaks for a 10 at% In-La-O film processed at a) T_a = 250 °C and b) T_a = 300 °C. Peak positions were fixed and correspond to fully bound oxygen (M-O-M), partially bound oxygen (M-O(H)) and weakly bound oxygen at the surface or organic impurities (M-O-R). c) The ratio of M-O-M peak area to total area, η_{M-O-M}, is plotted as a function of the X cation size for compositions of 2.5, 5, and 10 at%.

investigated here, and found to be dominated by trap-limited conduction (TLC) at low processing temperatures. This contrasts markedly with the high-temperature processed films, where activation energies for transport are much lower and independent of TFT gate voltages, suggesting transport dominated by electrons above the conduction band edge-in this case the conduction can be modeled using the typical Kamiya-Nomura percolation expression. It is observed in the TLC case that the tail state trap distribution broadens as the ionic radius of X increases for a fixed X concentration. In the percolation case, it is found

that larger ionic radii increase the potential barrier height, suggesting that disruptions to the indium oxide lattice by the introduction of the secondary cation X are the cause of such barriers. To understand the origin of this phenomenon, the local structure and valence of the oxide films were investigated using XAS and XPS and also compared to ab initio molecular dynamics simulations of the In-X-O system. A decrease in In-O and In-M coordination numbers is observed as the X cation size increases from that of In^{3+}. The fall in coordination number from the ideal crystalline value of 6 is especially apparent for the first In-M shell and for larger cation sizes (i.e., X = La). This result is concurrent with an increase in the variation of In-O and In-M shell bond distance, although the average distances remain constant. The interconnectivity of the MO_x polyhedra and structural disorder are therefore determined to be the main origins of the tail state width and percolation barrier height changes, and demonstrates that local structure measurements are vital to understanding charge transport in amorphous oxide electronics.

5. EXPERIMENTAL SECTION

Oxide Precursor Solutions: Solutions were prepared by dissolving $M(NO_3)_3$ in 2-methoxyethanol (M = In, Sc, Y, or La, 0.05 mol L^{-1}, 10 mL) and adding acetylacetone (32 μL) and $NH_{3(aq)}$ (30 μL). Solutions were stirred for 16 h before mixing in the desired ratios. The solutions were then filtered through a 0.2 μm Teflon filter, spin-coated at 3500 s^{-1} for 30 s and annealed at 250 or 300 °C (T_a) in air for 15 min yielding ≈5 nm thick oxide films. Repeated spin-coating and annealing was used to build up thicker films. This gave more dense oxide films than a single thick layer due to porosity caused by gas evolution during solution processing. The chosen thickness gave us optimal device performance. Hotplate surface temperatures were controlled to ±2 °C and only very small changes in substrate temperature were seen during film combustion. Changes in local temperature within the film during growth were extremely difficult to quantify accurately but were common to

all solution-processing techniques. Generally in these films, heat energy generated from chemical reactions will either be consumed driving lattice/network formation or will be dissipated relatively rapidly due to the large surface area-to-volume ratio. T_a therefore defines the technologically relevant thermal budget for the process. Films for TFTs were fabricated on heavily doped silicon wafers with 300 nm of thermal oxide (four repeated layers of combustion oxide, film thickness ≈15 nm). Films for grazing incidence XRD studies were fabricated on silicon wafers (four layers), and films for XAS were fabricated on fused-quartz substrates (11 layers, X: 10 at%). A postanneal in clean dry air at Ta was carried out at <5% relative humidity on all films.

Thin-Film Transistors: TFTs were fabricated by patterning the In-X-O films with oxalic acid to reduce gate leakage, followed by evaporation of aluminum source-drain contacts through a shadow mask. Device dimensions were L = 50 μm, W = 1 mm. Electrical measurements were carried out either in air or a vacuum probe station (<5 $\times 10^{-1}$mbar) with an Agilent B1500A parameter analyzer. Transfer characteristics were measured in both the linear and saturation regimes of the TFT. Samples for low-temperature measurements were mounted on an Advanced Research Systems liquid nitrogen cryostat controlled by a Lake Shore 331 temperature controller. Mobilities were extracted in the range of V_G-V_T between 5 and 25 V where leakage currents were always >10× lower than the source-drain current. Effective mobility μ_{EFF} was calculated in the linear regime (V_D = 5 V) using Equation (10) and choosing appropriate onset voltages V_{on} estimated from the transfer characteristics. This method gave an average mobility for both trapped and untrapped electrons and correctly represented the gate voltage dependence of the mobility [39].

$$\mu_{EFT}(V_G) = \frac{L}{WC_i}\frac{I_D(V_G)}{V_D(V_G - V_{on})} \tag{10}$$

X-Ray Absorption Spectroscopy: Experiments were conducted at sector 5BMD of the Advanced Photon Source of Argonne National Laboratory (ANL). A Si(111) double crystal monochromator was used to produce a 12 mm (horizontal) by 1 mm (vertical) beam. The incident beam energies were tuned to near the In, Sc, Y K-edge and La L-edge (27.940, 4.492, 17.038, 6.266 keV, respectively) to measure XAS spectra at the above four edges. Films were placed 45, from the incident direction, and data were collected in fluorescence mode using a four-element silicon drift detector (SII NanoTechnology). The reference powders were uniformly spread on Scotch tape (3M Corp.) and measured in transmission mode using an ionization chamber (Oxford-Danfysik). EXAFS spectra were extracted and normalized using athena software packages [140]. The intrinsic loss factor ($S_0^2 = 1.06$) for fitting the indium K-edge was obtained by modeling of the reference powders for each absorbing atom, and kept fixed when fitting the film data. The bond distances, coordination numbers, and Debye-Waller factors were obtained by the FEFF simulations using a cluster of the bixbyite structure with a radius of 6 Å centered on the absorbing atom. All the normalized absorption coefficients χ(k) were Fourier transformed using a Hanning window over the specified k-range and fit in k-space with k-weight 3.

Ab Initio Molecular Dynamics Simulation: The amorphous In-X-O structures were generated using first-principles MD as implemented in the Vienna Ab initio Simulation package (vasp) [105, 116, 117, 118]. The calculations were based on density functional theory within generalized gradient approximation (GGA) with the PBE functional [114]. For the initial structure, a bixbyite In_2O_3 cell containing 130 atoms ($In_{52}O_{78}$) and a density of 7.116 gcm^{-3} was used. For ternary structures, 20% of In atoms in crystalline In_2O_3 were replaced by metal X (Sc, Y, or La) resulting in the stoichiometric structure $In_{44}X_{10}O_{81}$; the cell volume was adjusted to maintain the density in the In-based samples. Also, amorphous nonstoichiometric $In_{44}X_{11}O_{77}$ structures were modeled by removing oxygen atoms in the initial structures, i.e., prior to liquid quench process. The amorphous In-O and In-X-O structures were then obtained using the liquid-quench approach as follows. First, to remove

any crystalline memory, each initial structure was melted at 3000 K for 6 ps. The melt was then cooled to 1700 K at the rate of 100 K/1.2 ps, and then rapidly quenched to 100 K at the rate of 200 K/1.2 ps. In order to make the calculations computationally efficient, a cutoff of 260 eV was used and the k-point sampling was restricted to k-point only during melting and quenching processes. Finally, the structures were equilibrated at 300 K for 6 ps with a cut-off energy of 400 eV. All simulations were carried out within NVT ensemble with Nose'-Hoover thermostat using integration time step of 2 fs.

Structural Characterization: Grazing incidence XRD was carried out on a Rigaku ATX-G workstation (Cu Kα, λ = 1.541 Å) with an incidence angle, $\alpha = 0.5^o$, compared to a critical angle for In_2O_3 of $\alpha C = 0.37^o$. After background subtraction, the degree of crystallinity χ_c was estimated from the ratio of area under the crystalline peaks (after subtracting the amorphous peak) to total area under the X-ray diffraction pattern. Diffraction peaks were fitted with a pseudo-Voigt function (Gaussian-Lorentzian product). Atomic force microscopy (AFM) was carried out in tapping mode on a Bruker ICON system. XPS was carried out on a Thermo Scientific ESCALAB 250Xi with O1s peaks being deconvoluted into separate peaks at 529.3, 530.9, and 532.1 eV.

6. ACKNOWLEDGEMENTS

The authors acknowledge support from the Office of Naval Research (MURI N00014-11-1-0690; J.S., K.S.) and the Materials Research Center of Northwestern University (NSF-MRSEC DMR-1121262; R.K., L.Z.). This work made use of the J. B. Cohen X-Ray Diffraction Facility supported by the NSF-MRSEC program (DMR-1121262) at the MRC-NU. XAS measurements were carried out at the 5BMD beamline of the DuPont-Northwestern-Dow Collaboration Assess Team (DND-CAT) at the Advanced Photon Source (APS) of Argonne National Laboratory (ANL). This work also made use of the KECK-II and NIFTI

facilities at Northwestern University's Atomic and Nanoscale Characterization Experimental Center (NUANCE) for XPS and AFM. NUANCE was supported by NSF-NSEC, NSF-MRSEC, Keck Foundation, the State of Illinois, and Northwestern University. The authors thank Prof. M. Grayson for insightful discussions. Computational resources were provided by the NSF-supported XSEDE program, Grant TG-DMR080007.

IV. COMPOSITION-DEPENDENT STRUCTURAL AND TRANSPORT PROPERTIES OF AMORPHOUS TRANSPARENT CONDUCTING OXIDES

Rabi Khanal[1] D. Bruce Buchholz [2] Robert P.H. Chang[2] Julia E. Medvedeva[1]

[1]*Department of Physics, Missouri University of Science & Technology*

Rolla, MO 65409

[2]*Department of Materials Science and Engineering, Northwestern University, Evanston, IL 60208*

ABSTRACT*

Structural properties of amorphous In-based oxides, In-X-O with X=Zn, Ga, Sn, or Ge, are investigated using ab-initio molecular dynamics liquid-quench simulations. The results reveal that Indium retains its average coordination of 5.0 upon 20% X fractional substitution for In, whereas X cations satisfy their natural coordination with oxygen atoms. This finding suggests that the carrier generation is primarily governed by In atoms, in accord with the observed carrier concentration in amorphous In-O and In-X-O. At the same time, the presence of X affects the number of six-coordinated In atoms as well as the oxygen sharing between the InO_6 polyhedra. Based on the obtained interconnectivity and spatial distribution of the InO_6 and XO_x polyhedra in amorphous In-X-O, composition-dependent structural models of the amorphous oxides are derived. The results help explain our Hall mobility measurements in In-X-O thin films grown by pulsed-laser deposition and highlight the importance of long-range structural correlations in the formation of amorphous oxides and their transport properties.

*Published in Physical Review B **91** 205203 (2015).

1. INTRODUCTION

Driven by technological appeal, the research area of amorphous transparent conducting oxides has grown tremendously since the first demonstration of the unique properties of these materials more than a decade ago [32, 41]. Today, amorphous oxides of post-transition metals, such as indium-based ternary In-Sn-O (a-ITO) and In-Zn-O (a-IZO) or quaternary In-Ga-Zn-O (a-IGZO) and Zn-In-Sn-O (a-ZITO), exhibit optical, electrical, thermal, and mechanical properties that are comparable or even superior to those possessed by their crystalline counterparts, pushing the latter out of the market [42, 58, 69, 181]. Yet, the structural variations associated with the crystalline-to-amorphous transition in these oxides are far from being understood. From experimental characterization, primarily via extended x-ray absorption fine structure (EXAFS) measurements [51, 54, 56, 147] and from theoretical models derived from molecular dynamics (MD) simulations, it has been established that the first-shell characteristics – the average metal-oxygen distances and coordination – remain nearly intact upon the transition to the amorphous phase [47, 49, 50, 68, 81, 84, 137, 138, 139, 182]. This suggests that, upon amorphization, both the optical band gap and the electron effective mass governed by the metal-oxygen interactions [67, 151, 152], should deviate only insignificantly from the crystalline values. Hence, the key features of the electronic band structure of a transparent conducting oxide host [24, 25, 183] should be preserved under the structural transition.

Recent investigations of amorphous indium oxide (a-IO) showed that the presence of nanocrystalline In_2O_3 inclusions whose size varies with deposition temperature, limits the electron transport properties via scattering [147]. Nucleation of such nanocrystallites was found in amorphous In-O structures obtained via MD simulations at slow cooling rates (5K/ps). Furthermore, the spatial distribution and interconnectivity of the fully-coordinated In atoms, i.e., the InO_6 polyhedra, was shown to depend strongly on the quench rates in the MD simulated structures. Based on a thorough comparison of the experimental and

theoretical results, the observed peak in the electron mobility was found to correspond to the structure with long chains of the InO_6 polyhedra connected primarily via corner sharing [147]. Thus, the long-range structural characteristics, i.e., how the metal-oxygen polyhedra are integrated into a continuous network, play a key role in the transport properties of the amorphous oxides.

Amorphous transparent conducting oxides are compositionally adaptive and allow incorporation of large fractions of other post-transition metals, e.g., Sn, Zn, or Ga, into the In-O matrix. The presence of additional cations affects the crystallization temperature and often makes it easier to achieve an amorphous state of the multicomponent oxide. Yet, the microscopic effect of the composition on the local and long-range structural characteristics of amorphous In-based oxides as well as on their transport properties – carrier generation, carrier concentration, and carrier mobility – is still unclear.

In marked contrast to the crystalline transparent conducting oxides, where the electron mobility is governed primarily by the scattering on the ionized or neutral impurities, phonons, and grain boundaries, the local distortions of the metal-oxygen polyhedra and the long-range structural disorder in amorphous oxides makes their transport properties more complex. Although amorphous oxides lack grain boundaries, additional electron scattering is expected to occur due to (i) size and spatial distribution of the nanocrystalline inclusions; (ii) spatial distribution and clustering of incorporated cations in multicomponent oxides; (iii) abundant trap defect states; and (iv) piezoelectric effects associated with internal strains. Clearly, chemical composition, oxygen deficiency as well as deposition temperature will have a strong effect on the above processes and should be systematically investigated.

In this work, we present a systematic study of the structural properties of ternary amorphous In-based oxides, In-X-O with X=Zn, Ga, Sn, or Ge, denoted below as a-IXO, obtained via liquid-quench MD simulations. To gain a thorough understanding of the role of composition in the structural properties of the amorphous oxides, the characteristics of the

first, second, and third shells are compared between amorphous indium oxide, ternary a-In-X-O as well as the corresponding crystalline oxides. In addition to the average distances and coordination numbers from the standard pair distribution functions, statistical distributions and weighted averages as a function of cation number and/or type of oxygen sharing are presented. The results reveal the importance of long-range structural correlations governed by the composition and explain the observed carrier concentration and mobility trends in amorphous In-X-O. All results presented in this work are for stoichiometric oxides; the effect of oxygen non-stoichiometry, important for the defect formation, carrier generation, and carrier transport in amorphous oxides [84, 85, 91, 93, 184, 185, 186], will be discussed in a future study.

2. COMPUTATIONAL METHOD

The amorphous a-In-O and a-In-X-O structures were generated using first-principles molecular dynamics as implemented in the Vienna Ab Initio Simulation package (VASP) [105, 116, 117, 118]. The calculations are based on the density functional theory (DFT) [102, 103] with PBE functional within the projector augmented-wave method [115, 122, 148]. For the initial structure, we used a cubic 130-atom cell of bixbyite In_2O_3 with density 7.12 gm/cm^3. To obtain ternary In-X-O structures, we randomly replaced 20% of the In atoms in the initial structure by respective metal X (Zn, Ga, Sn, or Ge) and adjusted (i) the number of oxygen atoms to maintain stoichiometry (as well as charge neutrality); and (ii) the cell volume to maintain the density in the In-based samples. For each initial In-O or In-X-O structure, we performed molecular dynamics simulations of liquid quench as follows. First, to remove any crystalline memory, each initial structure was melted at 3000 K for 6 ps. The melt was then cooled to 1700 K at the rate of 100 K/1.2 ps, and then rapidly quenched to 100 K at the rate of 200 K/1.2 ps. In order to make the calculations computationally efficient, we used low cut-off of 260 eV and restricted the k-point sampling to Γ point only

during melting and quenching processes. Finally, each structure was equilibrated at 300 K for 6 ps with a cut-off energy of 400 eV. All simulations were carried out within NVT ensemble with Nosé-Hoover thermostat using integration time step of 2 fs.

3. GROWTH AND CHARACTERIZATION

Amorphous oxide thin-films were grown by pulsed-laser deposition (PLD) from a dense hot-pressed indium oxide, zinc oxide, tin oxide and gallium oxide targets (25 mm diameter). PLD was accomplished with a 248 nm KrF excimer laser with 25 ns pulse duration and operated at 2 Hz. The 200 mJ/pulse beam was focused onto a 1 mm x 2 mm spot size. The target was rotated at 5-rpm about its axis to prevent localized heating. The target-substrate separation was fixed at 10 cm. For multi-component films the appropriate basis-oxide targets were employed. A computer controlled shuttle was used to alternate ablation between targets. Less than one monolayer of material was deposited in a typical cycle between the targets to help insure uniformity of film composition; the ratio of the pulses for each metal oxide in each cycle was adjusted to obtain the desired film composition. The compositions reported are nominal compositions: the ratio of the number of dopant pulses to total pulses. The films were grown on silicon substrates in an O_2 ambient of 8 mTorr. The substrates were attached to the substrate holder with silver paint and grown at a temperature of -25 °C to insure amorphous films.

Sheet resistance (R_s: Ω/□), carrier type, area carrier-concentration (n_a: 1/cm^2), and carrier mobility (μ_{hall}: cm^2/V·s) were measured with a Ecopia 3000 Hall measurement system on samples in the van der Pauw geometry. Carrier density (n_v: 1/cm^3) and resistivity (ρ: Ω·cm) were calculated by dividing the area carrier-concentration and sheet resistance, respectively, by the film thickness. Film thickness (d: nm) was measured using a spectral reflectometer (Filmetrics F20) and were shown to range from 250-300 nm.

4. RESULTS AND DISCUSSION

4.1. Local (short-range) structural characteristics.

4.1.1. In-O distances in amorphous In-O and In-X-O. To understand how composition affects the structural properties of amorphous In-based oxides, we first analyse the local structure of the InO_x polyhedra, i.e., the In-O distances and the coordination of In with oxygen atoms. The results are compared to the corresponding values for In-O in a-In-O and then to those for X-O values in a-In-X-O, X=Zn, Ga, Sn, or Ge.

The radial In-O distribution functions in a-In-O and a-In-X-O show insignificant variation in the width and peak position for different X, Fig.1. The calculated standard deviation, σ^2, for the first-shell distances slightly increases from 0.011 Å^2 for a-In-O and a-IZO to 0.012 Å^2 for a-IGO, and to 0.013 Å^2 for a-ITO and a-IGeO. Despite the different ionic radii of the X cations, the average In-O distance is similar in a-In-O and all a-In-X-O. For a more accurate comparison of the average In-O distances in a-In-O and a-In-X-O the average pair correlation function [125, 126] is calculated according to:

$$l_{av} = \frac{\sum_i l_i \, exp\left(1 - \left(\frac{l_i}{l_{min}}\right)^6\right)}{\sum_i exp\left(1 - \left(\frac{l_i}{l_{min}}\right)^6\right)}, \tag{11}$$

where the summation runs over all oxygen neighbors of a particular In atom and l_{min} is the smallest In-O distance in the i-th InO_x polyhedron. The average pair correlation function is weighted by taking into account the individual metal-oxygen bond lengths, and eliminates the long-distance bonds that represent non-interacting M-O pairs. The results, given in the insert of Fig. 1, reveal that the average pair correlation function increases from 2.161 Å for a-In-O to 2.165 Å for a-IGO; 2.166 Å for a-IZO; 2.167 Å for a-IGeO; and to 2.173 Å for a-ITO. Hence, the addition of X cations leads to a slight increase of the average In-O distance which remains to be below the corresponding value in crystalline In_2O_3, namely, 2.18 Å.

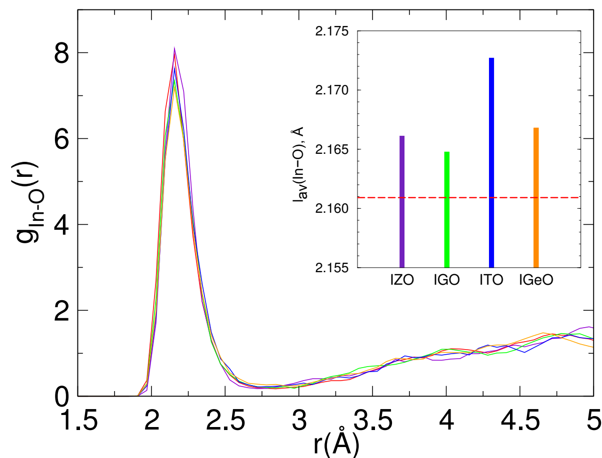

Figure 1. (Color online) Radial In-O pair distribution functions in amorphous In-O and In-X-O. In the inset, the calculated average In-O pair correlation function, l_{av}, is plotted for amorphous In-X-O. The horizontal dash line represents the corresponding l_{av} value in amorphous In-O.

To further understand the effect of X on the first-shell In-O distances, the average In-O distance (l_{av}) is calculated as a function of the number of X atoms in the second shell of the In atoms. For this, for every indium atom, the number of X nearest neighbours, i.e, those located within a sphere of radius 3.4 Å is determined. The latter corresponds to the In-In distance in c-In_2O_3. There may be no, one, two, three, or four X neighbors in the second shell of an In atom; the number of In atoms in each of the groups is given as a percent of the total number of In atoms in the cell, c.f., Table 1. The average pair correlation functions (Eq. 11) were then calculated for each of the In groups. First of all, it is found that for indium atoms with no X neighbors in the second shell, the calculated average In-O pair correlation function differs from the one in a-In-O (l_{av}=2.161 Å) being larger for X=Zn or Sn (l_{av} ~2.176 Å), and smaller for X=Ga or Ge (l_{av} ~2.154 Å), Table 1. The ionic size of the former two cations (Zn and Sn) is larger than that of the latter two (Ga and Ge); in addition, the strength of the X-O bonds is weaker in the former case compared to the latter case. Hence, one can argue that Ga and Ge, having short and strong bonds with their neighboring oxygen atoms, increase the In-O distance of their nearest neighbor

In atoms. As a result of such "oxygen-getter" behavior [149], the In-O bond length for In atoms that are farther away from Ga and Ge cations, decreases.

Different mechanism(s) should be sought for a-IZO and a-ITO because the ionic size of Zn or Sn is smaller compared to that of In; and the metal-oxygen bond strength is similar for In, Zn, and Sn. In the case of a-IZO, the longer In-O distances for the In atoms that do not have a Zn atom in the second shell, Table 1, are likely to originate from an increased average In-O coordination away from Zn: the average In coordination for the In atoms that do not have a Zn neighbor is ~5.4 that is notably higher than for a-In-X-O with X=Sn, Ga, or Ge, Table 1, or for a-In-O where the average In coordination is ~5.0. In a-ITO, a strong preference of Sn atoms toward natural coordination and clustering discussed in the sections below, may lead to longer In-O distances away from Sn. Clustering of Sn atoms is already evidenced from the large number, 48 %, of the In atoms with no Sn neighbor in the second shell as compared to all other cases, Table 1.

Table 1. Average In-O pair correlation function, l_{av} in Å, and effective coordination number, ECN(In-O), cf. Eq. 12, as a function of the number of X atoms, NN_X, located within the radial distance of 3.4 Å from a central In atom. The fractional number of the In atoms, N_{In}, in percent, that have a certain number of X neighbors in the second coordination sphere, i.e., with NN_X=0, 1, 2, 3, or 4, is given in brackets. The total average pair correlation function, $< l_{av} >$, and total average effective coordination number, <ECN(In-O)>, are given in the last column. For comparison, the average In-O pair correlation function is 2.161 Å and the average In-O effective coordination number is 5.0 in a-In-O.

	l_{av}, ECN(In-O) (N_{In})					
NN_X	0	1	2	3	4	Average
IZO	2.177, 5.4 (20)	2.170, 5.1 (46)	2.156, 5.0 (27)	2.151, 5.1 (7)	—	2.166, 5.1
IGO	2.156, 5.0 (30)	2.174, 5.2 (46)	2.149, 5.0 (20)	2.199, 6.2 (2)	2.198, 5.2 (2)	2.165, 5.1
ITO	2.175, 5.1 (48)	2.168, 5.1 (41)	2.180, 5.5 (11)	—	—	2.173, 5.1
IGeO	2.153, 5.1 (30)	2.172, 5.3 (50)	2.144, 5.2 (11)	2.213, 5.8 (9)	—	2.167, 5.3

When the number of X nearest neighbors for a particular In atom increases, the average In-O distance behaves differently in a-In-X-O. In the case of X=Zn, the In-O pair correlation function decreases with the number of second-shell X neighbors, Table 1. Significantly, the average In-O distance for the In atoms with two or three Zn nearest neighbors is nearly equal to that found in crystalline In_2ZnO_4, 2.154 Å. In contrast to a-IZO, there is no consistent trend for the In-O distances for X=Ga, Sn, or Ge, Table 1. This may be explained by: (i) comparable bond strengths for Zn-O and In-O as opposed to those for Ga-O and Ge-O; and (ii) the fact that Zn atoms are uniformly distributed throughout the In-O matrix – in marked contrast to Ge, Ga and especially Sn atoms that show a strong tendency to cluster (as discussed in more details in Section 4.2.3). The strong Ga-O and Ge-O bonds tend to increase the In-O distances as the number of Ga or Ge nearest neighbors increases (with an exception for the case of two X atoms, Table 1, which we attribute to a particular spatial distribution of the two X atoms, e.g., a possibility for X-X dimer formation). The above findings are consistent with crystalline multicomponent oxides: the average In-O distance in $GaInO_3$ (2.174 Å) and $In_2Ge_2O_7$ (2.163 Å) is longer as compared to that in In_2ZnO_4 (2.154 Å).

Among the X cations considered in this work, tin results in the largest average In-O distance, Figure 1. At the same time, the least variation in the average In-O distances is observed in a-ITO: independent of the number of Sn nearest neighbors, the average In-O distance remains close to the overall average, 2.173 Å, Table 1. As will be shown in Section 4.1.3, presence of tin has the least effect on the In-O coordination statistics, i.e., the numbers of differently coordinated In atoms remain unchanged upon introduction of tin. Indeed, the ionic size, bond strength, and preference for six-fold coordination with oxygen atoms are similar for In and Sn – in accord with the presence of fractional site occupation for Sn and In in crystalline $In_4Sn_3O_{12}$ and other crystalline oxides that contain In and Sn. Hence, one needs to look beyond the local, short-range structural features of amorphous oxides in order to explain the increase of the average In-O distance in a-ITO with respect to a-In-O. Indeed,

the spatial distribution and connectivity of SnO_x and InO_6 polyhedra in a-ITO provide a plausible explanation, see Section 4.2.3.

Thus, although all X cations considered in this work result in a slightly increased average In-O distance, a thorough structural analysis suggests that the origin of the X effect is different in a-In-X-O. Longer In-O distances are expected to increase the electron effective mass and, hence, may contribute to the reduced mobility in amorphous In-X-O as compared to amorphous In-O. However, the obtained changes in the In-O distances are not significant enough to explain the observed mobility reduction as the fraction of X increases. We believe that the transport properties in amorphous oxides are governed by spatial distribution and connectivity of the MO_x polyhedra, i.e., the long-range features of the amorphous structure, rather than the local M-O bonds.

4.1.2. X-O distances in amorphous In-X-O. The radial X-O pair distribution functions in a-In-X-O are shown in Fig. 2. Also, the calculated average pair correlation function l_{av}(X-O), Eq. 11, for each a-In-X-O structure is given in the insert of Fig. 2. The results reveal that for X=Sn or Ge (for X=Zn or Ga), the average X-O distance is shorter (longer) than the natural X-O distance, i.e., the distance in the corresponding crystalline binary oxides. The same trend is found when the average X-O distances are compared for crystalline binary and crystalline ternary oxides. The Sn-O and Ge-O distances are shorter in the ternary oxides with In: the average Sn-O distances are 2.06 Å and 2.09 Å in $In_4Sn_3O_{12}$ and SnO_2, respectively; the average Ge-O distances are 1.74 Å and 1.88 Å in $In_2Ge_2O_7$ and cristobalite/rutile GeO_2, respectively. The Zn-O and Ga-O distances are slightly longer in the ternary oxides with In: the average Zn-O distances are 1.99 Å and 1.98 Å in In_2ZnO_4 and wurtzite ZnO, respectively; and the average Ga-O distances are 1.94 Å and 1.93 Å in $GaInO_3$ and Ga_2O_3, respectively [187].

Significantly, in the case of Zn addition, the radial Zn-O distribution features a non-zero tail at longer distances, i.e., there is an appreciable amount of long-distance Zn-O bonds in a-IZO, Fig. 2. In contrast, the radial distribution functions for X=Ga, Sn, or Ge are

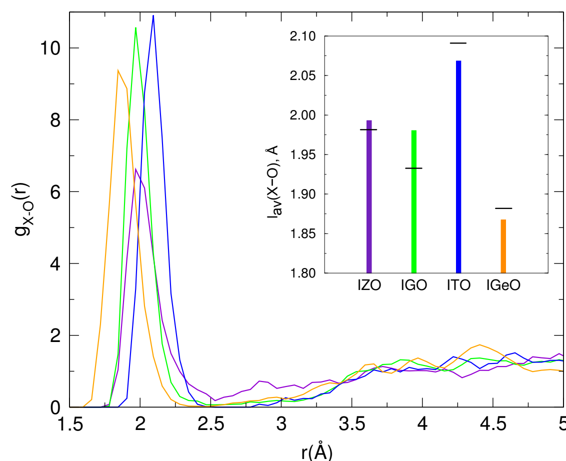

Figure 2. (Color online) Radial pair distribution function of X-O in amorphous In-X-O. The inset shows the average X-O correlation function, l_{av}, in amorphous In-X-O; black bar lines represent the average X-O distance in the corresponding crystalline binary oxides.

narrow, with the calculated standard deviation σ^2 <0.001 Å^2, and vanish above ~2.4 Å, Fig. 2. Thus, comparing the shape of the radial X-O pair distribution function for a-In-X-O, we conclude that Zn in amorphous In-Zn-O allows for both shorter and longer than its natural Zn-O distances, whereas Sn (Ga) in a-In-X-O allows only for shorter (longer) distances with oxygen atoms than the corresponding natural distances. In contrast, the Ge-O distances in a-InGeO exhibit the least deviation from the natural distance, as one should expect from the strong Ge-O bonds.

The deviation of the X-O distances from the natural X-O bond length may determine the connectivity between the XO_x polyhedra. For example, long X-O distances may lead to a formation of chains of connected XO_x polyhedra, whereas short X-O distance may limit the connectivity between the XO_x polyhedra or promote clustering of the XO_x polyhedra, to be discussed in Section 4.2.3. Here we stress the importance of the connectivity of the XO_x polyhedra which may affect (i) the degree of amorphization of the In-based matrix due to a specific spatial distribution of X; (ii) the carrier mobility controlled by the scattering on XO_x clusters or nanocrystalline inclusions; and (iii) the mechanical properties of the amorphous oxides and/or the electrical properties in oxides under an external strain.

4.1.3. In-O coordination in amorphous In-O and In-X-O. The effective coordination number (ECN) can be calculated based on the obtained pair correlation function (c.f., Eq. 11) for every In atom in the cell:

$$ECN = \sum_{i} \exp\left(1 - \left(\frac{l_i}{l_{av}}\right)^6\right). \tag{12}$$

In all In-based amorphous oxides, indium is under-coordinated with oxygen atoms, Fig. 3, as compared to the c-In_2O_3 with six-coordinated In atoms, that is InO_6 polyhedra. Moreover, at 20 % substitution, all X additions considered in this work have little effect on the average In-O coordination increasing it only slightly with respect to $\langle ECN \rangle$=5.0 in a-In-O: Zn, Ga, and Sn result in $\langle ECN \rangle$ ~5.1, whereas Ge increases it further to $\langle ECN \rangle$ ~5.3. This is consistent with the longer average In-O distances in a-In-X-O, discussed in Section 4.1.1. Notably, the average effective coordination number is increased to 5.4 for the In atoms which do not have a Zn neighbor in the second shell, i.e., those located away from Zn in a-IZO, Table 1.

To determine the origin of the increased average In-O coordination in a-In-X-O, the coordination of every In atom is calculated within a sphere of radius 2.36 Å (this is ~5 % longer than the longest first-shell In-O distance in c-In_2O_3, 2.25 Å). The number of differently coordinated In atoms gives statistical distribution of the In coordinations in each system. There are three, four, five, and six-coordinated In atoms, denoted below as InO_x, Fig. 4. In a-In-O and all a-In-X-O except for a-IGeO, around half of the In atoms are five-coordinated. Importantly, addition of Zn, Ga, and especially Ge results in an increase of the number of InO_6 and a suppression of both InO_5 and InO_4. In marked contrast, the number of InO_6 changes insignificantly upon Sn addition, so that the aforementioned slight increase of $\langle ECN(In\text{-}O) \rangle$ in a-ITO originates from a suppressed number of InO_4 and an increased number of InO_5 as compared to a-In-O.

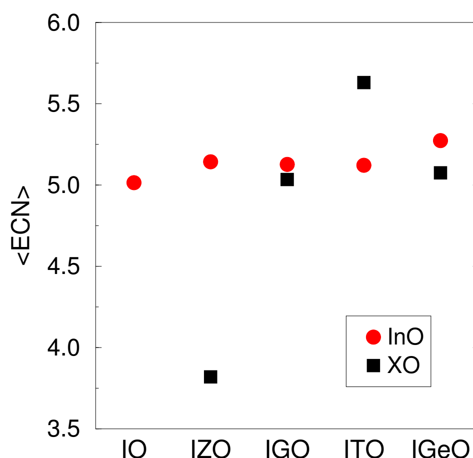

Figure 3. (Color online) Average effective coordination number for In-O and X-O in amorphous In-O and In-X-O calculated according to Eq. 2.

The above distribution of differently coordinated In atoms, Fig. 4, suggests that Sn stands apart from the other additions since it has a negligible effect on the In coordination statistics. In contrast, Ga, Zn, and Ge increase the number of six-coordinated In atoms, with Ge resulting in the most pronounced tendency toward the natural In coordination. These findings may be instructive to understand the role of chemical composition in carrier generation, carrier transport and amorphization of In-based oxides (see Section G below).

4.1.4. X-O coordination in amorphous In-X-O. The calculated average effective coordination number for X atoms, <ECN(X-O)>, given in Fig. 3, reveal that the average co-ordination of all addition elements is close to their natural coordination, i.e., the coordination in the corresponding crystalline binary oxides – in marked contrast to under-coordinated In. Indeed, the X-O coordination calculated as an average number of oxygen neighbors within a sphere of radius r, i.e., as a function of the radial distance from a central X atom, Fig. 5, illustrates that the X atoms quickly reach and exceed their natural coordination. Moreover, statistical analysis reveals that (1) *all* Sn atoms are six-coordinated above r=2.36 Å (as in crystalline SnO_2 and in $In_4Sn_3O_{12}$); (2) all but one Zn (9%) atoms are four-coordinated above 2.24 Å (as in wurtzite ZnO and in In_2ZnO_4); (3) about a half of the Ga atoms are

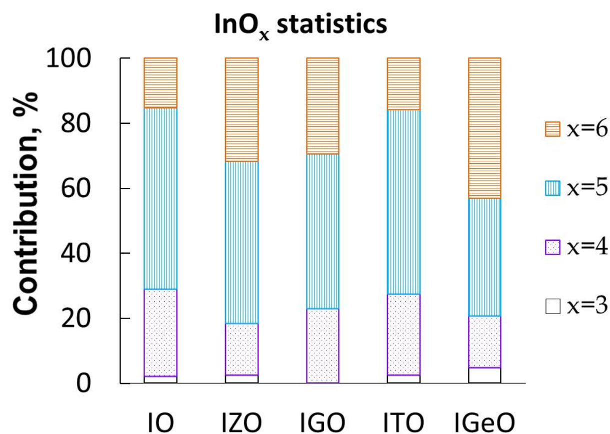

Figure 4. (Color online) The number of differently coordinated indium atoms, InO_x, in amorphous In-O and In-X-O calculated within 2.36 Å around a central In atom.

five-coordinated above 2.32 Å with an equal number of four and six-coordinated Ga for the other half Ga atoms (Ga is four and six-coordinated in β-Ga_2O_3, and five-coordinated in $GaInO_3$ and $InGaZnO_4$); and (4) about a half of Ge atoms are six-coordinated above 2.22 Å with an equal number of four and five-coordinated Ge for the other half Ge atoms (Ge is four-coordinated in cristobalite GeO_2 and in monoclinic $In_2Ge_2O_7$, and six-coordinated in rutile GeO_2).

We also note that Sn, Ga, and Ge average coordination reach a plateau at longer X-O radial distances, whereas Zn continues to steadily increase its coordination above the natural one – as expected from the non-vanishing Zn-O pair distribution function, Fig. 2. In marked contrast, In atoms in a-In-O remain under-coordinated even at r=2.6 Å, Fig. 5. This finding suggests that In atoms remain to serve as a main source of oxygen defects upon introduction of X. We should stress, however, that the results discussed in this work are for stoichiometric oxides; the effect of oxygen non-stoichiometry (for amorphous oxides grown at different oxygen partial pressures) on the relative coordination of the constituent cations will be discussed elsewhere.

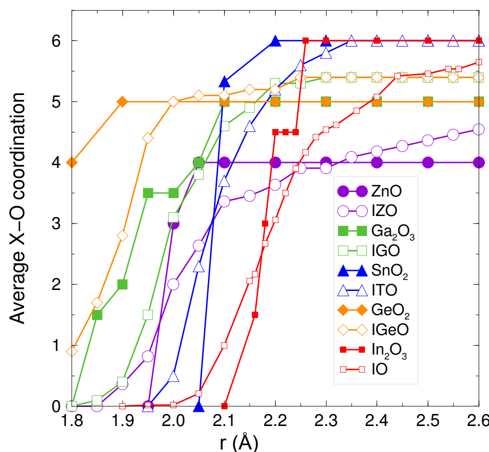

Figure 5. (Color online) Average X-O coordination in crystalline and amorphous oxides as a function of the radial distance r, in Å, from a central X atom. Also included is the average In-O coordination in c-In_2O_3 and a-In-O. Filled (open) symbols represent crystalline (amorphous) oxides.

Most importantly, the structural characteristics of a-In-X-O imply that fractional substitution of indium with alternative metals does not govern the carrier generation directly. Indeed, additional cations such as Sn^{4+}, Ga^{3+}, or Zn^{2+} in amorphous indium oxide have a weak effect on the carrier concentration: at 30% X fractional substitution for In in a-In-X-O, the observed carrier concentration is measured to be 0.8×10^{20} cm^{-3}, 1.2×10^{20} cm^{-3}, and 1.6×10^{20} cm^{-3} for X=Ga, Zn, and Sn, respectively. Despite the different valence of the additional cations, the resulting carrier concentrations are comparable in amorphous In-X-O and, moreover, are similar to the one observed for a-In-O, 1.6×10^{20} cm^{-3}. This implies that the X cations in amorphous oxides do not serve as dopants – in marked contrast to binary crystalline oxides where proper aliovalent external doping, e.g., Sn^{4+} on In^{3+} sites, increases the carrier concentration by orders of magnitude or to multicomponent crystalline oxides, e.g., $InGaZnO_4$, where cation substitutional disorder, Ga^{3+} on Zn^{2+}, is the major carrier donor [188].

4.2. Long-range structural characteristics.

4.2.1. In-M distance distribution and total In-M coordination. The analysis of the M-O (where M=In or X) bond lengths and coordination has shown that, on average, the local structure of the MO_x polyhedra remains nearly unchanged upon the transition from crystalline to amorphous state. To understand the transport properties of amorphous oxides, the long-range structural characteristics, i.e. the In-M shell distances and coordination that determine how the MO_x polyhedra are connected into a network, should be considered in great detail.

The calculated radial distribution functions for the In-M shell in a-In-O and a-In-X-O are shown in Fig. 6. The main peak in the distribution, centred at about 3.4 Å, is wide so that it combines the second and third shells in the c-In_2O_3 associated with six edge-shared In-In bonds at ~3.35 Å and six corner-shared In-In bonds at ~3.83 Å, respectively. A suppressed third-shell peak in all amorphous oxides does not imply, however, that the total In-In coordination is reduced upon amorphization. Indeed, the total In-M coordination, calculated as a function of the distance from an In atom, Fig. 6, reaches and exceeds the expected number, 12, above 4.3 Å in amorphous In-O and In-X-O. The absence of a distinct third-shell peak in the total In-M distance distribution in amorphous oxides is due to the fact that a significant part of the edge-shared In-M pairs (about 60 %) become corner-shared upon amorphization, as will be discussed in detail below, see Section 4.2.2.

Addition of Ga or Zn increases the total In-M coordination as compared to that in a-In-O, whereas Sn slightly reduces it, Fig. 6. Importantly, the X effect on the In-M coordination is reflected not only in the In-X coordination but also in the In-In coordination which reveals a similar composition-dependent trend, see insert for Fig. 6, with lowest coordination in a-ITO and a higher coordination in amorphous IGO and IZO as compared to that of a-In-O. Although the smallest In-M coordination in a-ITO seems to be in accord with the longest average In-O distance in this oxide, the increased In-M coordination for X=Zn, Ga, or Ge cannot be explained by the first shell changes alone since the average In-O

distance for these X cations also increases with respect to that in a-In-O, Fig. 1. Hence, it is necessary to further analyse the characteristics of the In-M shell.

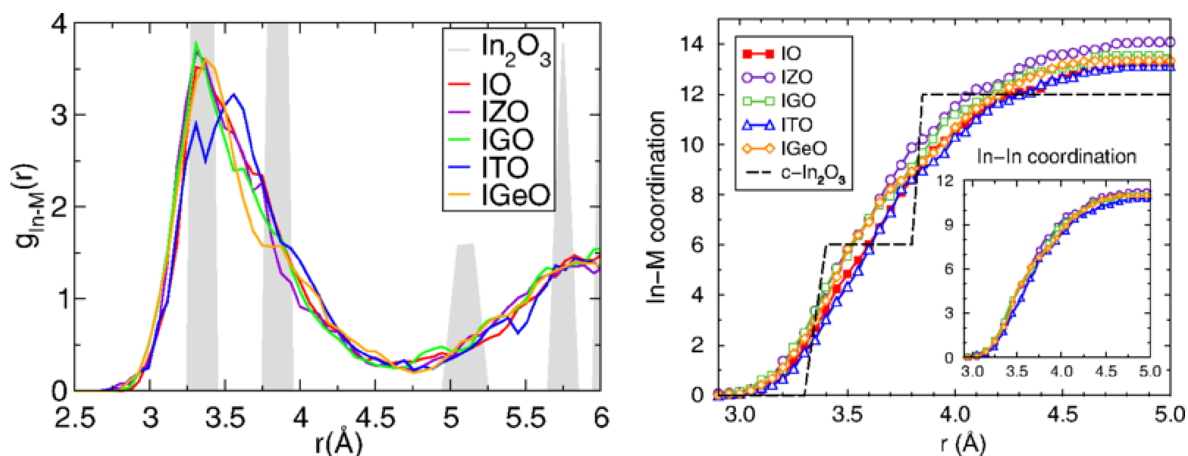

Figure 6. (Color online) (Left) Radial In-M distribution function, g_{In-M}(r), where M=In or X=Zn, Ga, Sn, Ge) as a function of distance from an In atom in crystalline In_2O_3 and in amorphous In-O and In-X-O. (Right) Total In-M coordination, where M=In or X=Zn, Ga, Sn, Ge, as a function of distance from an In atom in crystalline In_2O_3 and in amorphous In-O and In-X-O. The inset shows the In-In coordination as a function of distance for the same.

4.2.2. Edge- and corner-shared In-M in amorphous oxides. The proximity of the indium second and third shells (at 3.35 Å and 3.83 Å in c-In_2O_3) causes the corresponding pair distribution functions to overlap in the amorphous state [147]. The total In-M distance distribution becomes over 1 Å wide, Fig. 6, making the exponential fit in the l_{av} and ECN calculations, Eqs. 11 and 12, inapplicable. It is important, however, to gain a thorough understanding of the In-M shell structure since it determines the interconnectivity between the MO_x polyhedra.

Based on the optimized atomic coordinates of the MD simulated structures, one can distinguish between the edge- and corner-shared In-M pairs as follows. For every In atom, the number of metal neighbors (In or X) that share one, two, or three oxygen atoms with the central In atom is determined, representing the number of corner, edge, or face-shared In-M pairs, respectively. In this analysis, one should choose a maximum M-O distance to be considered as an M-O bond in the M-M sharing – this cut-off value should ensure that

the first shell M-O distances in the corresponding pair distribution function (i.e., those that belong to the first In-O or X-O peak) are included into consideration. In our analysis, we set the cut-off values to 2.36 Å for In-O bond and Sn-O bond; 2.20 Å for Zn-O bond and Ga-O bond; and 2.10 Å for Ge-O bond. The In-M distance and In-O-M angle distribution functions for both edge- and corner-shared pairs are given in Figure 7. The important findings are as follows:

(1) The *edge-shared* In-M distances are distributed between 2.9 Å and 3.7 Å. For all X, the peak in the distribution function is located at ~3.30 Å which is close to the second shell edge-shared In-In distance of 3.35 Å in c-In_2O_3. The width of the distribution function varies with X; the calculated standard deviation, σ^2, for the edge-shared In-M distances increases from 0.013 Å^2 for a-In-O to 0.015 Å^2 for a-IZO, to 0.020 Å^2 for a-IGO, to 0.021 Å^2 for a-ITO, and to 0.026 Å^2 for a-IGeO. The corresponding angle distribution for the edge-shared In-M pairs is from 80° to 110°, Figure 7. The average In-O-M angle for the edge-shared In-M pairs is 98° which is slightly smaller than the corresponding edge-shared In-In angles, 99-101°, in c-In_2O_3. For a-In-O and all a-In-X-O, the average edge-shared In-M coordination saturates at ~3.9 Å, as expected from the In-M distance distribution function. Comparing the values at the saturation, we find that all X cations increase the edge-shared In-M coordination, namely, from 1.62 for a-In-O to 1.66 in a-ITO, to 2.07 in a-IZO, to 2.11 in a-IGeO, and to 2.25 in a-IGaO. The improved edge-shared In-M coordination in a-In-X-O does not translate into better mobility: the observed mobility in a-In-X-O, X=Zn, Ga, or Sn, decreases as the substitutional fraction of X increases (see Section 4.2.3). Indeed, from the structural analyses of several a-In-O structures – obtained both theoretically (modelled via different cooling rates in MD simulations) and experimentally (deposited at different temperatures and characterized by EXAFS) – a seemingly counterintuitive conclusion was reached: the observed mobility peak corresponds to the structure with the *smallest* edge-shared In-In coordination number [147].

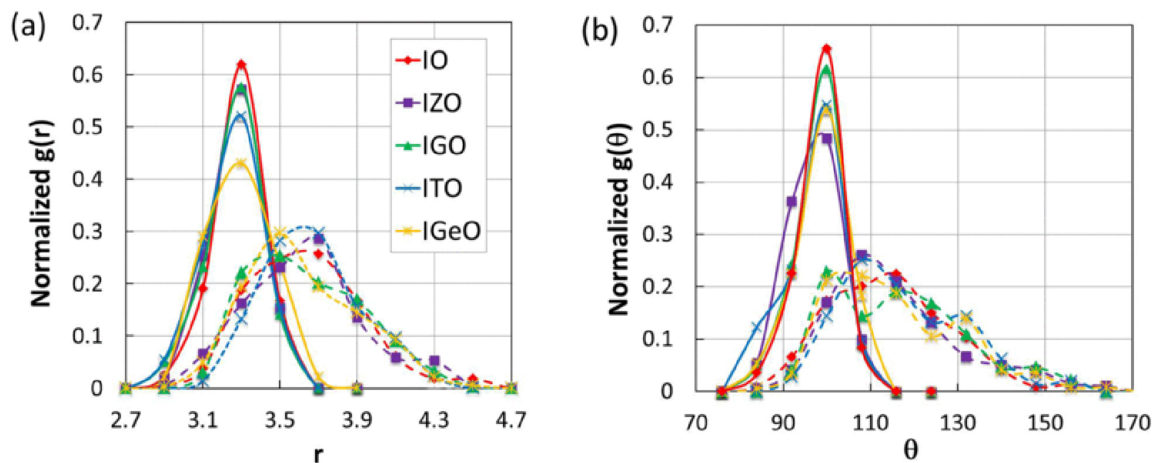

Figure 7. (Color online) (a) Normalized In-M distance distribution functions, g(r), calculated as a function of radial distance r from a central In atom, in Å, for edge-shared (solid line) and corner-shared (dash line) In-M pairs in amorphous In-O and In-X-O. (b) Normalized In-O-M angle distribution functions, $g(\theta)$, calculated for edge-shared (solid line) and corner-shared (dash line) In-M pairs.

(2) The *corner-shared* In-M distribution function is almost two times wider compared to the edge-shared one and begins at around 3.0 Å. Such significant overlap between the two distribution functions, Fig. 7, highlights the challenge to distinguish between the second and third shells from a general pair distribution function, whether it is obtained experimentally or theoretically. The average corner-shared In-M distance is about 3.6 Å for all a-In-X-O structures which is smaller than the crystalline corner-shared In-In distance of 3.8 Å. Consequently, the corresponding angle distribution for the corner-shared In-M pairs is wide and also overlaps with the angle values for the edge-shared In-M pairs, Fig. 7. The average In-O-M angle for the corner-shared In-M pairs is 116° for a-IXO, to be compared to 126° in c-In_2O_3.

The average edge/corner-shared In-M distance and In-O-M angle do not reveal significant differences between a-In-X-O, Fig. 7. The effect of composition becomes pronounced once the corresponding values are calculated separately for In-In, In-X, and X-X pairs. Moreover, following recent findings [147] on the importance of the connectivity of six-coordinated In atoms, denoted below as In_6, the average distances and angles for

edge and corner-shared In_6-In_6 pairs are also calculated and compared with those for the In-In pairs of all coordinations.

In-In: First, the average In-In values are calculated independent of the In coordination with oxygen atoms, i.e., for any two In atoms that are connected via edge- or corner-sharing. (Note, that In is primarily five-coordinated in a-In-O and in a-In-X-O except for a-IGeO, Fig. 4). The composition of ternary oxides does not change the relative number of the edge- *vs* corner-shared In-In pairs which remains nearly the same in a-In-O and all a-In-X-O, namely, 20% *vs* 80%, respectively, of the total shared In-In pairs in each oxide, Fig. 8(a). Moreover, the presence of X has little effect on the average edge-shared In-In distance as compared to the corresponding values in a-In-O, Fig. 8(c). In a-ITO, the shortest average edge-shared In-In distance (3.25 Å) may be due to the abundance and clustering of SnO_6 polyhedra (see Section 4.2.3); whereas in a-IGeO, the longest edge-shared In-In distance (3.33 Å) is likely to be due to the large number of In_6 (c.f., Fig. 4). The average corner-shared In-In distance increases slightly in all a-In-X-O, Fig. 8(d).

In_6-In_6: Most strikingly, the distances, angles, and connectivity between the naturally-coordinated In atoms vary significantly with composition of a-In-X-O. For X=Zn, Ga, or Ge, the number of In_6 increases, whereas Sn does not affect it, Fig. 4. However, all X cations modify the way the InO_6 polyhedra connect with each other. The relative number of edge- vs corner-shared In_6-In_6 pairs, shown in Fig. 8(b), is different in a-In-X-O – in contrast to the corresponding numbers of the shared In-In pairs, Fig. 8(a). Specifically, although Sn has little effect on the fractional number of In_6, Fig. 4, it suppresses the number of edge-shared InO_6 polyhedra, Fig. 8(b). At the same time, Sn leads to the formation of short-distant edge-shared In_6 pairs (~3.1 Å); the average corner-shared In_6-In_6 is also reduced in a-ITO as compared to a-In-O, resulting in the smallest average distance between the connected In_6-In_6 among the amorphous oxides considered. On the contrary, addition of Zn results in the longest edge-shared In_6-In_6 distance (3.42 Å) that is larger than that for the second shell in the crystalline In_2O_3, Fig. 8(c). Moreover, only in a-IZO, the number

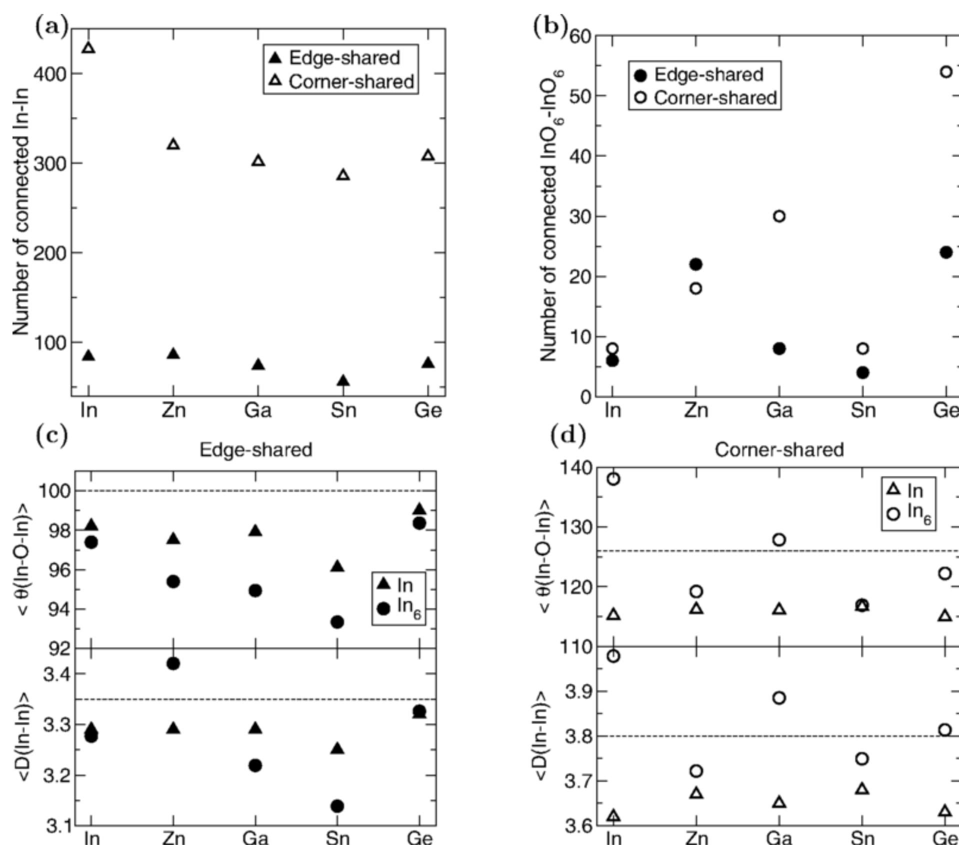

Figure 8. Number of edge-shared and corner-shared (a) In-In pairs and (b) In_6-In_6 pairs in amorphous In-O and In-X-O. Average In-In (triangle) or In_6-In_6 (circle) distance, in Å, and average In-O-In (triangle) or In_6-O-In_6 (circle) angle, in degrees, for the InO_x or InO_6 polyhedra connected via (c) edge-sharing or (d) corner-sharing in amorphous In-O and In-X-O. The horizontal dash line represents the corresponding values averaged for the second and third shells in crystalline In_2O_3.

of edge-shared InO_6 polyhedra is greater than that for the corner-shared InO_6, Fig. 8(b). Comparing a-IZO and a-IGO, the difference in the effect of composition on the InO_6 connectivity is manifested most clearly. In these oxides, the relative number of In_6 is nearly the same (and is doubled as compared to a-In-O and a-ITO, Fig. 4); the number of connected InO_6 polyhedra increases accordingly. However, Zn promotes edge-sharing between the InO_6 polyhedra whereas Ga favors their corner-sharing, Fig. 8. As a result, a-IZO (a-IGO) exhibits the longest edge-shared (corner-shared) In_6-In_6 distance for the connected InO_6 polyhedra among all a-In-X-O considered. Such differences in the InO_6 connectivity are

likely to reflect differences in the charge transport in a-IZO and a-IGO. The spatial distribution of InO_6 polyhedra will be discussed in the next section. Finally, Ge addition results in the largest number of InO_6 polyhedra, Fig. 4, so that the edge-shared distances and angles for In-In and In_6-In_6 pairs are nearly identical and are closest to the corresponding average edge-shared values in c-In_2O_3, 3.35 Å and 100°. The average corner-shared In_6-In_6 distance also matches that in c-In_2O_3. We note that the the proximity of the average In-In distance to that in c-In_2O_3 may serve as a signature of a large fraction of InO_6 polyhedra and may point out to a low effectiveness of Ge addition to amorphize indium oxide.

In-X: The connectivity between the InO_x and XO_x polyhedra is represented by the number of the edge- *vs* corner-shared In-X pairs and that is affected by the X preferred coordination discussed in Section 4.1.4 above. In particular, we find that most of the Sn and Ge atoms are six-coordinated with oxygen atoms that matches well with the framework InO_x polyhedra. Accordingly, the number of the edge- *vs* corner-shared In-X pairs does not change in a-ITO and a-IGeO and remains at 20% *vs* 80% which is similar to the corresponding ratio for In-In pairs. In marked contrast to Sn or Ge, Zn suppresses the edge-shared In-Zn number to as low as 6%. Most of the Zn atoms in a-IZO satisfy their natural coordination with oxygen atoms and, hence, such ZnO_4 polyhedra prefer only corner-sharing with nearby polyhedra (as indeed, found in crystalline ZnO and In_2ZnO_4). In a-IGO, about a half of the Ga atoms are five-coordinated which is not the natural coordination for binary Ga_2O_3 but can be found in ternary and quaternary oxides. In amorphous structure, such five-coordinated Ga atom can either share an additional oxygen atom (to become nearly six-coordinated) or let one of them loose (to become nearly four-coordinated). Both cases favor edge-sharing with neighboring polyhedra. Indeed, Ga increases the number of the edge-shared In-Ga up to 30%.

X-X: The preference for the natural X-X distances, X-O-X angles, and sharing between XO_x polyhedra is evident from Figure 9: no edge-shared Zn-Zn or Ge-Ge pairs are found in a-IZO and a-IGeO, in agreement with 100 % corner-sharing in crystalline

binary (wurtzite ZnO and cristobalite GeO_2) as well as ternary (In_2ZnO_4 and $In_2Ge_2O_7$) oxides. Moreover, the average corner-shared X-X distances and X-O-X angles in a-IZO and a-IGeO, Fig. 9, follow those in the crystalline binary oxides, namely 3.23 Å and 110° in wurtzite ZnO or 3.43 Å and 130° in rutile GeO_2. Similarly, Sn and Ga attain their preferred distances, angles, and polyhedra sharing in the a-In-X-O: in marked contrast to Zn and Ge, both Sn and Ga favor edge sharing leading to an increased number the edge-shared X-X pairs to 36 % and to 67 %, respectively, of the total number of the shared X-X pairs. (For comparison, as mentioned above, the number of the edge-shared In-In pairs does not exceed 20 % in a-In-O and a-In-X-O). Consequently, the average edge-shared Ga-Ga distance (3.02 Å) and the average edge-shared Ga-O-Ga angle (97.8^o) in a-IGO are close to those in crystalline β-Ga_2O_3, 3.08 Å and 98.6^o. Similarly, the average corner-shared Sn-Sn distance (3.72 Å) and the average corner-shared Sn-O-Sn angle (127.0^o) in a-ITO nearly match those in crystalline SnO_2, 3.71 Å and 129.3^o. The minority edge-shared Sn-Sn values are 3.33 Å and 102.8^o which are comparable to 3.19 Å and 101.5^o in c-SnO_2.

Thus, at 20 % fractional substitution of indium atoms with X, XO_x polyhedra show a strong preference to connect with each other in the way they do in the crystalline binary counterparts. This finding suggests that the spatial distribution of the XO_x polyhedra is an important issue from the points of view of (1) amorphization, e.g., formation of nanocrystalline inclusions; and (2) electron mobility governed by charge scattering, as will be discussed in the next section. It should be stressed that oxygen non-stoichiometry may affect the coordination of both In and X atoms and, therefore, may modify the interconnectivity and spatial distribution of the InO_x and XO_x polyhedra.

4.2.3. InO_6 and XO_x spatial distribution. As mentioned in the Introduction, the size and distribution of nanocrystalline In_2O_3 inclusions which are present in the amorphous oxide samples even below the transition to the so-called X-ray amorphous state of indium oxide, limit the transport properties via scattering [147]. In Figure 4, Section 4.1.3, the relative number of fully-coordinated In atoms are given for a-In-O and a-In-X-O, and their

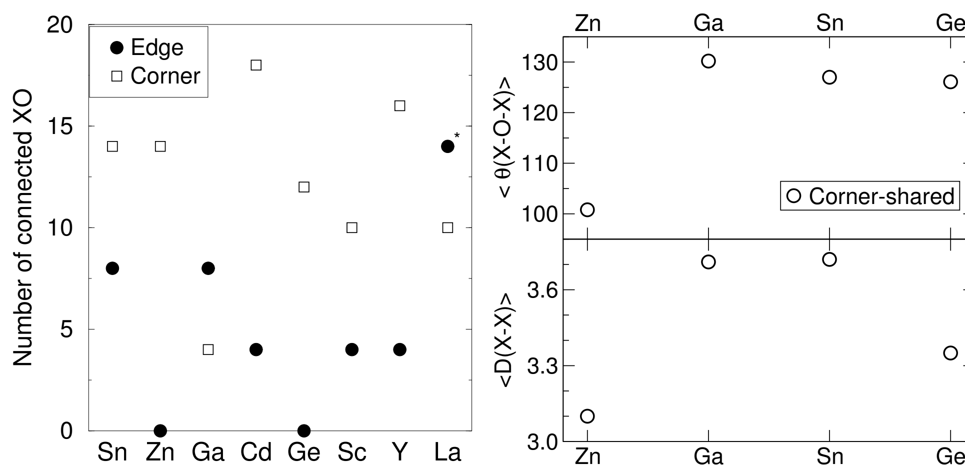

Figure 9. (Left) Number of edge-shared and corner-shared X-X pairs in a-In-X-O. (Right) Average X-X distance, in Å, and average X-O-X angle, in degrees, for the XO_x polyhedra connected via corner-sharing in amorphous In-X-O. The corresponding values for edge-shared X-X pairs for X=Sn and Ga are given in the text.

connectivity via edge- *vs* corner-sharing is discussed in the previous section. However, the spatial distribution of the InO_6, i.e., homogeneous distribution of separate-standing (not connected) polyhedra *vs* chains *vs* clusters, ultimately determines the properties [147] and should be addressed. The spatial behavior of XO_x polyhedra plays as important role and is also discussed below. In this work, the MD quench rates employed for a-In-O and a-In-X-O (170 K/ps) are expected to be fast enough to prevent InO_6 clustering and, hence, to avoid nucleation of In_2O_3 nanocrystallites observed in amorphous structures obtained at 5K/ps rates [147]. Indeed, in a-In-O obtained at this cooling rate, only 13% of In atoms are six-coordinated, and these InO_6 are distributed uniformly throughout the cell volume: the number of connected InO_6 (via edge or corner-sharing) is small, Fig. 8, and the average distance between shared InO_6 polyhedra is 3.68 Å which is greater than the average shared In-In distance in c-In_2O_3, 3.6 Å. The latter is primarily due to the presence of long-distance corner-shared In_6-In_6 pairs that result in the average corner-shared In_6-O-In_6 angle of 138°, Fig. 8 (to compare, the average corner-shared In-O-In angle in c-In_2O_3 is 126°). All X

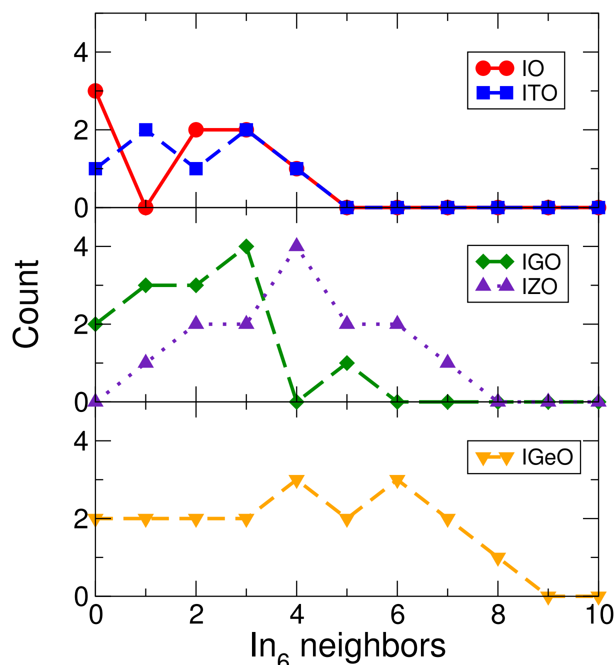

Figure 10. (Color online) The number of In_6 neighbors calculated within a radial cut-off distance of 3.8 Å from a central In_6 in a-In-O and a-In-X-O. The oxides are grouped according to the fractional number of the six-coordinated In atoms, c.f., Fig. 4, that is ~20 % for a-In-O, and a-ITO; ~30 % for a-IGO, and a-IZO; and ~40 % for a-IGeO.

cations considered in this work reduce the average corner-shared In_6-In_6 distance in a-In-X-O as compared to that in a-In-O, Fig. 8(d). This finding may point to a suppressed connectivity between the InO_6 polyhedra. Since the decrease does not follow the trend in the fractional number of In_6 (c.f., Fig. 4), different composition-dependent mechanisms should be responsible for the formation of the amorphous oxide structure, e.g., a tendency toward InO_6 clustering may be expected in some a-In-X-O. To analyse this, the number of In_6 neighbours to a central In_6 was calculated within a radial cut-off distance of 3.8 Å. (Note that oxygen sharing, i.e., connectivity between the InO_6 polyhedra, was not taken into account in these calculations, and the distance of 3.8 Å is simply to include the In-In distance of the second and third shells in c-In_2O_3). The results are grouped according to the fractional number of six-coordinated In atoms in different compounds (c.f., Fig. 4) for comparison. We find that addition of Sn reduces the probability of a single-standing

InO_6 polyhedra (i.e., not connected with another InO_6) as compared to a-In-O, Fig 10. Addition of Zn completely suppresses isolated InO_6 polyhedra in a-IZO. Comparing a-IGO and a-IZO where the fractional number of In_6 atoms is the same (about 30 %, Fig. 4), the different spatial distribution of the InO_6 polyhedra in these oxides is apparent, Fig. 10. In a-IGO, the In_6 atoms have primarily no, one, two or three In_6 neighbors; a single cluster of five InO_6 neighbors is observed. In contrast, a-IZO has a bell-shape distribution of the In_6 neighbors with four In_6 neighbors to be the most likely arrangement, Fig. 10. Such preferential distribution of the six-coordinate In atoms in a-IZO is likely due to the strong tendency of Zn to facilitate edge-sharing between the In_6 atoms, Fig. 8(b), thus forming long continuous chains of shared InO_6 polyhedra in a-IZO. Finally, the number of InO_6 is largest in a-IGeO, Fig. 4, and the probability to find an In_6 cluster of any size (no or 1 to 8 neighbors) is nearly the same in a-IGeO. This indifference to the In_6 cluster size in a-IGeO may arise from the smallest ionic radius of Ge among the X atoms considered, and signify inability of Ge addition to amorphize In-based oxides. We must stress here that the role of oxygen-non-stoichiometry and deposition temperatures (or cooling rates) on the structural properties of a-In-X-O was not taken into account in this work. Such investigations are ongoing and are expected to elaborate the effect of X addition. In ternary In-based amorphous oxides, the spatial distribution and connectivity of XO_x polyhedra are expected to have a greater effect on the charge scattering than the distribution of InO_6 polyhedra discussed above. The strong tendency of X atoms toward their natural distances in first, second, and third shells as well as toward the type of sharing between the XO_x polyhedra have been demonstrated in Section 4.1.2. At 20 % fractional substitution, we observe that the number of shared XO_x polyhedra correlates with the X ionic radius: for X=Zn, Ga, or Ge with smaller ionic radii there are 12-14 X-X connections per cell, whereas for the larger Sn addition, the total number of Sn-Sn connections increases to 22, Fig. 9. Although the number of connected XO_x polyhedra is similar in amorphous IZO, IGO, and IGeO, the strong preference for edge-sharing between the GaO_x polyhedra leads to

the formation of GaO_x clusters in a-IGO – in marked contrast to a more homogeneous distribution of ZnO_x and GeO_x polyhedra in the respective oxides, as discussed in the next Section. Most strikingly, a-ITO features significant SnO_x clustering having eight SnO_6 polyhedra connected via edge-sharing with the rest of the SnO_6 polyhedra attached to the cluster via corner-sharing. This finding may be explained by the large Sn ionic size and its strong ability to attain full coordination with oxygen atoms as compared to more distortion-tolerant In atoms. This finding resembles the structural characteristics of crystalline $In_4Sn_3O_{12}$ where a fraction of Sn atoms form regular SnO_6 polyhedra, whereas the rest of the Sn atoms and all In atoms have a low symmetry coordination with the In/Sn-O distances ranging from 2.07 Å to 2.31 Å. Thus, Sn addition may help attain amorphous In-based oxide structure by distorting the InO_x polyhedra and, hence, may help prevent InO_6 clustering with subsequent formation of In_2O_3 nanocrystallites. On the other hand, Sn has a strong tendency to cluster itself which ultimately limits the electron mobility as the fraction of Sn increases. Indeed, among the PLD-grown amorphous In-X-O with X=Zn, Ga, and Sn, the observed carrier mobility of a-ITO is highest only up to about 10% of the Sn fractional substitution, Fig. 11. The mobility drops significantly for larger Sn fraction, and above 15% becomes lower than that in a-IZO where no Zn clustering was found from the MD simulations. A similar behavior of the carrier mobility is observed in a-IGO where a change in the slope occurs at about 20 % of Ga substitution for In, Fig. 11, signifying a stronger scattering possibly associated with an onset of GaO_x clustering that was found in our MD-simulated a-IGO structure. The linear decrease of the carrier mobility with Zn fractional substitution is in accord with the proposed uniform distribution of ZnO_x throughout the InO_x framework.

4.3. Structural models of amorphous In-X-O. The above comparison of the local and long-range structural characteristics of amorphous In-X-O points to the substantial differences between the oxides that originate from the different ionic size, valence, metal-oxygen bond strength, and oxygen-sharing preferences of the cations. To illustrate the

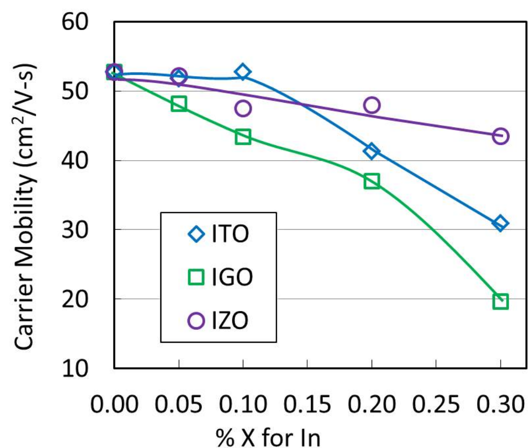

Figure 11. (Color online) Observed Hall mobility in PLD-grown amorphous In-X-O, X=Zn, Ga, or Sn, as a function of fractional substitution.

different structural behavior in the amorphous In-X-O oxides, their atomic structures are presented in Fig. 12 where both the InO_6 and XO_x polyhedra are highlighted. Based on the results of MD simulations, we propose the following structural models of amorphous In-X-O that help explain the observed transport properties in these oxides (Fig. 11).

In *a-IZO*, Zn exhibits both longer and shorter than the natural Zn-O distances resulting in a wide Zn-O pair distribution. This points out the ability of Zn to adopt to the distortions of amorphous environment – a property that is advantageous in the oxides under strain. Addition of Zn increases the coordination of In atoms located away from Zn and strongly favors edge-sharing between InO_6 polyhedra. The latter form long connected chains that serve as conductivity paths, Figure 12. At the same time, Zn maintains its tetrahedral coordination with oxygen that ensures corner-sharing of ZnO_x polyhedra and facilitates a uniform distribution of the ZnO_x polyhedra throughout the InO_x framework, Figure 12. Absence of ZnO_x clustering mitigates charge scattering in a-IZO, in accord with the measured linear dependence of the mobility with Zn fractional substitution, Fig. 11. Hence, the long chain network of InO_6 supported by ZnO_4 gives rise to the excellent carrier mobility observed in a-IZO.

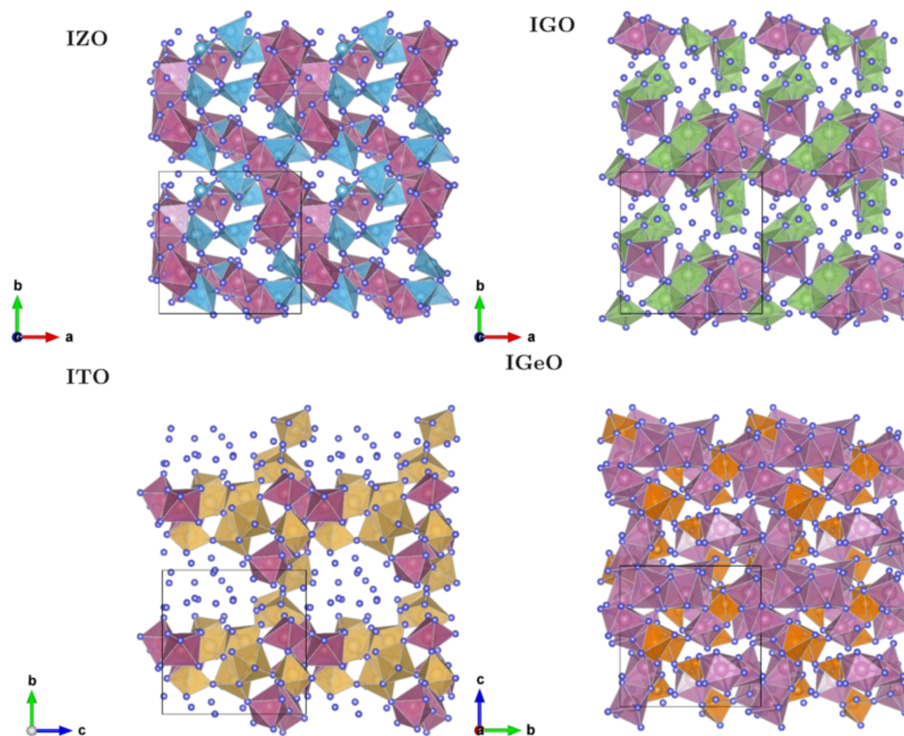

Figure 12. (Color online) Atomic structures of a-In-X-O, X=Zn, Ga, Sn, or Ge, highlighting the InO_6 and XO_x polyhedra only. Small spheres represent oxygen atoms, and large spheres represent In or X atoms.

In *a-ITO*, addition of Sn does not affect the InO_x coordination statistics, in agreement with the unchanged carrier concentration of a-ITO at 30% Sn substitution as compared to the one observed for a-In-O (1.6×10^{20} cm^{-3} for both cases). Moreover, presence of Sn does not affect the spatial distribution and sharing between the InO_6 polyhedra as compared to a-In-O. At the same time, Sn satisfies its natural distances and coordination with oxygen. Strikingly, these SnO_6 polyhedra fill the space between disconnected InO_6 polyhedra, and together they form a distinct network of long connected chains, Figure 12. Given the electronic similarities between the six-coordinate In and Sn ions, such InO_6-SnO_6 chains are expected to serve as conductivity paths for good charge transport. Indeed, the carrier mobility remains constant in a-ITO up to 10% Sn fractional substitution, Fig. 11. At larger Sn concentrations, the strong tendency of Sn to cluster causes electron scattering so that the carrier mobility decreases rapidly above 10% Sn fractional substitution in a-ITO.

In *a-IGO*, Ga cations, on average, satisfy their natural coordination with oxygen, adopting a four-, five- or six-fold local oxygen environment. As a result of the sustained multi-coordination, Ga suppresses the number of low-coordinated In atoms in a-IGO which may explain the largest reduction of the observed carrier concentration with fractional Ga substitution as compared to a-ITO and a-IZO. Addition of Ga triples the number of corner-shared InO_6 polyhedra and has no effect on the number of edge-shared In_6 pairs. Hence, Ga helps prevent growth of nanocrystalline In_2O_3 inclusions that makes Ga cation an effective candidate for amorphization of indium oxide. However, the absence of extended InO_6 chains along with a strong charge scattering associated with clusters of the edge-shared GaO_x polyhedra, Figure 12, is expected to limit the electron transport in a-IGO as the Ga fractional substitution increases.

In *a-IGeO*, owing to the strong Ge-O bonds, the average Ge-O distance and Ge coordination with oxygen remain at their natural values. Ge nearly triples the fractional number of six-coordinated indium atoms as compared to the a-In-O and increases the average distance between edge- and corner-shared In_6 pairs to nearly crystalline In_2O_3 values. Hence, Ge addition facilitates the formation and growth of nanocrystalline indium oxide and is likely to limit the ability of a-IGeO to generate carriers.

5. CONCLUSIONS

The results of *ab-initio* molecular-dynamics liquid-quench simulations of ternary In-based amorphous oxides, a-In-X-O with X=Sn, Zn, Ga, or Ge, reveal that an interplay between the local and long-range structural preferences of the constituent oxides gives rise to a complex composition-dependent behavior in these multicomponent materials. More specifically, it is found that the local structure of the MO_x polyhedra remains, on average, nearly unchanged upon the transition from crystalline to amorphous state. Moreover, the average In-O coordination is 5.0-5.2 in a-In-O and all a-In-X-O considered in this

work. Such a weak dependence of the In coordination on the composition signifies that In atoms remain to serve as a main source of oxygen defects upon fractional substitution with X. This is in accord with a similar carrier concentration measured for amorphous In-O (1.6×10^{20} cm^{-3}) and for In-X-O at 30% substitution with X=Ga, Zn, or Sn (0.8, 1.2, or 1.6×10^{20} cm^{-3}, respectively). Hence, in marked contrast to crystalline transparent conducting oxides, the additional cations in amorphous oxides do not serve as dopants and do not govern the carrier generation directly. At the same time, composition-induced differences in the connectivity and spatial distribution of InO_6 and XO_x polyhedra determine the formation of the amorphous structures as well as the carrier mobility which is controlled by electron scattering. Based on the structural results of the MD simulations, the proposed composition-dependent models of amorphous oxide network help explain the observed electrical properties in amorphous In-O-X. These systematic results shed light on the role of composition in tuning the properties of amorphous oxides and facilitate the progress in fundamental understanding of amorphous transparent conducting oxides.

6. ACKOWLEDGMENTS

The work was performed under the collaborative MRSEC program at Northwestern University and supported by the National Science Foundation (NSF) grant DMR-1121262. Computational resources are provided by the NSF-supported XSEDE program.

SECTION

3. CONCLUSIONS

In this dissertation, we have systematically investigated the dependence of structure and properties of amorphous indium-based oxides on cooling rates and the cation composition. *Ab initio* molecular dynamics with the method of liquid quench simulation were used to model amorphous structure.

Experimentally, the size of the nanocrystalline In_2O_3 inclusions was shown to depend on the deposition temperature used to grow the samples. These nanocrystalline inclusions limit the electron transport via scattering. MD simulation showed the nucleation of such nanocrystallites in the structure obtained by using a slow cooling rate, revealing the dependence on the quench rates for the spatial distribution and interconnectivity of the naturally coordinate indium atoms, i.e., InO_6-polyhedra. Based on a precise comparison of experimental and theoretical results, we have concluded that the medium-range structural characteristics of the amorphous structure, or in other words, the way metal-oxygen polyhedra are distributed into a continuous network, play a fundamental role in the transport properties of amorphous oxides.

Next, the study performed for amorphous ternary indium-based oxides, In-X-O, showed that indium retains its average coordination of 5 upon 20% X partial substitution for In. At the same time, X cation substitution is found to satisfy their natural coordination, suggesting that under-coordinated indium atoms serve as a possible source of carriers in indium-based ternary oxides. Moreover, the presence of X was found to affect the number of six-coordinated indium atoms and the oxygen sharing between them and hence the transport behavior such as Hall mobility. An explicit study carried out by taking three cations Sc, Y, and La of different atomic radius, indicates that the effects of X on the structural properties

of the host InO framework depend on the cationic size of the incorporated X atom. Indeed, this influences the amorphousness of the structure and the formation of different defect states in the electronic band structure.

In summary, we explained the structural changes and their effect on the transport properties that take place near the transition from crystalline to amorphous state or introduced via chemical composition. However, many interesting questions remain. Device performance of semiconductors depends on surface states. It would be interesting to investigate how structural, electronic, and electrical properties are affected by surfaces and interfaces of amorphous transparent oxides. As mentioned in the Introduction, amorphous oxides are flexible, allowing for a bending without significant loss in optical and electrical properties. The role of composition could be studied to identify candidate cations that are most efficient in absorbing the lattice stress caused by strain to improve the mechanical property. Furthermore, the effect of transition metals such as Fe, Mn, Cr could expand the area of amorphous transparent conducting oxide with tunable properties and broader application, e.g., memory devices. Also, the problem of tackling large system sizes with the technique we have used, *ab initio* molecular dynamics, could be compensated by combining it with other techniques like activation-relaxation or classical molecular dynamics. These techniques are computationally not very demanding allowing one to have longer simulation with system size of the order of thousands of atoms to study the nucleation of inclusions and grain formation.

BIBLIOGRAPHY

[1] A. Facchetti and T. Marks. *Transparent Electronics: From Synthesis to Applications*. John Wiley & Sons, New York, 2010.

[2] K. L. Chopra, S. Major, and D. K. Pandya. Transparent conductors – a status review. *Thin Solid Films*, 102:1–46, 1983.

[3] A. L. Dawar and J. C. Joshi. Semiconducting transparent thin films: their properties and applications. *J. Mater. Sci.*, 19:1–23, 1984.

[4] H. L. Hartnagel, A. L. Dawar, A. K. Jain, and C. Jagadish. *Semiconducting Transparent Thin Films*. Institute of Physics Publishing, London, 1995.

[5] D. S. Ginley and C. Bright. Special issue on transparent conducting oxides. *MRS Bull.*, 25:15–18, 2000.

[6] R. L. Weiher and R. P. Ley. Optical properties of indium oxide. *J. Appl. Phys*, 37:299–302, 1966.

[7] C. Kligshirn. The luminescence of ZnO under high one- and two-quantum excitation. *Phys. Status Solidi B*, 71:547, 1975.

[8] F. P. Koffyberg. Thermoreflectance spectra of CdO: Band gaps and band-population effects. *Phys. Rev. B*, 13:4470–4476, 1976.

[9] D. Fröhlich, R. Kenklies, and R. Helbig. Band-gap assignment in sno_2 by two-photon spectroscopy. *Phys. Rev. Lett.*, 41:1750–1751, Dec 1978.

[10] M. Mohamed, I. Unger, C. Janowitz, R. Manzke, Z. Galazka, R. Uecker, and R. Fornari. The surface band structure of β-Ga_2O_3. *Journal of Physics: Conference Series*, 286(1):012027, 2011.

[11] H. Schmidt, F. Giustiniano, and G. Eda. Electronic transport properties of transition metal dichalcogenide field-effect devices: surface and interface effects. *Chem. Soc. Rev.*, 44:7715–7736, 2015.

[12] Z. Li, Z. Liu, H. Sun, and C. Gao. Superstructured assembly of nanocarbons: Fullerenes, nanotubes, and graphene. *Chem. Rev.*, 115(15):7046–7117, 2015.

[13] X. Yu, T. J. Marks, and A. Facchetti. Metal oxides for optoelectronic applications. *Nat Mater*, 15(4):383–396, 04 2016.

[14] D. A. Drabold and S. K. Estreicher. *Theory of defects in semiconductors*. Springer-Verlag, Berlin Heidelberg, 2007.

[15] T. B. Reed. *Free energy of formation of binary compounds*. MIT Press, Cambridge, Massachusetts, 1971.

[16] F. A. Kröger. *The Chemistry of Imperfect Crystals*. North-Holland, Amsterdam, 1974.

[17] J. H.W. de Wit, G. van Unen, and M. Lahey. Electron concentration and mobility in In_2O_3. *J. Phys. Chem. Solids*, 38:819–824, 1977.

[18] S. Lany and A. Zunger. Dopability, intrinsic conductivity and nonstoichiometry of transparent conducting oxides. *Phys. Rev. Lett.*, 98:045501, 2007.

[19] T. J. Coutts, D. L. Young, and X. Li. Characterization of transparent conducting oxides. *MRS Bull.*, 25:58–65, 2000.

[20] P. Ponte Castaneda and M. Kailasam. Nonlinear electrical conductivity in heterogeneous media. *Proceedings: Math., Phys. and Eng. Sci.*, 453(1959):793–816, 1997.

[21] A. J. Freeman, K. R. Poeppelmeier, T. O. Mason, R. P.H. Chang, and T. J. Marks. Chemical and thin-film strategies for new transparent conducting oxides. *MRS Bull.*, 25:45–51, 2000.

[22] O. N. Mryasov and A. J. Freeman. Electronic band structure of indium tin oxide and criteria for transparent conducting behavior. *Phys. Rev. B*, 64:233111, 2001.

[23] Ç. Kiliç and A. Zunger. Origins of coexistence of conductivity and transparency in SnO_2. *Phys. Rev. Lett.*, 88:95501, 2002.

[24] J. E. Medvedeva and A. J. Freeman. Combining high conductivity with complete optical transparency: A band-structure approach. *Europhys. Lett.*, 69:583–587, 2005.

[25] J. E. Medvedeva. *in Transparent Electronics: From Synthesis to Applications*, pages 1–29. John Wiley & Sons, 2010.

[26] T. S. Moss. The interpretation of the properties of indium antimonide. *Proc. Phys. Soc. B*, 67:775–782, 1954.

[27] E. Burstein. Anomalous optical absorption limit in InSb. *Phys. Rev.*, 93:632–633, 1954.

[28] E. Fortunato, P. Barquinha, and R. Martins. Oxide semiconductor thin-film transistors: A review of recent advances. *Adv. Mater.*, 24(22):2945–2986, 2012.

[29] E.P. Denton, H. Rawson, and J.E. Stanworth. Vanadate Glasses. *nat*, 173:1030–1032, May 1954.

[30] H. Hosono. Ionic amorphous oxide semiconductors: design, carrier transport, and device application. *J. Non-Cryst. Solids*, 352:851, 2006.

[31] K. Ito, T. Nakazawa, and K. Osaki. Amorphous-to-crystalline transition of indium oxide films deposited by reactive evaporation. *Thin Solid Films*, 151(2):215 – 222, 1987.

[32] J.R. Bellingham, W.A. Phillips, and C.J. Adkins. Electrical and optical properties of amorphous indium oxide. *J. Phys.: Condens. Matter. Sci. Lett*, 2:6207–6221, 1990.

[33] H. Hosono, N. Kikuchi, N. Ueda, H. Kawazoe, and K. Shimidzu. Amorphous transparent electroconductor $2CdO.GeO_2$: Conversion of amorphous insulating cadmium germanate by ion implantation. *Appl. Phys. Lett.*, 67(18):2663–2665, 1995.

[34] N. Kikuchi, H. Hosono, H. Kawazoe, K. Oyoshi, and S. Hishita. Transparent, conducting, amorphous oxides: Effect of chemical composition on electrical and optical properties of cadmium germanates. *J. Am. Ceram. Soc.*, 80(1):22–26, 1997.

[35] M. Yasukawa, H. Hosono, N. Ueda, and H. Kawazoe. Novel transparent and electroconductive amorphous semiconductor: Amorphous $AgSbO_3$ film. *Jpn. J. Appl. Phys.*, 34(3A):L281, 1995.

[36] M. Orita, H. Ohta, M. Hirano, S. Narushima, and H. Hosono. Amorphous transparent conductive oxide $InGaO_3(ZnO)_{(m)}$ ($m \leq 4$): a Zn4s conductor. *Phil. Mag. B*, 81:501–515, 2001.

[37] H. Hosono, Y. Yamashita, N. Ueda, H. Kawazoe, and K.-I. Shimidzu. New amorphous semiconductor: $2CdO.PbO_x$. *Appl. Phys. Lett.*, 68(5):661–663, 1996.

[38] H. Hosono, H. Un'no, N. Ueda, H. Kawazoe, N. Matsunami, and H. Tanoue. Conversion of insulating thin films of $MgIn_2O_4$ into transparent conductors by ion implantation. *Nuclear Instruments and Methods in Physics Research Section B: Beam Interactions with Materials and Atoms*, 106(1-4):517 – 521, 1995.

[39] John F. Wager, Douglas, and Rick E. Presley. *Transparent Electronics*. Springer, New York, 2008.

[40] H. Hosono, N. Kikuchi, H. Kawazoe, and N. Ueda. Working hypothesis to explore novel wide band-gap electrically conducting amorphous oxides and examples. *J. Non-Cryst. Solids*, 198-200:165 – 169, 1996.

[41] H. Hosono, M. Yasukawa, and H. Kawazoe. Novel oxide amorphous semiconductors: transparent conducting amorphous oxides. *J. Non-Cryst. Solids*, 203:334 – 344, 1996.

[42] K. Nomura, H. Ohta, A. Takagi, T. Kamiya, M. Hirano, and H. Hosono. Room temperature fabrication of transparent flexible thin-film transistors using amorphous oxide semiconductors. *Nature*, 432:488–492, 2004.

[43] D.C. Paine, T. Whitson, D. Janiac, R. Beresford, C.O. Yang, and B. Lewis. A study of low temperature crystallization of amorphous thin film indium-tin-oxide. *J. Appl. Phys.*, 85:8445–8450, 1999.

[44] G. GonÃğalves, E. Elangovan, P. Barquinha, L. Pereira, R. Martins, and E. Fortunato. Influence of post-annealing temperature on the properties exhibited by ITO, IZO and GZO thin films. *Thin Solid Films*, 515(24):8562 – 8566, 2007.

[45] T. Moriga, A. Fukushima, Y. Tominari, S. Hosokawa, I. Nakabayashi, and K. Tominaga. Crystallization process of transparent conductive oxides $Zn_kIn_2O_{k+3}$. *J. Synchrotron Radiat.*, 8:785–787, 2001.

[46] J. H. Park, D. Byun, and J. K. Lee. Structural and electrical characteristics of gallium tin oxide thin films prepared by electron cyclotron resonance-metal organic chemical vapor deposition. *J. Nanosci. Nanotechnol.*, 11(8):7234–7237, 2011.

[47] M. Ramzan, T. Kaewmaraya, and R. Ahuja. Molecular dynamics study of amorphous Ga-doped In_2O_3: A promising materials for phase change memory devices. *Appl. Phys. Lett.*, 103:072113, 2013.

[48] K. H. Ko, H. S. So, D. H. Jung, J. W. Park, and H. Lee. Spectroscopic ellipsometry-based study of optical properties of amorphous and crystalline ZnSnO alloys and Zn_2SnO_4 thin films grown using sputtering deposition: Dielectric function and subgap states. *J. Appl. Phys.*, 119(13), 2016.

[49] K. Nomura, T. Kamiya, H. Ohta, T. Uruga, M. Hirano, and H. Hosono. Local coordination structure and electronic structure of the large electron mobility amorphous oxide semiconductor In-Ga-Zn-O: Experiment and ab initio calculations. *Phys. Rev. B*, 75:035212, 2007.

[50] A. Walsh, J.L.F. Da Silva, and S.-H. Wei. Interplay between order and disorder in the high performance of amorphous transparent conducting oxides. *Chem. Mater.*, 21:5119–5124, 2009.

[51] D.-Y. Cho, Na.K.D. Jaewon Song, C.S. Hwang, J.H. Jeong, J.K Jeong, and Y.-G. Mo. Local structure and conduction mechanism in amorphous In-Ga-Zn-O films. *Appl. Phys. Lett.*, 94:112112–1(3), 2009.

[52] M. D. Heinemann, J. Berry, G. Teeter, T. Unold, and D. Ginley. Oxygen deficiency and Sn doping of amorphous Ga_2O_3. *Appl. Phys. Lett.*, 108(2), 2016.

[53] A. Thakur, H. Yoo, S. Kang, J. Y. Baik, I. Lee, H. Lee, K. Kim, B. Kim, S. Jung, J. Park, and H. Shin. Effects of substrate temperature on structural, electrical and optical properties of amorphous In-Ga-Zn-O thin films. *ECS J. Solid State Sci. Technol.*, 1(1):Q11–Q15, 2012.

[54] D.E. Proffit, Q. Ma, D.B Buchholz, R.P.H. Chang, M.J. Bedzyk, and T.O. Mason. Structural and physical property studies of amorphous Zn-In-Sn-O thin films. *J. Am. Ceram. Soc.*, 95:3657–3664, 2012.

[55] M. Kim, H. S. Kim, Y. Ha, J. He, M. G. Kanatzidis, A. Facchetti, and T. J. Marks. High-performance solution-processed amorphous zinc-indium-tin oxide thin-film transistors. *J. Am. Chem. Soc.*, 132(30):10352–10364, 2010.

[56] C.A. Hoel, S. Xie, C. Benmore, C.D. Malliakas, J.-F. Gaillard, and K.R. Poeppelmeier. Evidence for tetrahedral zinc in amorphous $In_{2-2x}Zn_xSn_xO_3$ (a-ZITO). *Z. Anorg. Allg. Chem.*, 637:885–894, 2011.

[57] C. Liang, J. L. H. Chau, C. Yang, and H. Shih. Preparation of amorphous Ga-Sn-Zn-O semiconductor thin films by rf-sputtering method. *Mater. Sci. Eng., B*, 183:17 – 23, 2014.

[58] D.S. Ginley, H. Hosono, and D.C. Paine. *Handbook of Transparent Conductors*. Springer, 2010.

[59] M. K. Ryu, S. Yang, S. K. Park, C. Hwang, and J. K. Jeong. High performance thin film transistor with cosputtered amorphous Zn-In-Sn-O channel: Combinatorial approach. *Appl. Phys. Lett.*, 95(7):–, 2009.

[60] X. Yu, L. Zeng, N. Zhou, P. Guo, F. Shi, D. B. Buchholz, Q. Ma, J. Yu, V. P. Dravid, R. P. H. Chang, M. Bedzyk, T. J. Marks, and A. Facchetti. Ultra-flexible, “invisible" thin-film transistors enabled by amorphous metal oxide/polymer channel layer blends. *Adv. Mater.*, 27(14):2390–2399, 2015.

[61] G. S. Chae. A modified transparent conducting oxide for flat panel displays only. *Jpn. J. Appl. Phys.*, 40(3R):1282, 2001.

[62] M. Ito, M. Kon, C. Miyazaki, N. Ikeda, M. Ishizaki, R. Matsubara, Y. Ugajin, and N. Sekine. Amorphous oxide tft and their applications in electrophoretic displays. *physica status solidi (a)*, 205(8):1885–1894, 2008.

[63] W. M. Kim, D. Y. Ku, I. Lee, Y. W. Seo, B. Cheong, T. S. Lee, I. K., and K. S. Lee. The electromagnetic interference shielding effect of indium-zinc oxide/silver alloy multilayered thin films. *Thin Solid Films*, 473(2):315–320, 2005.

[64] M. P. Taylor, D. W. Readey, M. F. A. M. van Hest, C. W. Teplin, J. L. Alleman, M. S. Dabney, L. M. Gedvilas, B. M. Keyes, B. To, J. D. Perkins, and D. S. Ginley. The remarkable thermal stability of amorphous In-Zn-O transparent conductors. *Adv. Funct. Mater.*, 18(20):3169–3178, 2008.

[65] K. Ide, K. Nomura, H. Hiramatsu, T. Kamiya, and H. Hosono. Structural relaxation in amorphous oxide semiconductor, a-In-Ga-Zn-O. *J. Appl. Phys.*, 111(7), 2012.

[66] A.I Taub and F Spaepen. The kinetics of structural relaxation of a metallic glass. *Acta Metall.*, 28(12):1781 – 1788, 1980.

[67] J. E. Medvedeva. Averaging of the electron effective mass in multicomponent transparent conducting oxides. *Europhys. Lett.*, 78:57004, 2007.

[68] J. Rosen and O. Warschkow. Electronic structure of amorphous indium oxide transparent conductors. *Phys. Rev. B*, 80:115215, 2009.

[69] J.D. Perkins, M.F.A.M. van Hest, C.W. Teplin, J.L. Alleman, M.S. Dabney, L.M. Gedvilas, B.M. Keyes, B. To, D.S. Ginley, M.P. Taylor, and D.W. Readey. Amorphous transparent conducting oxides (TCOs) deposited at t = 100^0c. In *Photovoltaic Energy Conversion, Conference Record of the 2006 IEEE 4th World Conference on*, volume 1, pages 202–204, May 2006.

[70] Ryo Endoh, Takayuki Hirano, Masaaki Takeda, Manabu Oishi, Nobuto Oka, and Yuzo Shigesato. Thermal conductivity of amorphous indium zinc oxide thin films. In *Symposium MM - Transparent Conducting Oxides and Applications*, volume 1315 of *MRS Proceedings*, pages mrsf10–1315–mm11–05, 2011.

[71] Y. Gassenbauer, R. Schafranek, A. Klein, S. Zafeiratos, M. Hävecker, A. Knop-Gericke, and R. Schlögl. Surface states, surface potentials, and segregation at surfaces of tin-doped In_2O_3. *Phys. Rev. B*, 73:245312, 2006.

[72] A. J. Meux, G P., J G., and P. Heremans. Comparison of the electronic structure of amorphous versus crystalline indium gallium zinc oxide semiconductor: structure, tail states and strain effects. *J. Phys. D: Appl. Phys.*, 48(43):435104, 2015.

[73] J. Singh and K. Shimakawa. *Advances in Amorphous Semiconductors*. Taylor & Francis, 2003.

[74] T. Kamiys, K. Nomura, and H. Hosono. Present status of amorphous In-Ga-Zn-O thin-film transistors. *Sci. Technol. Adv. Mater.*, 11:044305–044323, 2010.

[75] R L McGreevy. Reverse monte carlo modelling. *J. Phys.: Condens. Matter*, 13(46):R877, 2001.

[76] D. E. Polk and D. S. Boudreaux. Tetrahedrally coordinated random-network structure. *Phys. Rev. Lett.*, 31:92–95, Jul 1973.

[77] F. Wooten and D. Weaire. A computer-generated model of the crystalline/amorphous interface in silicon. *J. Non-Cryst. Solids*, 114, Part 2(0):681 – 683, 1989.

[78] G. Gutiérrez and B. Johansson. Molecular dynamics study of structural properties of amorphous Al_2O_3. *Phys. Rev. B*, 65:104202, Feb 2002.

[79] K. G. Gofryk, S. Du, C. R. Stanek, J. C. Lashley, X. Y. Liu, R. K. Schulze, J. L. Smith, D. J. Safarik, D. D. Byler, K. J. McClellan, B. P. Uberuaga, B. L. Scott, and D. A. Andersson. Anisotropic thermal conductivity in uranium dioxide. *Nat Commun*, 5:1–7, 2014.

[80] A. Arnold, N. Mauser, and J. Hafner. A molecular dynamics study of the structure of liquid germanium. *J Phys. Condens. Matter*, 11:965, 1989.

[81] A. Aliano, A. Catellani, and G. Cicero. Characterization of amorphous In_2O_3: An ab initio molecular dynamics study. *Appl. Phys. Lett.*, 99:211913, 2011.

[82] T. Kamiya and H. Hosono. Material characteristics and applications of transparent amorphous oxide semiconductors. *Asia Mater*, 2:15–22, 01 2010.

[83] K. Nomura, A. Takagi, T. Kamiya, H. Ohta, M. Hirano, and H. Hosono. Amorphous oxide semiconductors for high-performance flexible thin-film transistors. *Jpn. J. Appl. Phys*, 45:4303–4308, 2006.

[84] M. Kim, I.J. Kang, and C.H. Park. First-principle study of electronic structure of Sn-doped amorphous In_2O_3 and the role of O-deficiency. *Curr. Appl. Phys.*, 12:S25–S28, 2012.

[85] S. Sallis, K. T. Butler, N. F. Quackenbush, D. S. Williams, M. Junda, D. A. Fischer, J. C. Woicik, N. J. Podraza, B. E. White, A. Walsh, and L. F. J. Piper. Origin of deep subgap states in amorphous indium gallium zinc oxide: Chemically disordered coordination of oxygen. *Appl. Phys. Lett.*, 104(23):–, 2014.

[86] S. Sallis, N. F. Quackenbush, D. S. Williams, M. Senger, J. C. Woicik, B. E. White, and L. F. J. Piper. Deep subgap feature in amorphous indium gallium zinc oxide: Evidence against reduced indium. *Phys. Status Solidi (a)*, 212(7):1471–1475, 2015.

[87] K. Nomura, T. Kamiya, E. Ikenaga, H. Yanagi, K. Kobayashi, and H. Hosono. Depth analysis of subgap electronic states in amorphous oxide semiconductor, a-In-Ga-Zn-O, studied by hard x-ray photoelectron spectroscopy. *J. Appl. Phys.*, 109(7):–, 2011.

[88] T. Kamiya, K. Nomura, and H. Hosono. Origins of high mobility and low operation voltage of amorphous oxide tfts: Electronic structure, electron transport, defects and doping. *J. Display Technol.*, 5(7):273–288, 2009.

[89] H. Omura, H. Kumomi, K. Nomura, T. Kamiya, M. Hirano, and H. Hosono. First-principles study of native point defects in crystalline indium gallium zinc oxide. *J. Appl. Phys.*, 105:093712, 2009.

[90] T. Kamiya, K. Nomura, and H. Hosono. Subgap states, doping and defect formation energies in amorphous oxide semiconductor a-$InGaZnO_4$ studied by density functional theory. *phys. status solidi (a)*, 207(7):1698–1703, 2010.

[91] H.-K. Noh, K.J. Chang, B. Ryu, and W.-J. Lee. Electronic structure of oxygen-vacancy defects in amorphous In-Ga-Zn-O semiconductors. *Phys. Rev. B*, 84:115205, 2011.

[92] H. Nahm and Y. Kim. Undercoordinated indium as an intrinsic electron-trap center in amorphous $InGaZnO_4$. *NPG Asia Mater*, 6, 2014.

[93] W. Körner, D. F. Urban, and C. Elsässer. Generic origin of subgap states in transparent amorphous semiconductor oxides illustrated for the cases of In-Zn-O and In-Sn-O. *phys. status solidi (a)*, 212(7):1476–1481, 2015.

[94] K. Nomura, T. Kamiya, H. Yanagi, E. Ikenaga, and K. Yang. Subgap states in transparent amorphous oxide semiconductor, In-Ga-Zn-O, observed by bulk sensitive x-ray photoelectron spectroscopy. *Appl. Phys. Lett*, 92:202117, 2008.

[95] L. Yuan, G. Fang, X. Zou, H. Huang, H. Zou, X. Han, Yihua Gao, Sheng Xu, and Xingzhong Zhao. Optical and electrical characterization of a-InGaZnO thin film fabricated by pulsed laser deposition for thin film transistor applications. *J. Phys. D: Appl. Phys.*, 42(21):215301, 2009.

[96] N.Y. Yuan, S.Y. Wang, C.B. Tan, X.Q. Wang, G.G. Chen, and J.N. Ding. The influence of deposition temperature on growth mode, optical and mechanical properties of zno films prepared by the ALD method. *J. Cryst. Growth*, 366:43 – 46, 2013.

[97] X.F. Chen, G. He, J. Gao, J.W. Zhang, D.Q. Xiao, P. Jin, and B. Deng. Substrate temperature dependent structural, optical and electrical properties of amorphous InGaZnO thin films. *J. Alloys Compd.*, 632:533 – 539, 2015.

[98] N. Marzari. Realistic modeling of nanostructures using density functional theory. *MRS Bull.*, 31:681, 2006.

[99] E. Wimmer. Computational materials design: A perspective for atomistic approaches. *J. Comput. Aided Mater. Des.*, 1:215–242, 1994.

[100] R. M. Martin. *Electronic Structure: Basic Theory and Practical Methods*. Cambridge University Press, 2004.

[101] G. C. Kaphle, S. Ganguly, R. Banerjee, R. Banerjee, R. Khanal, C. M. Adhikari, N. P. Adhikari, and A. Mookerjee. A study of magnetism in disordered Pt-Mn, Pd-Mn and Ni-Mn alloys: an augmented space recursion approach. *J. Phys.: Condens. Matter*, 24(29):295501, 2012.

[102] P. Hohenberg and W. Kohn. Inhomogeneous electron gas. *Phys. Rev.*, 136:B864–B871, 1964.

[103] W. Kohn and L.J. Sham. Self-consistent equations including exchange and correlation effects. *Phys. Rev*, 140:A1133–A1138, 1965.

[104] J. J. Rehr and R. C. Albers. Theoretical approaches to x-ray absorption fine structure. *Rev. Mod. Phys.*, 72:621–654, 2000.

[105] G. Kresse and J. Hafner. *Ab initio* molecular-dynamics simulation of the liquid-metal-amorphous-semiconductor transition in germanium. *Phys. Rev. B*, 49:14251–14269, 1994.

[106] R. Car and M. Parrinello. Unified approach for molecular dynamics and density-functional theory. *Phys. Rev. Lett.*, 55:2471–2474, Nov 1985.

[107] J. C. Slater. A simplification of the hartree-fock method. *Phys. Rev.*, 81:385–390, Feb 1951.

[108] L. H Thomas. The calculation of atomic fields. *Proc. Camb. Phil. Soc.*, 23(542), 1927.

[109] E. Fermi. *Z. Phys*, 48(73), 1928.

[110] D. M. Ceperley and B. J. Alder. Ground state of the electron gas by a stochastic method. *Phys. Rev. Lett.*, 45:566–569, Aug 1980.

[111] J. P. Perdew. Density functional theory and the band gap problem. *Int. J. Quantum Chem*, 28:497–523, 1985.

[112] A. Garc'ia, C. Elsässer, J. Zhu, S. G. Louie, and M. L. Cohen. Use of gradient-corrected functionals in total-energy calculations for solids. *Phys. Rev. B*, 46:9829–9832, 1992.

[113] B. G. Johnson, P. M. W. Gill, and J. A. Pople. The performance of a family of density functional methods. *J. Chem. Phys.*, 98(7):5612–5626, 1993.

[114] John P. Perdew, Kieron Burke, and Matthias Ernzerhof. Generalized gradient approximation made simple. *Phys. Rev. Lett.*, 77:3865–3868, 1996.

[115] J. P. Perdew, K. Burke, and M. Ernzerhof. Generalized gradient approximation made simple. *Phys. Rev. Lett.*, 78:1396–1396, 1997.

[116] G. Kresse and J. Hafner. *Ab initio* molecular dynamics for liquid metals. *Phys. Rev. B*, 47:558–561, 1993.

[117] G. Kresse and J. Furthmüller. Efficiency of *Ab initio* total energy calculations for metals and semiconductors using a plane-wave basis set. *Comput. Mater. Sci.*, 6:15 – 50, 1996.

[118] G. Kresse and J. Furthmüller. Efficient iterative schemes for *ab initio* total-energy calculations using a plane-wave basis set. *Phys. Rev. B*, 54:11169–11186, 1996.

[119] J. Heyd, G. E. Scuseria, and M. Ernzerhof. Hybrid functionals based on a screened coulomb potential. *J. Chem. Phys.*, 118(18):8207–8215, 2003.

[120] J. Heyd, G. E. Scuseria, and R. L. Martin. Hybrid functionals based on a screened coulomb potential. *J. Chem. Phys.*, 123:174101, 2006.

[121] J. Paier, M. Marsman, K. Hummer, G. Kresse, I. C. Gerber, and J. G. Ngyn. Screened hybrid density functionals applied to solids. *J. Chem. Phys.*, 124(15), 2006.

[122] P.E. Blöchl. Projector augmented-wave method. *Phys. Rev. B*, 50:17953–17979, Dec 1994.

[123] M. Gajdoš, K. Hummer, G. Kresse, J. Furthmüller, and F. Bechstedt. Linear optical properties in the projector-augmented wave methodology. *Phys. Rev. B*, 73:045112, Jan 2006.

[124] J. Grotendorst, editor. *Modern Methods and Algorithms of Quantum Chemistry*. John von Neumann Institute for Computing, Jüllich, NIC Series, 2000.

[125] R. Hoppe. The coordination number - an “inorganic chameleon". *Angew. Chem. Int. Ed. Engl.*, 9:25–34, 1970.

[126] R. Hoppe, S. Voigt, H. Glaum, J. Kissel, H.P. Muller, and K. Bernet. A new route to charge distribution in ionic solids. *J. less-Common Met.*, 156:105–122, 1989.

[127] Raymond Atta-Fynn, Parthapratim Biswas, Pablo Ordejón, and D. A. Drabold. Systematic study of electron localization in an amorphous semiconductor. *Phys. Rev. B*, 69:085207, Feb 2004.

[128] E. Fortunato, D. Ginley, H. Hosono, and D. C. Paine. Transparent conducting oxides for photovoltaics. *MRS Bull.*, 32:242–247, 2007.

[129] D.B. Buchholz, D.E. Proffit, M.D. Wisser, T.O. Mason, and R.P.H. Chang. Electrical and band-gap properties of amorphous zinc-indium-tin oxide thin films. *Prog. Nat. Sci.: Mater Int.*, 22(1):1 – 6, 2012.

[130] D.Y. Lee, J.R. Lee, G.H. Lee, and P.K. Song. Study on In-Zn-Sn-O and In-Sn-Zn-O films deposited on {PET} substrate by magnetron co-sputtering system. *Surf. Coat. Technol.*, 202(22-23):5718 – 5723, 2008.

[131] Steven P. Harvey, Thomas O. Mason, D. Bruce Buchholz, Robert P. H. Chang, Christoph Körber, and Andreas Klein. Carrier generation and inherent off-stoichiometry in Zn, Sn codoped indium oxide (ZITO) bulk and thin-film specimens. *J. Am. Ceram. Soc.*, 91(2):467–472, 2008.

[132] D. B. Buchholz, J. L., T. J. Marks, M. Zhang, and R. P. H. Chang. Control and characterization of the structural, electrical, and optical properties of amorphous zinc-indium-tin oxide thin films. *ACS Appl. Mater. Interfaces*, 1(10):2147–2153, 2009.

[133] A.K. Kulkarni, Kirk H. Schulz, T.S. Lim, and M. Khan. Dependence of the sheet resistance of indium-tin-oxide thin films on grain size and grain orientation determined from x-ray diffraction techniques. *Thin Solid Films*, 345(2):273 – 277, 1999.

[134] R. B. H. Tahar, T. Ban, Y. Ohya, and Y. Takahashi. Tin doped indium oxide thin films: Electrical properties. *J. Appl. Phys.*, 83(5):2631–2645, 1998.

[135] E. A. Stern, D. E. Sayers, and F. W. Lytle. Extended x-ray-absorption fine-structure technique. iii. determination of physical parameters. *Phys. Rev. B*, 11:4836–4846, Jun 1975.

[136] Supplemental material for for chem. mater. doi: 10.1021/cm502689x. `http://pubs.acs.org/doi/suppl/10.1021/cm502689x`. accessed: April 2016.

[137] S. Davis and G. Gutierrez. Structural, elastic, vibrational and electronic properties of amorphous Al_2O_3 from ab-initio calculations. *J. Phys. Cond. Matter*, 23:495401, 2011.

[138] K. Nishio, T. Miyazaki, and H. Nakamura. Universal medium-range order of amorphous metal oxides. *Phys. Rev. Lett.*, 111:155502, 2013.

[139] H.-X. Deng, S.-H. Wei, S.-S. Li, J. Li, and A. Walsh. Electronic origin of the conductivity imbalance between covalent and ionic amorphous semiconductors. *Phys. Rev. B*, 87:125203, 2013.

[140] B. Ravel and M. Newville. *ATHENA*, *ARTEMIS*, *HEPHAESTUS*: data analysis for X-ray absorption spectroscopy using *IFEFFIT*. *Journal of Synchrotron Radiation*, 12(4):537–541, Jul 2005.

[141] I. Štich, R. Car, and M. Parrinello. Amorphous silicon studied by ab initio molecular dynamics: Preparation, structure, and properties. *Phys. Rev. B*, 44:11092–11104, Nov 1991.

[142] N. A. Marks. Evidence for subpicosecond thermal spikes in the formation of tetrahedral amorphous carbon. *Phys. Rev. B*, 56:2441–2446, Aug 1997.

[143] Tomoko Yoshida, Tetsuo Tanabe, and Hisao Yoshida. XAFS study on silica glasses irradiated by high-energy particles. *Physica Scripta*, 2005(T115):435, 2005.

[144] D. Bruce Buchholz, Li Zeng, Michael J. Bedzyk, and Robert P.H. Chang. Differences between amorphous indium oxide thin films. *Prog. Nat. Sci.: Mater. Int.*, 23(5):475 – 480, 2013.

[145] F. Utsuno, H. Inoue, Y. Shimane, T. Shibuya, K. Yano, K. Inoue, I. Hirosawa, M. Sato, and T. Honma. A structural study of amorphous In_2O_3 films by grazing incidence X-ray scattering (GIXS) with synchrotron radiation. *Thin Solid Films*, 496:95–98, 2006.

[146] D.S. Yang, J.C. Lee, J.G. Chung, E. Lee, B. Anass, N-E. Sung, J.M. Lee, and J.H. Kang. Local structure and local conduction paths in amorphous (In,Ga,Hf)-ZnO semiconductor thin films. *Solid States Comm.*, 152:1867–1869, 2012.

[147] D. B. Buchholz, Q. Ma, D. Alducin, A. Ponce, M. Yacaman, R. Khanal, J. E. Medvedeva, and R.P.H. Chang. The structure and properties of amorphous indium oxide. *Chem. Mater.*, 26(18):5401–5411, 2014.

[148] G. Kresse and D. Joubert. From ultrasoft pseudopotentials to the projector augmented-wave method. *Phys. Rev. B*, 59:1758–1775, Jan 1999.

[149] J.W. Hennek, J. Smith, A. Yan, M.-G Kim, W. Zhao, V.P. Dravid, A. Facchetti, and T.J. Marks. Oxygen “getter" effects on microstructure and carrier transport in low temperature combustion-processed a-InXZnO (X= Ga, Sc, Y, La) transistors. *J. Am. Chem. Soc.*, 135:10729–10741, 2013.

[150] R. Khanal, D. B. Buchholz, R. P. H. Chang, and J. E. Medvedeva. Composition-dependent structural and transport properties of amorphous transparent conducting oxides. *Phys. Rev. B*, 91:205203, May 2015.

[151] J. E. Medvedeva and C.L. Hettiarachchi. Tuning the properties of complex transparent conducting oxides: Role of crystal symmetry, chemical composition, and carrier generation. *Phys. Rev. B*, 81:125116, 2010.

[152] A. Murat and J. E. Medvedeva. Electronic properties of layered multicomponent wide−band−gap oxides: a combinatorial approach. *Phys. Rev. B*, 85:155101, 2012.

[153] Sunho Jeong and Jooho Moon. Low-temperature, solution-processed metal oxide thin film transistors. *J. Mater. Chem.*, 22:1243–1250, 2012.

[154] E.A. Davis N.F. Mott. *Electron. Processes Non-Cryst. Mater.* Clarendon Press, Oxford, 1979.

[155] S. R. Forrest. The path to ubiquitous and low-cost organic electronic appliances on plastic. *Nat.*, 428(0028-0836):435, 2004.

[156] IGZO oxide semiconductor mass produced by sharp and semiconductor energy laboratory co. ltd. for display technologies. `http://sharp-world.com/igzo/`. accessed: October 2014.

[157] Jonathan W. Hennek, Myung-Gil Kim, Mercouri G. Kanatzidis, Antonio Facchetti, and Tobin J. Marks. Exploratory combustion synthesis: Amorphous indium yttrium oxide for thin-film transistors. *J. Am. Chem. Soc.*, 134(23):9593–9596, 2012. PMID: 22625409.

[158] A. Wang, J. R. Babcock, N. L. Edleman, A. W. Metz, M. A. Lane, R. Asahi, V. P. Dravid, C. R. Kannewurf, A. J. Freeman, and T. J. Marks. Indium-cadmium-oxide films having exceptional electrical conductivity and optical transparency: Clues for optimizing transparent conductors. *Proceedings of the National Academy of Sciences*, 98(13):7113–7116, 2001.

[159] H. Kim, C. M. Gilmore, A. Piqu, J. S. Horwitz, H. Mattoussi, H. Murata, Z. H. Kafafi, and D. B. Chrisey. Electrical, optical, and structural properties of indium-tin-oxide thin films for organic light-emitting devices. *J. Appl. Phys.*, 86(11):6451–6461, 1999.

[160] A. U. Adler, T. C. Yeh, D. B. Buchholz, R. P. H. Chang, and T. O. Mason. Quasi-reversible point defect relaxation in amorphous In-Ga-Zn-O thin films by in situ electrical measurements. *Appl. Phys. Lett.*, 102(12), 2013.

[161] J. Ni, H. Yan, A. Wang, Y. Yang, C. L. Stern, A. W. Metz, S. Jin, L. Wang, T. J. Marks, J. R. Ireland, , and C. R. Kannewurf. MOCVD-derived highly transparent, conductive zinc- and tin-doped indium oxide thin films: Precursor synthesis, metastable phase film growth and characterization, and application as anodes in polymer light-emitting diodes. *J. Am. Chem. Soc.*, 127(15):5613–5624, 2005.

[162] J. Heo, S. Bok Kim, and R. G. Gordon. Atomic layer deposited zinc tin oxide channel for amorphous oxide thin film transistors. *Appl. Phys. Lett.*, 101(11), 2012.

[163] S. R. Thomas, P. Pattanasattayavong, and T. D. Anthopoulos. Solution-processable metal oxide semiconductors for thin-film transistor applications. *Chem. Soc. Rev.*, 42:6910–6923, 2013.

[164] K. K. Banger, Y. Yamashita, K. Mori, R. L. Peterson, T. Leedham, J. Rickard, and H. Sirringhaus. Low-temperature, high-performance solution-processed metal oxide thin-film transistors formed by a solgel on chip process. *Nat Mater*, 10:45–50, 2011.

[165] Myung-Gil Kim, Mercouri G. Kanatzidis, Antonio Facchetti, and Tobin J. Marks. Low-temperature fabrication of high-performance metal oxide thin-film electronics via combustion processing. *Nat Mater*, 10:382–388, 2011.

[166] Young Hwan Hwang, Jin-Suk Seo, Je Moon Yun, HyungJin Park, Shinhyuk Yang, Sang-Hee Ko Park, and Byeong-Soo Bae. An ‘aqueous route’ for the fabrication of low-temperature-processable oxide flexible transparent thin-film transistors on plastic substrates. *NPG Asia Mater*, 5:45, 2013.

[167] Stephen T. Meyers, Jeremy T. Anderson, Celia M. Hung, John Thompson, John F. Wager, and Douglas A. Keszler. Aqueous inorganic inks for low-temperature fabrication of ZnO TFTs. *J. Am. Chem. Soc.*, 130(51):17603–17609, 2008.

[168] Chang-Ho Choi, Seung-Yeol Han, Yu-Wei Su, Zhen Fang, Liang-Yu Lin, Chun-Cheng Cheng, and Chih-hung Chang. Fabrication of high-performance, low-temperature solution processed amorphous indium oxide thin-film transistors using a volatile nitrate precursor. *J. Mater. Chem. C*, 3:854–860, 2015.

[169] Sunho Jeong, Ji-Yoon Lee, Sun Sook Lee, Youngmin Choi, and Beyong-Hwan Ryu. Impact of metal salt precursor on low-temperature annealed solution-derived ga-doped in2o3 semiconductor for thin-film transistors. *J. Phys. Chem. C*, 115(23):11773–11780, 2011.

[170] R. D. Shannon. Revised effective ionic radii and systematic studies of interatomic distances in halides and chalcogenides. *Acta Crystallogr., Sect. A*, 32(5):751–767, Sep 1976.

[171] K. Wolfgang, Daniel F. Urban, and Christian Elsösser. Origin of subgap states in amorphous In-Ga-Zn-O. *J. Appl. Phys.*, 114(16), 2013.

[172] J. Robertson and Y. Guo. Light induced instability mechanism in amorphous ingazn oxide semiconductors. *Appl. Phys. Lett.*, 104(16), 2014.

[173] J. F. Conley. Instabilities in amorphous oxide semiconductor thin-film transistors. *IEEE Transactions on Device and Materials Reliability*, 10(4):460–475, Dec 2010.

[174] S. Lee, K. Ghaffarzadeh, A. Nathan, J. Robertson, S. Jeon, C. Kim, I. Song, and U-In Chung. Trap-limited and percolation conduction mechanisms in amorphous oxide semiconductor thin film transistors. *Appl. Phys. Lett.*, 98(20), 2011.

[175] K. Nomura, T. Kamiya, H. Ohta, K. Ueda, M. Hirano, and H. Hosono. Carrier transport in transparent oxide semiconductor with intrinsic structural randomness probed using single-crystalline $InGaO_3(ZnO)_5$ films. *Appl. Phys. Lett.*, 85(11):1993–1995, 2004.

[176] T. Kamiya, K. Nomura, and H. Hosono. Origin of definite hall voltage and positive slope in mobility-donor density relation in disordered oxide semiconductors. *Appl. Phys. Lett.*, 96(12), 2010.

[177] David Adler, Laurence P. Flora, and Stephen D. Senturia. Electrical conductivity in disordered systems. *Solid State Commun.*, 12(1):9 – 12, 1973.

[178] W. Chr. Germs, W. H. Adriaans, A. K. Tripathi, W. S. C. Roelofs, B. Cobb, R. A. J. Janssen, G. H. Gelinck, and M. Kemerink. Charge transport in amorphous InGaZnO thin-film transistors. *Phys. Rev. B*, 86:155319, Oct 2012.

[179] Supplemental material for for adv. electron. mater., doi: 10.1002/aelm.201500146. `http://onlinelibrary.wiley.com/wol1/doi/10.1002/aelm.201500146/suppinfo`. accessed: April 2016.

[180] Jae Gwang Um, Mallory Mativenga, and Jin Jang. Mechanism of positive bias stress-assisted recovery in amorphous-indium-gallium-zinc-oxide thin-film transistors from negative bias under illumination stress. *Appl. Phys. Lett.*, 103(3), 2013.

[181] K. Ghaffarzadeh and R. Das. Metal oxide tft backplanes for displays 2014-2024: Technologies, forecasts, players. Technical report, IDTechEx, August 2014.

[182] Paweł P. Zawadzki, John Perkins, and Stephan Lany. Modeling amorphous thin films: Kinetically limited minimization. *Phys. Rev. B*, 90:094203, Sep 2014.

[183] J. E. Medvedeva. Unconventional approaches to combine optical transparency with electrical conductivity. *Appl. Phys. A*, 89:43–47, 2007.

[184] T. Kamiya, K. Nomura, M. Hirano, and H. Hosono. Electronic structure of oxygen deficient amorphous oxide semiconductor a-$InGaZnO_{4-x}$: Optical analyses and first-principle calculations. *Physica Status Solidi C*, 5:3098–3100, 2008.

[185] K. Wolfgang and E. Christian. Density-functional theory study of stability and subgap states of crystalline and amorphous Zn-Sn-O. *Thin Solid Films*, 555(0):81 – 86, 2014. International Symposia on Transparent Conductive Materials, October 2012.

[186] W. H. Han, Young Jun Oh, K. J. Chang, and Ji-Sang Park. Electronic structure of oxygen interstitial defects in amorphous In-Ga-Zn-O semiconductors and implications for device behavior. *Phys. Rev. Appl.*, 3:044008, 2015.

[187] Inorganic crystal structure database (icsd).

[188] A. Murat, A. U. Adler, T. O. Mason, and J. E. Medvedeva. Carrier generation in multicomponent wide-bandgap oxides: $InGaZnO_4$. *J. Am. Chem. Soc.*, 135(15):5685–5692, 2013.

VITA

Rabi Khanal was born in Gulmi, Nepal. He received his Bachelor of Science in Physics from Tribhuvan University, Butwal Multiple Campus, Butwal, Nepal in May 2008. He received his Master of Science in Physics from Tribhuvan University, Central Department of Physics (CDP), Kritipur, Kathmandu, Nepal in August 2011. For his Master's Degree, he wrote a thesis, entitled, *Electronic and magnetic properties of ordered (Pt_3Mn and Pd_3Mn) & disordered ($Pt_{(1-x)}Mn_x$ ($x = 0.01$, 0.05, and 0.10) and $Pd_{(1-x)}Mn_x$ ($x = 0.20$, 0.25 and 0.50)) binary alloy*, at S.N. Bose National Center for Basic Sciences (SNBNCBS), Kolkata, India under the supervision of Dr. Abhijit Mookerjee (SNBNCBS) and Dr. Narayan P. Adhikari (CDP). After finishing his Masters, he moved to The Abdus Salam International Center for Theoretical Physics (ICTP), Trieste, Italy, where he got a Post Graduate Diploma in Condensed Matter Physics in 2012. At the ICTP, he wrote his Post Graduate Diploma thesis, *The dissociation constant of water at extreme conditions: a molecular dynamics study*, under the supervision of Dr. Sandro Scandolo. In 2012, he joined the group of Dr. Julia E. Medvedeva at Missouri University of Science and Technology, Rolla, MO, 65409 to work on his Ph.D. in Condensed Matter Physics, and received his degree in December 2016.

He has published five refereed journal papers. Based on his research he was awarded travel grants from the American Physical Society (APS) and the Materials Computation Center (MCC) at the University of Illinois Urbana-Champaign. Also, he received several prizes and grants from the Missouri University of Science and Technology and from the Physics Department. For the last year of his Ph.D., he received a dissertation completion fellowship from the Office of the Graduate Studies. He has been a member of the American Physical Society since 2012.